The interplay of long-range magnetic order and single-ion anisotropy in rare earth nickel germanides

by

Zahirul Islam

A dissertation submitted to the graduate faculty
in partial fulfillment of the requirements for the degree of
DOCTOR OF PHILOSOPHY

Major: Condensed Matter Physics
Major Professors: Alan I. Goldman and Paul C. Canfield

Iowa State University
Ames, Iowa
1999

Graduate College
Iowa State University

This is to certify that the Doctoral dissertation of

Zahirul Islam

has met the dissertation requirements of Iowa State University

---

Committee Member

Committee Member

Committee Member

Committee Member

Co-major Professor

Co-major Professor

For the Major Program

For the Graduate College

TABLE OF CONTENTS

LIST OF TABLES

LIST OF FIGURES

1 INTRODUCTION

The purpose of this dissertation is to investigate the interplay between long-range magnetic order and single-ion anisotropy across an isostructural series of rare earth (R) intermetallic compounds ($R\mathrm{Ni_2Ge_2}$) as a function of the R elements. Both conventional magnetic neutron diffraction and the newly developed x-ray resonant exchange scattering (XRES) techniques are used. The experimental work is augmented by computational investigations of the mechanism driving the phase transitions in these systems. In addition, experimental and computational studies of the low-temperature metamagnetic properties of a particularly interesting member of the family, $\mathrm{TbNi_2Ge_2}$, are also discussed.

Basic Magnetic Interactions

Crystals with tetragonal symmetry such as the ternary rare earth intermetallic compounds with composition RT_2X_2, where T represents a transition metal ion, and X denotes Si or Ge, display a wide variety of magnetic and correlated electron phenomena [1, 2, 3]. With the general exception of the T=Mn compounds, which exhibit ferromagnetism, most of these materials, with moment-bearing R ions, show antiferromagnetic ordering at low temperature with virtually all of the magnetism associated with the $4f$ electrons. Many of these compounds also exhibit field induced magnetic phase transitions, or metamagnetism, at sufficiently low temperatures. There are various parameters in the Hamiltonian of these complex systems that determine their magnetic phase tran-

sitions and ordered structures. However, a quantitative understanding of their magnetic ordering can be achieved within a simple theoretical framework involving a few basic magnetic interactions which are briefly reviewed below.

The R ions in these compounds are well separated from each other so that any direct exchange between two neighboring $4f$ shells is negligible. Due to their metallic nature, however, the magnetic interaction between two such ions can take place via the polarization of the conduction band electrons as in the case of the elemental rare earth metals. This is the RKKY (Ruderman-Kittel-Kasuya-Yosida) indirect exchange interaction which is responsible for cooperative phenomena such as magnetic ordering. The simplest effective Hamiltonian for this two-ion interaction is [4]:

$$\mathcal{H}_{\text{RKKY}} = -\sum_{\substack{m,n \\ m>n}} \mathcal{J}(\mathbf{R}_{mn})\mathbf{J}_m \cdot \mathbf{J}_n, \tag{1.1}$$

where $\mathbf{J}$ is the total angular momentum operator and $\mathcal{J}$ is the exchange interaction between two R ions. By considering the response of a set of R ions, interacting via the RKKY exchange, to a periodic field in the paramagnetic phase it is found that the antiferromagnetic ordering temperature

$$T_N \propto (g_J - 1)^2 J(J+1), \tag{1.2}$$

which is the well-known de Gennes scaling for T_N [5]. Such scaling behavior is expected for isostructural compounds where the ordering temperature is determined solely by the RKKY exchange interaction.

The RKKY interaction is determined by the electronic band structure and Fermi surface topology. In the case of elemental rare earths it is well established that nesting of the Fermi surface, which enhances the indirect exchange interaction, is responsible for the magnetic ordering. Intermetallic compounds such as RT_2X_2 are structurally much more complex. While the experimental studies of their magnetism have focused on determination of the ordered states, a quantitative theoretical understanding of their

magnetic phase transition is less developed than for the case of the pure rare earths. Although a few computational investigations, such as those done for $R\mathrm{Ni_2B_2C}$ series, suggest [6] the connection of Fermi surface nesting to their magnetic ordering a clear demonstration of such a correlation by means of manifestly changing the band filling in such complex systems is lacking. A primary concern of the present work is the investigation of such correlations to better understand the origin of magnetic ordering in $R\mathrm{Ni_2Ge_2}$ compounds within the theoretical framework being outlined. Although this dissertation is focused on a particular family of materials, results of such studies may, however, be applicable to other RT_2X_2 compounds in light of the isostructural relationship and the generality of the interactions being considered.

While the RKKY interaction is responsible for the long-range order, the anisotropy, which in extreme cases, is either uniaxial or planar in tetragonal systems, is often determined by crystalline electric field (CEF) effects. In the presence of CEF the degeneracy of the Hund's rule ground state J-multiplet is removed according to the point symmetry of the rare earth site. In addition, CEF also affects the ordering temperature [7] and plays an important role in the low temperature metamagnetic phases. In tetragonal systems five parameters are required to determine the CEF which is much smaller number of parameters than is required for systems with lower symmetry (*e.g.* nine in orthorhombic systems). The Hamiltonian for this single-ion interaction is given by

$$\mathcal{H}_{\mathrm{CEF}} = \sum_n \left(\sum_{l=2,4,6} B_l^0 O_l^0(\mathbf{J}_n) + \sum_{l=4,6} B_l^4 O_l^4(\mathbf{J}_n) \right), \tag{1.3}$$

where the B_l^m's are the CEF parameters characteristic of a material and the O_l^m's are Stevens operators [8, 9]. This simple form is only valid when the axis of quantization is chosen to be along the four-fold direction. It should be noted that the CEF parameters, B_l^m's, are expected to change little as a function of temperature assuming that the thermal variation of the lattice constants is not too great. The temperature dependence of the anisotropy in the paramagnetic phase then originates from thermal population,

as determined by the trivial Boltzmann factor, of the higher levels of the CEF split J-multiplet. In the ordered state, the variation of the anisotropy with temperature depends on the nature of the ordering which can be rather complicated. This is because the Stevens operators being polynomials in $\mathbf{J}$ have strong temperature dependence. The expectation values of these operators vary as [5]

$$\langle O_l^m(\mathbf{J})\rangle_T = \langle O_l^m(\mathbf{J})\rangle_{T=0} \left(\frac{|\langle \mathbf{J}\rangle|}{J}\right)^{\frac{l(l+1)}{2}}, \tag{1.4}$$

which was first shown by Zener [10] using a classical theory and later derived rigorously by Callen and Callen [11, 12]. A more recent theoretical study of the temperature dependence of magnetization and anisotropy that takes into account the effects of nonspherical precession of $\mathbf{J}$ in the presence of CEF is given by Lindgård and co-workers [13]. This work showed when such precessions are negligible the well-known power law for the temperature dependence for the Stevens' operators as shown above is valid. Accordingly, as the ordered moments grow on decreasing temperature below T_N the CEF terms change more rapidly than the exchange term which varies as $\left(\frac{|\langle \mathbf{J}\rangle|}{J}\right)^2$, showing the increasing importance of the CEF interaction in the ordered states. In order to study anisotropic effects of $\mathcal{H}_{\text{CEF}}$ on magnetic structures a series-wide investigation on single crystals can be performed. In particular, since Gd has zero orbital momentum due to its half-filled $4f$ shell, $\mathcal{H}_{\text{CEF}}$ is ineffective in this case. Thus, a comparison between the structures of the Gd member to those of the other members of the series may allow for a separation of CEF effects.

Finally, the Zeeman interaction due to the internal field, when $\mathbf{J}$ is a constant of motion, can be written as [14, 15]

$$\mathcal{H}_{\text{Zee}} = g_J \mu_B \sum_n \mathbf{J}_n \cdot \mathbf{H}(\mathbf{R}_n), \tag{1.5}$$

where $\mathbf{H}(\mathbf{R})$ is a spatially varying field. For the case of $4f$ compounds, $\mathbf{J}$ is constant to a good approximation (with possible exceptions in the Sm and Eu compounds) since

term-splitting into multiplets due to spin-orbit coupling is $\sim 10^4$ K [16] whereas the multiplet-splitting due to CEF is $\sim 10^2 - 10^3$ K. So, only the Hund's rule ground state multiplet, with constant angular momentum, needs to be considered for the temperature of interest ($< 10^3$ K). In comparison, the RKKY interaction which is primarily responsible for determining the ordering temperature is of the order of $\sim 10 - 10^2$ K [17]. The Zeeman interaction is essential for the study of the effects of an external field on periodic structures and metamagnetism. In sufficiently high fields the ordered structure transforms into a saturated paramagnet with all the moments reaching the saturation value of $g_J \mu_B J$. The structures in intermediate fields, however, can be very complex due to an interplay of all three interactions above: $\mathcal{H}_{\rm RKKY}$ $\mathcal{H}_{\rm CEF}$ and $\mathcal{H}_{\rm Zee}$, respectively. When all three terms are comparable, a multi-step metamagnetic behavior with subtle differences among the metamagnetic phases can occur. This case is explored in some detail in chapter 6 using a "toy model" with an R ion having $J = 2$.

Although a remarkably large number of magnetic phenomena can be adequately explained with the above set of basic interactions it should be noted that magneto-elastic coupling can also be important and may be manifest in both CEF and exchange terms. This type of interaction, if strong enough, lowers the crystallographic symmetry via a structural distortion such as the tetragonal-to-orthorhombic transition at T_N observed in Tb and Er nickel borocarbides [18, 19]. The Hamiltonian for this type of interaction is rather complex and reference should be made to Morin and Schmitt [20] and Callen and Callen [12]. In addition, anisotropic two-ion exchange interaction due to a number of effects as elucidated by Jensen and co-workers [21] may also be significant.

Prelude to $R\mathrm{Ni_2Ge_2}$

Among the vast class of RT_2X_2 compounds, the $R\mathrm{Ni_2Ge_2}$ family of materials is of particular interest. These materials crystallize in the body-centered tetragonal $\mathrm{ThCr_2Si_2}$

structure with space group I4/mmm (D_{4h}^{17}). The conventional tetragonal unit cell of this structure is shown in Fig. 1.1. There are two formula units in this unit cell. The Wyckoff positions of the R atoms are 2(a) with tetragonal point symmetry D_{4h} which plays the crucial role of determining the CEF anisotropy. The Ni atoms are located at 4(d). There are two Ge atoms positioned one above and one below each R atom, at Wyckoff sites 4(e). In the unit cell the R atoms are located at the corners and body center while the Ni atoms are positioned on the cell faces. This layered structure can be visualized as R planes separated along the $\hat{\mathbf{c}}$ axis by a network of Ni-Ge tetrahedra. These atoms form a bicapped-square-prismatic coordination-polyhedron surrounding each R atom located at the polyhedron center as depicted in Fig. 1.1.

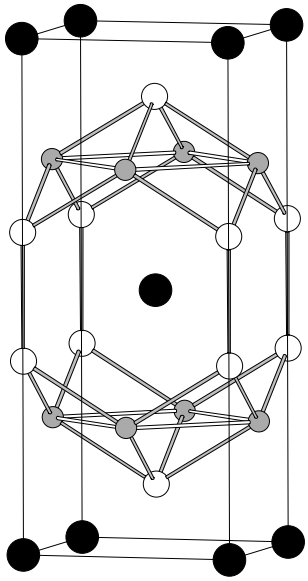

Figure 1.1 A conventional unit cell of the RNi$_2$Ge$_2$ structure. The solid black circles represent the R elements, small shaded circles stand for Ni atoms and the big open circles denote Ge atoms.

The unit cell volume (V_c) and the lattice parameters (a and c) of all the members, except those of PmNi$_2$Ge$_2$ and EuNi$_2$Ge$_2$, are shown in Fig. 1.2(a)-(c) (see also Table 1.1). The figures display a gradual decrease of V_c as well as of a and c due to the

"lanthanide contraction." This smooth structural variation is important since it implies that in the paramagnetic state the electronic bands across the series with trivalent R ions should be similar when the $4f$ electrons are treated as part of the core. Thus, since band electrons determine the RKKY interaction, some general feature regarding the long-range order across the series may exist. On the other hand, $EuNi_2Ge_2$ has larger ($\sim 3\%$ compared to those of $GdNi_2Ge_2$, see Table 1.1) lattice parameters, due to the larger ionic radius of divalent Eu. For this reason it provides the opportunity to study the effects of band filling on the RKKY interaction and magnetic ordering.

In order to illustrate the type of magnetic phenomena that can occur in RNi_2Ge_2 two particular cases from the isostructural RNi_2Si_2 series can be considered. These materials display considerable magneto-crystalline anisotropy which manifests remarkably in $TbNi_2Si_2$ [25, 26]. In zero field, $TbNi_2Si_2$ is an *incommensurate amplitude modulated* (AM) antiferromagnet below T_N=15 K. At about T_t=9 K, the structure locks into a *commensurate equal moment* (EM) phase (see Refs. [25, 26] and references therein). In both the phases, the Tb moments are aligned with the $\hat{\mathbf{c}}$ axis. The most striking behavior was found [25] at 1.3 K, where five metamagnetic transitions were seen in an external field applied along the $\hat{\mathbf{c}}$ axis, due to strong uniaxial anisotropy. Subsequently, neutron diffraction on single crystals of $TbNi_2Si_2$ in a field revealed a rich phase diagram [26] for this material. Among various phases, a field-induced transition into an AM structure from an EM phase was reported, suggesting a strong interplay of RKKY and CEF interactions. The neighboring $DyNi_2Si_2$ compound also undergoes two magnetic phase transitions in zero applied field, at T_t=3.4 K and T_N=6 K, respectively [27, 28, 29]. As in the case of $TbNi_2Si_2$, the magnetic structure below T_N but above T_t is *incommensurate* AM, while below T_t the structure becomes EM *commensurate*. In addition, the magnetization is anisotropic and a series of four metamagnetic transitions at 1.5 K, with the field applied along the $\hat{\mathbf{c}}$ axis, is also observed [27].

The salient features of the magnetic properties of the silicides, just presented, are that

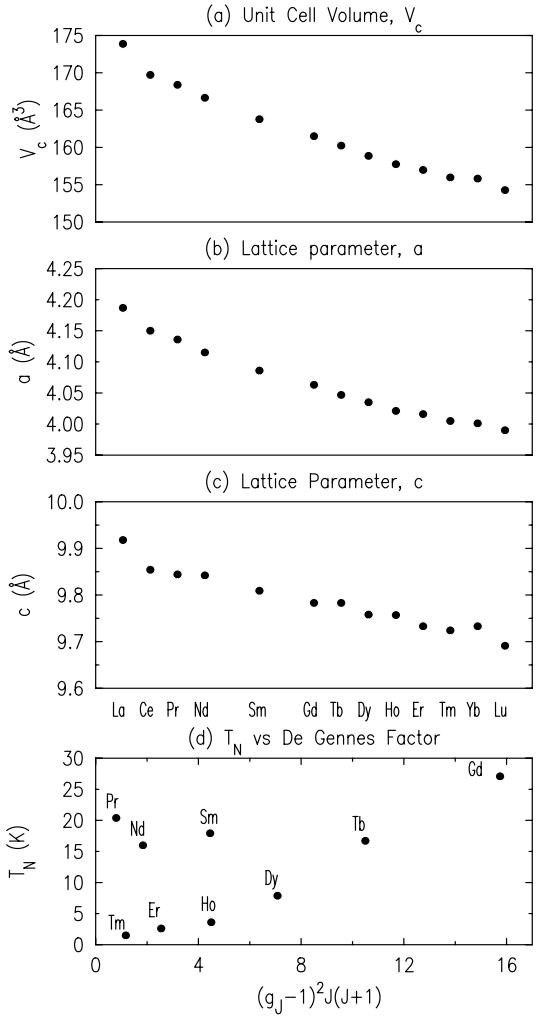

Figure 1.2 Unit cell volume and lattice parameters ((a)-(c)) of RNi_2Ge_2 compounds showing the "lanthanide contraction" [22]. (d) T_N as a function of de Gennes scaling factor [23]. T_N for the Tm compound, from Ref. [24].

there exists an additional transition below the ordering temperature which corresponds to an incommensurate-commensurate structural transformation with a saturation of the $4f$ moments, strong anisotropy and low-temperature metamagnetism. These observations are in fact quite general, found to occur in many rare earth intermetallic compounds [3, 30]. The origin of the incommensurate phase just below the ordering temperature lies in the RKKY interaction, which is long-range and oscillatory with periodicity related to the Fermi wave vector of the conduction electrons. As the temperature is lowered, a balance between the exchange and the magneto-crystalline anisotropy determines the evolution of the structure. In general, the AM phase can not be stable down to the absolute zero of temperature due to entropic effects [31]. An AM phase can be stable at finite temperature below T_N because a sinusoidal AM arrangement has higher entropy compared to that of an EM structure. Thus, the free energy, $F = U - TS$, is lower than that of the EM phase at finite temperature. As the temperature is lowered, the entropic term decreases and the stable structure corresponds to that which minimizes the internal energy term, U. This behavior is also expected from Nernst's theorem. As a consequence, the modulated structure squares up and in the case of uniaxial anisotropy transforms into an antiphase domain structure [31], as exemplified above. This squaring-up certainly happens in compounds with Kramers ions (*e.g.* Dy, Er), since in the absence of any exchange or external field, they possess at least a magnetic doublet as their ground state. When a nonvanishing exchange is present, such a doublet splits due to the Zeeman interaction. Therefore, at a finite temperature below T_N, the thermal population of the higher level, below T_N, may stabilize an AM structure. However, as the temperature is lowered, the moment saturates to some finite value associated with the ground state, due to thermal depopulation of the higher level. For non-Kramers ions (*e.g.* Pr, Tb), on the other hand, a nonmagnetic or singlet ground state is possible. In this case, if the exchange is weaker than some critical value necessary to polarize the nonmagnetic state by admixing higher CEF levels [32, 33], an AM phase can persist even at 0 K. Such a

situation seems to exist in $PrNi_2Si_2$ [34] down to 1.5 K, whereas T_N is ~20 K.

Due to the isostructural relationship such interplay of long-range order and anisotropy in the RNi_2Ge_2 compounds can also be expected. However, no single-crystal work prior to the series-wide investigations [23] initiated at the Ames Laboratory exists. Bulk measurements such as susceptibility and magnetization by previous researchers have been performed only on polycrystalline samples where information concerning anisotropy was not obtainable due to powder averaging. In addition, phase transitions associated with subtle spin reorientations without any changes in the sublattice magnetization often evade detection in bulk measurements on polycrystalline samples [35]. Further, powder samples prepared by pulverizing arc-melted ingots are prone to exhibit strain induced changes in thermodynamic and transport properties. Extrinsic effects due to impurity phases may also appear in such samples. Nevertheless, the magnetic structures of some of the RNi_2Ge_2 compounds have been investigated by neutron diffraction techniques on powder samples. A summary of earlier work on these materials is given below. Various inconsistencies in these experimental results show the need for a systematic studies on single-crystal samples of these compounds.

$NdNi_2Ge_2$ is the only light R member with an ordered state that has been studied using neutron diffraction by Szytuła and co-workers [36]. A longitudinal AM structure with moments along the $\hat{\mathbf{c}}$ axis described by (0 0 0.805) at 2.2 K was determined. This AM structure persists up to T_N=16 K. No other transition below T_N was observed, and the structure is AM at relatively low temperature, whereas Nd is a Kramers ion. These observations do not conform to the expectations stated above.

Both Eu and Gd highly absorb neutrons, making neutron diffraction studies of their compounds impractical, especially for the polycrystalline samples. This is perhaps why neutron scattering studies have not been performed on $EuNi_2Ge_2$ and $GdNi_2Ge_2$. However, susceptibility and Mössbauer spectroscopic measurements on polycrystalline samples were carried out by Felner and Nowik [37]. As in the case of $NdNi_2Ge_2$, only the

Néel transition was observed at 30 K and 22 K, respectively. From the hyperfine field measurements the easy axis of magnetization was found to be at 44° and 75° from the $\hat{\mathbf{c}}$ axis, respectively.

Neutron diffraction studies by two groups on polycrystalline $TbNi_2Ge_2$ indicated the structures to be quite complex. Pinto and co-workers [38] observed two transitions in this compound at $T_N = 16$ K and $T_t = 9$ K, respectively, and thought the structure just below T_N to be incommensurate. The phase below T_t was mentioned to be complex, and no further details were provided by this group. Later, Bourée-Vigneron [39] also observed two transitions, at T_N=17 K and T_t=10.25 K, respectively. However, this work found both the phases to be commensurate, with Tb moments aligned with the $\hat{\mathbf{c}}$ axis. According to this work, the structure below T_N but above T_t is AM with wave vector (0 0 $\frac{3}{4}$). Below T_t, a squaring-up of the moments and a new modulation ($\frac{1}{2}$ $\frac{1}{2}$ $\frac{1}{2}$) were observed indicating the complexity of this phase. The complete determination of the structure, however, remained incomplete. In fact, an ordered Tb moment value of 12.45±0.35 μ_B was ascribed to some sites, which is surprising since the saturation value of 9.0 μ_B is expected for the ionic moment.

Polycrystalline $DyNi_2Ge_2$ has been studied by various groups. A T_N of 11 K reported by earlier groups [3] is considerably different from that found by André and co-workers [40]. They determined T_N to be 7.5 K from susceptibility measurements. According to their powder neutron diffraction measurements, T_N is 8.5 K. At 1.4 K, the structure was found to be AM with propagation vector (0 0 0.788) and ordered Dy moments at 20° from the $\hat{\mathbf{c}}$ axis. No additional transition was observed.

The results for the magnetic structure of $HoNi_2Ge_2$ also exhibit inconsistencies. Pinto *et al.* reported [38] the structure to be incommensurate below T_N=6 K with a modulation vector of the form (0 0 q_z), where q_z=0.76, and moment directions in the tetragonal basal plane (a flat spiral). André and co-workers found [40] the modulation to be of the form (q_x q_y q_z) below a transition temperature of 4.8 K with moments at an angle of 42° from

the $\hat{\mathbf{c}}$ axis.

According to neutron diffraction studies, $ErNi_2Ge_2$ [40] and $TmNi_2Ge_2$ [24] order with a modulation of (0 0 0.757) and (0 0 0.785) below the T_N of 3.65 K and ~1.5 K, respectively. The magnetic structures of both compounds were suggested to be modulated with Er moment forming an angle of 64° with $\hat{\mathbf{c}}$ axis, while the Tm moment being locked to the basal plane.

Perhaps the only consistent finding of the earlier investigations is that the propagation vector at the onset of ordering is of the form (0 0 q_z), with the exception of $HoNi_2Ge_2$, for which a different modulation was also reported [40]. In general, however, the inconsistency of results obtained by different groups, the lack of observation of additional transitions and the incomplete knowledge of the ordered phases make clear the need for systematic studies of single crystals in order to obtain a correct understanding of anisotropy and long-range magnetic order in the RNi_2Ge_2 materials. Single crystals of all the members of this family, except $PmNi_2Ge_2$, have been grown at the Ames Laboratory. Measurements of macroscopic properties, such as magnetization and electrical resistivity, have been carried out on these single-crystal samples [23].

Among these compounds the members with Pr, Nd, Sm and Eu through Tm with antiferromagnetic (AF) ground states are the focus of the current investigations. Here, the salient magnetic properties obtained from measurements on single crystals are recapitulated. In Fig. 1.2(d) the Néel temperatures (see Table 1.1 also) of these compounds are plotted as a function of the de Gennes factor. The T_N's of the heavy rare earth compounds seem to increase with the scaling factor with small deviations from the expected linear behavior. These deviations are more dramatic in the case of the light rare earths which do not follow the scaling at all. This indicates the significant role [7], particularly in the light R systems, played by the CEF interactions in determining the transition temperatures, in addition to their role in fixing the single-ion anisotropy. This anisotropy, as determined from the susceptibility measurements with a field applied along the $\hat{\mathbf{c}}$ axis

Table 1.1 The transition temperatures [23] (T_N of Tm member, from Ref. [24]), anisotropy [23], lattice parameters [22], cell volume [22] and magnetic ordering vectors, (0 0 q_z), of the RNi$_2$Ge$_2$ compounds with long-range order.

R	T_N (K)	T_t (K)	Anisotropy (T>T$_N$)	a (Å) (300 K)	c (Å) (300 K)	V_c (Å^3) (300 K)	q_z $\left(\frac{2\pi}{c}\right)$	q_z (Å^{-1})
Pr	20.4	7.7	$\chi_{\parallel} > \chi_{\perp}$	4.136	9.844	168.4	0.809 [41]	0.5176
Nd	16.0	2.6	$\chi_{\parallel} > \chi_{\perp}$	4.115	9.842	166.7	0.805 [36]	0.5139
Sm	17.9	11.8	$\chi_{\parallel} < \chi_{\perp}$	4.086	9.809	163.8	0.791 [42]	0.5067
Eu	30.8	13.4	$\chi_{\parallel} \sim \chi_{\perp}$	4.140	10.10	173.1	1.00 [43]	0.6221
Gd	27.1	16.8	$\chi_{\parallel} \sim \chi_{\perp}$	4.063	9.783	161.5	0.793 [43]	0.5074
Tb	16.7	9.6	$\chi_{\parallel} > \chi_{\perp}$	4.047	9.783	160.2	0.758 [44]	0.4868
Dy	7.9	2.7	$\chi_{\parallel} > \chi_{\perp}$	4.035	9.758	158.9	0.75 [45]	0.4829
Ho	3.6	-	$\chi_{\parallel} \sim \chi_{\perp}$	4.021	9.757	157.8	0.76 [38]	0.4894
Er	2.6	-	$\chi_{\parallel} < \chi_{\perp}$	4.016	9.733	157.0	0.757 [40]	0.4889
Tm	1.5	-	$\chi_{\parallel} < \chi_{\perp}$	4.005	9.724	156.0	0.785 [24]	0.5072

($\chi_{\parallel}$) and perpendicular to it ($\chi_{\perp}$), is also shown in Table 1.1. These measurements reveal significant magneto-crystalline anisotropy in the paramagnetic phase for all but the Eu and Gd compounds (Table 1.1, see also Ref. [23]). Additional phase transitions below the ordering temperature are also observed in all of them except for the Ho, Er, and Tm members (Table 1.1), where T_N itself is low because of the small de Gennes factor. Thus, additional transitions, if they exist, are expected to be at much lower temperature than 1.8 K for the first two and 1.5 K for the latter. In the case of Sm and Gd compounds, there is a third transition at 5.5 K and 18.5 K, respectively [23].

The Tb member of this series is of particular interest. $TbNi_2Ge_2$ was found to be strongly anisotropic with the easy axis of magnetization along $\hat{\mathbf{c}}$. Two well-defined magnetic phase transitions were observed in the anisotropic susceptibility measurements. The most interesting behavior, however, was found in the magnetization as a function of field applied along the $\hat{\mathbf{c}}$ axis at 2 K. By ramping the field up and down nine well-defined phases have been observed [23]. The large number of well-defined transitions (see Fig. 3.1(b) and 6.1) makes this uniaxial system a very good candidate for the study of metamagnetism. Indeed, the $H-T$ phase diagram (see Fig. 6.2) is rather complex and exhibits a large number of critical points where two or more phases coexist [23]. A primary focus in this work is on the zero-field and "zero"-temperature (1.4 K) boundary of this complex phase diagram. A correct determination of these perimeter phases may not only provide a better understanding of the Hamiltonian that governs the magnetic phenomena in such complex materials, but also build a foundation and pave the way for the future investigations of critical phenomena in a clean, well-characterized model system like this.

An Overview

In the present work a definitive determination of the zero-field magnetic structures of $TbNi_2Ge_2$ is undertaken. These structures can be compared with those of other anisotropic members such as the neighboring $DyNi_2Ge_2$ which is also under investigation. As mentioned above, a comparison of the ordered states of these anisotropic members to those of $GdNi_2Ge_2$ allows for a separation of the effects due to $\mathcal{H}_{\rm CEF}$. Next, a major focus of this dissertation is the study of the effects of band filling on long-range order. This can be accomplished by comparing the magnetic ordering in $EuNi_2Ge_2$, where Eu is divalent, to those of the trivalent members. Both experimental and computational techniques are employed to better understand the RKKY-type interaction, $\mathcal{H}_{\rm RKKY}$, and magnetic ordering in this complex crystal structure. The results of such investigations may also shed light on magnetic order-disorder transitions in the RT_2X_2-type compounds in general. Finally, with the knowledge of the zero-field structures, the metamagnetic phase transitions in $TbNi_2Ge_2$ are studied in order to observe the interplay of all three interactions, $\mathcal{H}_{\rm RKKY}$, $\mathcal{H}_{\rm CEF}$ and $\mathcal{H}_{\rm Zee}$, respectively.

In the study of magnetic structures on a microscopic scale, both XRES and magnetic neutron diffraction experiments are useful. The major advantage of using XRES is the superior **Q**-resolution available, allowing one to observe subtle changes in periodicities, as is often the case at phase transitions. In addition, small samples as well as materials containing elements such as B, Sm, Eu and Gd with high neutron capture cross-sections can be conveniently studied with this technique. The rather small cross-sections of resonant and non-resonant scattering compared to that of the Thomson scattering render the former to be effectively extinction-free, which facilitates more accurate integrated intensity measurements on single crystals. Finally, the elemental selectivity of the XRES technique makes it possible to study individual sublattices in a model-independent way. On the less favorable side, XRES can currently be performed only on single-crystal

samples. In addition, at present, it is not possible to determine the absolute values of the ordered moments and it is difficult to extract the ferromagnetic components using this technique. In the last three cases neutron scattering is undoubtedly superior. Hence, both of these complementary techniques have been utilized in the study of $R\mathrm{Ni_2Ge_2}$ compounds.

Both $\mathrm{TbNi_2Ge_2}$ and $\mathrm{DyNi_2Ge_2}$ have AM structures below T_N with propagation vectors, $\mathbf{q}_1$, (0 0 0.758) and (0 0 ∼0.75), respectively. The phase below T_t in both compounds is an *equal moment* (EM) *commensurate* structure. This EM phase is described by a set of three modulation vectors, namely, $\mathbf{q}_1$=(0 0 $\frac{3}{4}$) along with its third harmonic $\mathbf{q}_1'$=(0 0 $\frac{1}{4}$), $\mathbf{q}_2$=($\frac{1}{2}$ $\frac{1}{2}$ 0) and $\mathbf{q}_3$=($\frac{1}{2}$ $\frac{1}{2}$ $\frac{1}{2}$). The $\mathbf{q}_2$ and $\mathbf{q}_3$ modulations are due to the antiferromagnetically ordered planes present in the structure which may be the result of 'exchange frustrations' built into the EM structure [44, 45]. In both phases the ordered moments in $\mathrm{TbNi_2Ge_2}$ are aligned with the $\hat{\mathbf{c}}$ axis. In $\mathrm{DyNi_2Ge_2}$, the moments are canted away from the $\hat{\mathbf{c}}$ axis due to in-plane ordered component. This canting angle at 1.5 K is estimated to be $\sim 17^\circ$. The rotation of the ordered moments away from the $\hat{\mathbf{c}}$ axis is consistent with the weaker anisotropy in $\mathrm{DyNi_2Ge_2}$ observed in the paramagnetic phase compared to that of $\mathrm{TbNi_2Ge_2}$ [23].

The ordered structures just below T_N vary from one R compound to the next, as exemplified above, due to the change of $4f$ moments and CEF anisotropy. However, all of them are characterized by a single incommensurate propagation vector, as listed in Table 1.1, of the same symmetry (Λ line), (0 0 q_z). This observation was hypothesized to be due to Fermi surface nesting [44]. In order to verify this conjecture, $\mathrm{GdNi_2Ge_2}$ and $\mathrm{EuNi_2Ge_2}$, having the same isotropic moment but different band filling, were studied experimentally and computationally. According to the hypothesis, the Gd compound should order with a propagation vector on the Λ line close to the ones observed in the other trivalent members, whereas ordering vector for the Eu compound could be quite different, due to lower electron count in the latter. Indeed, XRES measurements show

that the ordering vector in the Gd compound is $\mathbf{q}_{Gd}$=(0 0 0.793), whereas that in Eu material is commensurate, $\mathbf{q}_{Eu}$=(0 0 1). Band and generalized electronic susceptibility calculations found not only that $\mathbf{q}_{Gd}$ is due to nesting but also that because of lower band filling in the Eu compound. the nesting in the latter occurs at $\mathbf{q}_{Eu}$. The elucidation of the origin of the Néel transition in RNi$_2$Ge$_2$ compounds is the most important theoretical result of this work.

Next, magnetic structures of EuNi$_2$Ge$_2$ and GdNi$_2$Ge$_2$ have been studied by XRES. As already mentioned, since both Eu and Gd absorb neutrons highly, XRES is the probe of choice in these studies. In both materials the moments are locked to the basal plane below T_t. The transition at T_t in EuNi$_2$Ge$_2$ corresponds to spin reorientations in the tetragonal basal plane whereas an ordered component along the $\hat{\mathbf{c}}$ axis develops in GdNi$_2$Ge$_2$ [43].

Finally, as a part of the series-wide study, the metamagnetic structures at 1.4 K of TbNi$_2$Ge$_2$ have been investigated using neutron diffraction measurements. The first metamagnetic structure at 16.1 kG, consists of Tb ions with reduced moments at certain sites. Calculations for a simple "toy model" with an ion having $J = 2$ suggest that this may be due to *moment instability* originating from an interplay of CEF effects and Zeeman interactions with a local magnetic field. Also, the AF planes are present in all the metamagnetic structures, contrary to the naive expectation that *spin-flip* transitions induced by the external field will make such planes ferromagnetic. Neutron diffraction results for all these phases are also discussed.

The organization of the dissertation is as follows. The following chapter summarizes the crystal growth and experimental methods, with particular emphasis on the neutron and XRES techniques which are the primary tools used for the magnetic structure determinations. Chapter 3 is concerned with the zero-field magnetic structures of anisotropic systems, TbNi$_2$Ge$_2$ and DyNi$_2$Ge$_2$. In Chapter 4, a closer look is given to the RKKY interaction and the hypothesis of nesting as the driving mechanism for the Néel transition

in $R\mathrm{Ni_2Ge_2}$ compounds is developed. Chapter 5 presents the XRES investigations of magnetic structures of $\mathrm{GdNi_2Ge_2}$ and $\mathrm{EuNi_2Ge_2}$ designed to investigate the hypothesis developed in Chapter 4. The next chapter focuses on the metamagnetic structures of $\mathrm{TbNi_2Ge_2}$ compound studied with neutron diffraction. The last chapter gives a summary of this work and suggests possible future experiments that may be useful for improving the current state of knowledge of magnetic phenomena in these compounds.

2 EXPERIMENTAL TECHNIQUES

In the previous chapter earlier investigations of $R\mathrm{Ni}_2\mathrm{Ge}_2$ compounds using polycrystalline samples were summarized. It was established that such studies were not only inadequate for a complete understanding of the interplay of long-range order and anisotropy but also they are often erroneous. It was made clear that good-quality single crystals were necessary to make progress toward a better understanding of the complex Hamiltonian, involving several competing interactions discussed earlier, that governs magnetic phenomena in these compounds. In the first section of this chapter a brief description of the growth technique of the single-crystal samples used for the present study is given followed by a summary of their characterization methods.

A complete solution of a magnetic structure requires several steps [46]. Firstly, the magnetic wave vector(s), $\mathbf{q}$, needs to be found. Secondly, the ordered moment direction is determined. With the exception of uniaxial or collinear structure the direction of moments in general can vary from site to site in the case of complicated ordered states, such as a bunched spiral or a conical AF structure. Finally, the absolute values of the ordered moments must be evaluated. Depending on the complexity of the structure a single experimental technique is not sufficient to provide a complete knowledge of a magnetic structure. In the later sections of this chapter neutron and x-ray scattering techniques as utilized in this work are also reviewed in order to elucidate the complementarity of these methods in the study of magnetic structures and discuss the relevant cross-sections needed for model calculations.

Single Crystal Growth and Characterization

High-Temperature-Solution-Growth Technique

The series-wide study of $R\mathrm{Ni_2Ge_2}$ compounds was made possible by the availability of high-quality single crystals of these materials. These crystals were grown in the Ames Laboratory using a high-temperature-solution-growth technique details of which have been elucidated by Fisk and Remeika [47] and Canfield and Fisk [48]. Recent this technique has been applied to grow high-quality large-grain icosahedral R-Mg-Zn [49], and decagonal Al-Ni-Co [50] quasicrystals, respectively. A self-contained, and lucid description of this technique as employed for the growth of the tetragonal $R\mathrm{AgSb_2}$ compounds can be found in Ref. [51]. The steps involved for the growth of high-qulaity single crystals of the $R\mathrm{Ni_2Ge_2}$ compounds is briefly described below.

Single crystals of $R\mathrm{Ni_2Ge_2}$ are grown out of a ternary melt with elemental composition $R_6\mathrm{Ni_{47}Ge_{47}}$. This composition was found to be the optimum after several exploratory growths with different starting compositions. The elemental composition was placed in an alumina crucible in a stratified manner with Ge on the top and the R element on the bottom. Since Ge has the lowest melting temperature it melts first. As the molten Ge flows downward it starts to incorporate Ni and the R element with higher melting temperature into the melt. A second alumina crucible containing quartz wool is placed upside down over the growth crucible. The latter crucible acts as a strainer during later decanting of the melt. Both the crucibles are sealed in a quartz ampoule with a partial pressure of argon. The elemental mixture is then heated to a temperature of 1200 °C for a sufficient period of time for it to form a homogeneous liquid. The melt is then cooled over a period of approximately 100 hours to 1000 °C. Since Ni and Ge form 94% of the mixture and are present with equal proportion relative to each other the growth is essentially out of NiGe liquid above 1000 °C. An inspection of the Ge-Ni binary phase diagram reveals the liquidus to be at ∼960 °C at NiGe composition.

Therefore, in order to avoid the formation of any binary Ge-Ni compounds below this temperature the remaining melt is quickly decanted at 1000 °C using a centrifuge. With the exception of the radioactive Pm member of the series all others have been grown using this method. All these crystals have plate-like habits with clearly visible square facets perpendicular to the crystallographic $\hat{\mathbf{c}}$ axis. In the case of $EuNi_2Ge_2$ the plates do not have clear [1 0 0] facets.

X-Ray Diffraction Characterization

In order to confirm the crystal structures and to detect any second phase contaminations, large grains of single crystals were pulverized and x-ray powder diffraction patterns were taken at room temperature using Cu K_α radiation in a flat plate geometry. The powder pattern revealed sharp Bragg peaks. All the sharp intense peaks were indexed to the body-centered tetragonal crystal structure. Two *weak* spurious peaks with negligible weight were also observed in some growths originating from the elemental Ge and Ni present in the residual flux on the grain surfaces (or flux inclusions). The quality of the single crystals was then checked by x-ray diffraction measurements using an in-house Rigaku generator and a four-circle diffractometer. White radiation from a rotating Cu anode was monochromatized with a Ge (111) crystal. Another Ge (111) crystal was placed right before the detector to use as an analyzer. These measurements on single crystals showed high degree of structural order. Both the longitudinal and transverse widths ($\sim$0.003 Å^{-1} and $\sim$0.04°, respectively) of the observed (h 0 l), (h h l) and (0 0 l) type peaks were close to the resolution limit.

Thermodynamic and Transport Measurements

Single crystals of all the members of the series were characterized by bulk susceptibility and magnetization measurements using a superconducting quantum interference device (SQUID) magnetometer which provides a temperature range of 1.8-350 K and a

maximum field of 55 kG. With the exception of $SmNi_2Ge_2$, the low-field susceptibility in all the other members was found to obey a Curie-Weiss (CW) law at high temperature. The effective moments extracted from the CW fits were found to be in close agreement with the theoretical values of the localized trivalent rare earth moments for the Hund's rule ground state, except for $EuNi_2Ge_2$, which was found to be divalent. A summary of the salient magnetic properties of the Pr, Nd, Sm and Eu through Tm members has been given in Table 1.1. Low-field susceptibility measurements with the field applied along the $\hat{\mathbf{c}}$ axis ($\chi_{\parallel}$) and perpendicular to it ($\chi_{\perp}$) reveal significant magneto-crystalline anisotropy in the paramagnetic phase for all but the Eu and Gd compounds (Table 1.1, see also REf. [23]). This anisotropy, which is primarily determined by $\mathcal{H}_{\rm CEF}$, an important term in the Hamiltonian, could not be observed in previous studies on powder samples. Additional phase transitions below the ordering temperature (T_N) are also observed in all of them except for the Ho, Er, and Tm members (Table 1.1) where T_N itself is low because of the small de Gennes factor. Thus, additional transitions, if they exist, are expected to be at much lower temperature than 1.8 K for the first two and 1.5 K for the latter. In the case of Sm and Gd compounds, there is a third transition at 5.5 K and 18.5 K, respectively [23]. Susceptibility and magnetization measurements of the Eu, Gd, Tb, and Dy compounds are discussed in detail in the following chapters.

The zero-field in-plane resistivity ($\rho(T)$) of all the members of the series was measured as a function of temperature using the standard four-probe technique [23]. The high temperature resistivity varies linearly with T in the case of compounds with magnetically ordered ground states, consistent with their metallic behavior. The resistivity drops at T_N yielding a break, due to the loss of the spin-disorder scattering that is present in the paramagnetic phase. At the lower transition at T_t, the magnitude of the change of resistivity depends on the nature of the phase below T_t and may not produce any pronounced features such as the break observed at T_N. In the case of Pr, Nd, Gd, and Tb, however, a change of slope at T_t is indeed observed [23]. This is illustrated in Fig.

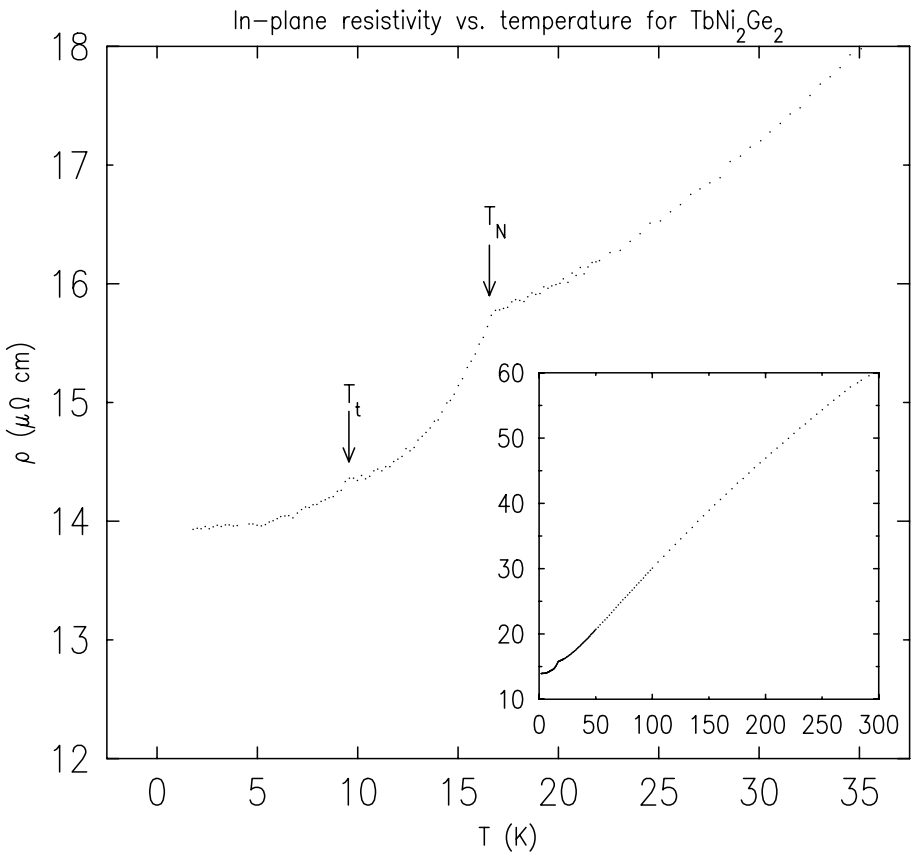

Figure 2.1 In-plane zero-field resistivity for $TbNi_2Ge_2$. Note the break at the transitions. The inset shows nearly linear behavior of $\rho(T)$at high temperature.

2.1 for $TbNi_2Ge_2$. There is a clearly visible break at both transitions as indicated by the arrows. As the inset shows $\rho(T)$ is nearly linear above $\sim$ 100 K. As mentioned above, for the Ho, Er, and Tm compounds T_t, if it exists, is expected to be lower than 1.8 K, the lowest temperature of the present measurements. For the remaining members, Sm and Dy, the change of $\rho(T)$ at T_t is barely discernible [23]. The residual resistance ratio (RRR) can be estimated from $\frac{\rho(300\mathrm{K})}{\rho(2\mathrm{K})}$, which is a measure of the degree of perfection of a crystal. The values of the RRR for the compounds with ordered ground state lie in the range of 3.2 to 6.7, which is quite good for intermetallic compounds. Magnetoresistance measurements were also carried on these compounds. Details of these measurements can be found in [23].

Neutron Diffraction

Neutron diffraction on powdered materials is an invaluable tool in the study of magnetic structures in condensed matter, since the magnetic and nuclear scattering cross-sections are of comparable strength. By comparing neutron diffraction patterns above and below the magnetic transition temperature, one can readily identify magnetic peaks assuming that the crystal structure remains the same through the transition. This is of definite advantage since polycrystalline materials can be grown relatively easily, while in many cases single crystals are not available.

For magnetic structures described by multiple propagation vectors, however, indexing magnetic peaks in a powder pattern unambiguously becomes a formidable, if not impossible task. Shirane [52], for example, has shown that even for a simple uniaxial magnetic structure it is not possible to determine completely the magnetic structure in a crystal of high symmetry (*i.e.* cubic, tetragonal and hexagonal) from powder data alone (except for some special cases), due to averaging of magnetic domains associated with equivalent directions of moments allowed by symmetry.

Diffraction measurements on single-crystal samples must be performed in order to determine the propagation vectors and the moment direction unambiguously. Once the wave vectors and the moment direction are known, the best magnetic configuration among competing models is found by comparing calculated magnetic peak intensities with observed ones. Because of the comparable nuclear and magnetic cross-sections of neutrons, the magnetic peaks can be put on an absolute scale with the nuclear reflections, giving the absolute value of the ordered moments.

A number of excellent textbooks on thermal-neutron diffraction techniques exist. For further details reference should be made to the texts by Bacon [53]. Marshall and Lovesey [54], and Squires [55]. respectively. A brief discussion of the elastic scattering cross-sections of neutrons, relevant to this work, is given below.

Scattering Cross-Section for Neutron Powder Diffraction

A summary of the intensity calculations along with the underlying assumptions is given below. The intensity of a nuclear powder peak (hkl) is given by:

$$\begin{aligned} I^N_{hkl} &= SC(\theta_B)\frac{j^N_{hkl}}{\sin(\theta_B)\sin(2\theta_B)} \\ &\times \left|\sum_n \bar{b}_n e^{i\mathbf{Q}\cdot\mathbf{r}_n} e^{-W_n(\mathbf{Q})}\right|^2, \end{aligned} \tag{2.1}$$

where S is an overall scale factor depending only on the experimental conditions; j^N_{hkl} is the multiplicity of the (hkl) reflection; $\bar{b}$ is the bound scattering amplitude of neutrons averaged over nuclear isotopes and, where necessary, over their nuclear spin states; $\mathbf{Q} = \mathbf{k}' - \mathbf{k}$ is the scattering vector; W_n is the Debye-Waller factor of a particular nucleus at $\mathbf{r}_n$; and the sum is performed over all the nuclei in the unit cell. In order to compare with the observed intensities from a powder pattern, one needs to account for absorption, extinction and preferred orientations. All these factors are lumped into the correction factor, $C(\theta_B)$. For the calculations in this work, the corrections necessary for strain broadening are ignored. For a finely ground powder, primary extinction of neutrons can also be ignored. Although secondary extinction and preferred orientations may not be negligible, no attempts have been made to correct for them. In the case of $TbNi_2Ge_2$, a small absorption correction mostly due to Tb was found to be negligible [44]. It is noted here that in the case of Sm, Eu and Gd, the neutron absorption cross-section is very large, 5670, 4565 and 48890 barns, respectively, compared to that in Tb, which is only ~23 barns [56]. Compounds containing these elements, such as $EuNi_2Ge_2$ and $GdNi_2Ge_2$, are neutron opaque, making their study with neutron diffraction very difficult. Since the neutron diffraction measurements on powder samples were taken at low temperature (~ 10 K), Debye-Waller factors were also ignored. Thus, the intensities of nuclear peaks

were calculated according to:

$$I^N_{hkl} = S\frac{j^N_{hkl}}{\sin(\theta_B)\sin(2\theta_B)}\left|\sum_n \bar{b}_n e^{i\mathbf{Q}\cdot\mathbf{r}_n}\right|^2. \tag{2.2}$$

There is only a temperature-independent overall scale factor, S, to fit, which is determined from the data in the paramagnetic phase. In the case of $TbNi_2Ge_2$, discussed later in detail, the scale factor was determined by comparing measured intensities of nuclear peaks at 20 K to those calculated via Eqn. 2.2 (see Appendix B). This scale factor is later used to put the magnetic peaks on an absolute scale, which allows the determination of the absolute values of the ordered moments.

In general, calculations of intensities for magnetic peaks are quite complicated. However, for collinear structures calculations simplify to the following expression [52]:

$$\begin{aligned} I^M_{hkl} &= \frac{S}{N_m^2}\frac{j^M_{hkl}}{\sin(\theta_B)\sin(2\theta_B)}\langle q^2\rangle\left(\frac{\gamma e^2}{2m_e c^2}\right)^2 \\ &\times \left|\sum_j \langle\mu_j\rangle f_j(Q) e^{i\mathbf{Q}\cdot\mathbf{r}_j}\right|^2. \end{aligned} \tag{2.3}$$

Here N_m is the number of conventional unit cells comprising the magnetic unit cell, which can differ from the conventional cell, j^M_{hkl} is the multiplicity of the (hkl) reflection, γ is the neutron gyromagnetic ratio, $\langle\mu_j\rangle$ is the thermal average of magnetic moment (in units of Bohr magneton, μ_B) at the jth magnetic site. The magnetic form factor, $f_j(Q)$, of the j-th ion was calculated in the dipole approximation according to :

$$f_j(Q) = \langle j_0(Q)\rangle + C_2\langle j_2(Q)\rangle, \tag{2.4}$$

where C_2 is a constant depending on the Landé g-factor. Values of $\langle j_l(Q)\rangle$ were calculated using analytic expressions given in Ref. [56].

In the case of powder neutron diffraction, an average of magnetic interaction vector, $\mathbf{q} = \hat{\mathbf{e}}(\hat{\mathbf{e}}\cdot\hat{\boldsymbol{\mu}}) - \hat{\boldsymbol{\mu}}$, over equivalent spin directions needs to be performed which leads to ambiguity in the determination of the moment direction as mentioned above. This

average is given by [52]:

$$\langle q^2 \rangle = 1 - \langle \cos^2(\eta) \rangle, \tag{2.5}$$

where η is the angle between the moment direction, $\hat{\mu}$, of the atoms and the unit scattering vector, $\hat{\mathbf{e}}$. These averages for various crystal systems are given in Ref. [52]. For the tetragonal system with ordered moments along the $\hat{\mathbf{c}}$ axis the average is :

$$\langle q^2 \rangle = 1 - \left(\frac{l \mathrm{d}_{hkl}}{c} \right)^2, \tag{2.6}$$

where d_{hkl} and c are the planar spacing and the lattice parameter, respectively.

Observed intensities can be obtained by simple numerical integration of the Bragg peaks corrected for background. When there is significant peak overlap, intensities of all the unresolved Bragg peaks are included.

Cross-Section for Neutron Scattering from Single Crystals

The primary advantages of using single crystals are the unambiguous determination of the magnetic modulation vectors, as well as the moment directions in many cases, and the order-of-magnitude increase in the scattering intensity. This large gain in intensity makes it easier to observe weak superlattice peaks that can remain undetected in powder diffraction measurements. Since, in general, only one Bragg peak is observed at a time with single crystal samples, the widths of these peaks are resolution limited, resulting in a much more precise determination of the wave vectors. In the case of powder samples, there are often several sets of overlapping peaks, which degrade the precision with which wave vectors and the integrated intensities can be extracted. Finally, metamagnetic or magnetic-field-induced structures can only be studied on single crystals, which is one of the primary objectives of this work. Diffraction from single crystals, however, suffers from extinction effects, which reduce integrated intensities of Bragg reflections. This reduction may lead to erroneous models of ordered states if it is not corrected for. These

effects are sample-dependent and vary significantly with intensity, as well as the **Q** of Bragg reflections for a given neutron energy. Therefore, *a priori* calculations for these effects can not be performed with confidence. It is possible to assess the importance of these effects by comparing intensities as a function of neutron energy, which is seldom done. However, it is far more practical to measure experimentally these effects for a given crystal structure. Integrated intensities are calculated, as discussed below, for a large number of nuclear peaks and compared with the measured intensities corrected for geometric effects and absorption, where necessary. The best fit between the observed and calculated intensities is obtained by varying an extinction factor associated with each reflection. In general, the stronger Bragg peaks are affected the most by extinctions, yielding large correction factors for these peaks. These extinction factors can be used to obtain interpolated values needed to correct the *calculated* intensities of magnetic peaks, appearing elsewhere in reciprocal space, for a given model to obtain agreement with the observed intensities.

For a single-crystal sample the integrated intensity of a magnetic peak is given by [46, 17]:

$$I^M(\mathbf{Q}) = \mathbf{F}\cdot\mathbf{F}^* - \frac{[\mathbf{F}\cdot\mathbf{Q}][\mathbf{F}^*\cdot\mathbf{Q}]}{|\mathbf{Q}|^2}, \tag{2.7}$$

where the vector magnetic structure factor, **F**, without the Debye-Waller factor is shown below

$$\mathbf{F} = \left(\frac{\gamma e^2}{2m_e c^2}\right)\sum_j \langle\boldsymbol{\mu}_j\rangle f_j(Q) e^{i\mathbf{Q}\cdot\mathbf{r}_j}. \tag{2.8}$$

The above expressions were used to calculate intensities in the neutron diffraction studies of metamagnetism in $TbNi_2Ge_2$ presented in Chap. 6.

X-Ray Resonant Exchange Scattering (XRES)

The first prediction that x-ray scattering can be used to study magnetic structures of condensed matter was made by Platzman and Tzoar in 1970 [57]. This was experimentally verified in 1972 by de Bergevin and Brunel [58] in their pioneering work on NiO, using an x-ray tube source. However, significant progress in the study of magnetism using x-ray scattering had to wait almost a decade for the development of synchrotron radiation sources. The availability of high flux, polarized photon beam, and high **Q**-resolution opened up a new field of research. In 1985, Blume [59], using a second-order perturbation theory, suggested the resonant contribution to magnetic scattering of x-rays when the incident energy is tuned to some absorption edge. The first observation of the resonant scattering sensitive to magnetization was observed by Namikawa and co-workers [60] at the Ni K-edge. In the same year, Gibbs and co-workers made the first non-resonant x-ray scattering studies on Ho [61] and pioneered the investigations of elemental rare earth magnetism using x-rays. In 1988, this work was complemented by an extensive study of polarization and resonance properties of magnetic x-ray scattering in the same material [62]. This experiment prompted a detailed theoretical work by Hannon and co-workers [63] who derived the complicated dependence of the resonant cross-section on local magnetization direction and the polarization state of the primary and secondary photons. According to this work, the resonant magnetic scattering results from electric multipole transitions. In the case of rare earths, such transitions involve exciting an electron from a core level (such as $2p$) to an unoccupied state above the Fermi level, due to exclusion principle, (such as $5d$), followed by the de-excitation and re-emission of the absorbed photon. Hence, the name is x-ray resonant exchange scattering (XRES). The scattering is sensitivite to magnetization because the spin-orbit coupling or the exchange interaction splits the core levels and/or the excited states. In the magnetically ordered states such effects at different sites are correlated giving rise

to Bragg peaks. The XRES cross-sections have been presented in a readily usable form by Hill and McMarrow [64]. The XRES cross-section pertinent to this work is discussed below.

The major advantage of using XRES is the superior **Q**-resolution available, allowing one to measure magnetic wave vectors with an order-of-magnitude better precision than that available with conventional neutron diffraction methods and observe subtle changes in periodicities, as is often the case at phase transitions. The high **Q**-resolution also makes it possible to study magnetic structures on a mesoscopic scale in excess of 1000 Å. XRES studies of the rare earths are performed at the L_{II} and L_{III} edges (see below) which lie in an energy range of 6-10 keV, which is convenient for diffraction studies using synchrotron radiation. In addition, small samples, as well as materials containing elements such as B, Sm, Eu and Gd with high neutron capture cross-sections, can be conveniently studied with this technique. Since the cross-sections of resonant (and non-resonant) scattering are order-of-magnitude smaller compared to that of the Thomson scattering, extinction effects are negligible, which facilitates a more accurate integrated intensity measurements on single crystals. Furthermore, an *ab initio* determination of moment direction can also be done in an element-selective way [65, 66, 67, 44, 43]. This is of definite advantage in systems containing two or more magnetic species. Whereas neutrons simultaneously probe all the magnetic ions, XRES is primarily sensitive to the resonating atoms. Thus, XRES provides the opportunity to study different magnetic sublattices independently. Recently, the XRES technique for determining the moment direction by measuring the **Q**-dependence of integrated intensities of magnetic Bragg peaks has been developed and applied with success on the series-wide investigation of magnetic structures in the $R\mathrm{Ni_2B_2C}$ compounds [65, 66, 67]. In the following, the procedure involved in determining the ordered moment direction using XRES is described.

In order to use resonance phenomena to study rare earth magnetism, the incident photon energy is tuned to the appropriate L-edge of the rare earths, which is L_{II} for the

light rare earths, including Gd, and L_{III} for the heavy rare earths, respectively. With the energy chosen, extensive searches for superlattice peaks along various symmetry directions of the Brillouin zone, as allowed by the scattering geometry, are carried out. Once the superlattice peaks are found, the energy where the peak shows the maximum is identified as the resonant energy (E_{res}). The observation of a maximum in the energy scan is consistent with the magnetic origin of a superlattice peak. In order to utilize the maximum resonant enhancement, the photon energy is tuned to E_{res}, which is typically within 5-6 eV of the absorption edge. In order to determine the moment direction associated with the resonating ions, integrated intensities of a set of magnetic Bragg peaks are measured carefully and model calculations are compared with their observed **Q**-dependence.

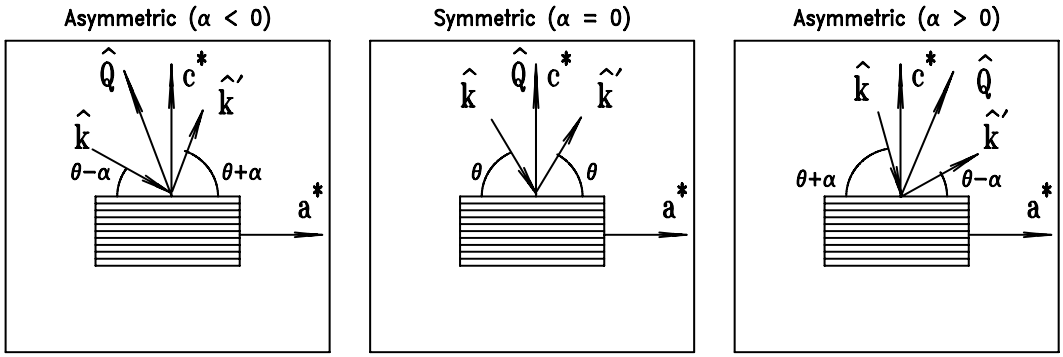

Figure 2.2 Scattering geometries and sample orientations for the integrated intensity measurements.

The measurements of intensities are carried out in the flat plate geometry, which also allows a larger number of asymmetric reflections to be accessed with simple geometric corrections. In the case of $TbNi_2Ge_2$, discussed in the next chapter, altogether 19 magnetic peaks were measured, which is comparable to and, in some cases, larger than, the number of resolved magnetic peaks observed in powder neutron diffraction patterns. The sample orientations and various scattering geometries are shown in Fig. 2.2. The samples are cut and polished to be of rectangular shape with small width. This narrow

geometric shape ensures that at all angles of measurements the beam profile is larger than the sample dimension in the scattering plane. In addition, single crystals grown by high-temperature-solution-growth technique have residual flux on their surfaces. By polishing the crystals the left-over flux is also removed, which increases reflectivity. Next, in order to accept the full intensity, the detector slits are opened up as described in Ref. [65]. Finally, the integrated intensities are collected by performing a transverse scan through the magnetic peaks. This scan is done by varying the Bragg angle (θ, as shown in Fig. 2.2) over an angular range (typically $\pm 0.1^{\circ}$ centered on a Bragg peak) where intensity is above the background level, at a constant rate as the scattered photons are counted. For the typical scattering geometries and sample orientations shown in Fig. 2.2, the integrated reflection of a magnetic Bragg peak takes the following form [63, 65, 64]:

$$\begin{aligned} I_{hkl}^{XRES} &\propto \frac{\sin(\theta_B+\alpha)\sin(\theta_B-\alpha)}{2\mu\sin(\theta_B)\cos(\alpha)\sin(2\theta_B)} \\ &\times \Big|\sum_{n\epsilon\epsilon'}\big(f_n^{non-res}[\mathbf{k},\hat{\epsilon},\mathbf{k}',\hat{\epsilon}',\mathbf{L}_n(\mathbf{Q}),\mathbf{S}_n(\mathbf{Q})] \\ &+ F_n^{XRES}[\mathbf{k},\hat{\epsilon},\mathbf{k}',\hat{\epsilon}',\hat{z}_n]e^{i\mathbf{Q}\cdot\mathbf{r}_n}e^{-W_n(\mathbf{Q})}\Big|^2, \end{aligned} \tag{2.9}$$

where the non-resonant term is also included for completeness. This expression is valid for symmetric ($\alpha = 0$) as well as for asymmetric ($\alpha \neq 0$) geometries (see Fig. 2.2) where α is the "asymmetry" angle between the surface normal, $\hat{\mathbf{n}}$, which is $\hat{\mathbf{c}}$ for all the sample geometries used in this work, and the scattering vector, $\mathbf{Q} = \mathbf{k}' - \mathbf{k}$. The Lorentz velocity factor, $\frac{1}{\sin(2\theta_B)}$, is also included. The rest of the angular factors are needed to account for the fraction of the beam intercepted by the sample and absorption [65, 68]. The non-resonant and resonant scattering amplitudes depend on the wave vector and the polarization of incident ($\mathbf{k}$, $\hat{\epsilon}$) and scattered ($\mathbf{k}'$, ϵ') x-ray beams. The non-resonant scattering amplitude has different angular dependence for orbital moment, $\mathbf{L}_n(\mathbf{Q})$, and spin moment, $\mathbf{S}_n(\mathbf{Q})$, respectively. The resonant scattering, on the other hand, depends on the direction, $\hat{z}_n$, of the net magnetic moment at the nth site. The exact expressions for the non-resonant cross-sections for different incident and scattered photon polariza-

tion states have been worked out by Blume and Gibbs [69]. However, since the observed non-resonant scattering away from resonance was quite small in all the measurements pertaining to this work, at resonance this contribution can be neglected. The polarization of the primary beam in the orbital plane of the electrons of a synchrotron source is horizontal (90%) which corresponds to σ-polarization with respect to the vertical scattering geometry used. For the electric-dipole-electric-dipole ($E1$) transition (which is the dominant term in the scattering cross-section) only $\sigma \rightarrow \pi$ scattering contributes [63, 64]. Due to the low temperature of the measurements in this work the Debye-Waller factors are assumed negligible and can also be dropped. Thus, the XRES expression for the integrated intensity of a magnetic peak reduces to [64]:

$$I_{hkl}^{XRES} \propto \frac{\sin(\theta_B + \alpha)\sin(\theta_B - \alpha)}{2\mu \sin(\theta_B)\cos(\alpha)\sin(2\theta_B)} \sum_i \left| \hat{k}' \cdot \hat{z}_i \right|^2 , \tag{2.10}$$

where the summation is over all the magnetic domains associated with equivalent moment directions. From the above equation one immediately sees that only the component in the scattering plane can be probed by $E1$ resonant scattering. This is in contrast to the case with neutrons where the moment component normal to the scattering vector is probed, or non-resonant x-ray scattering where primarily the component perpendicular to the scattering plane is measured.

In summary, neutron diffraction and magnetic x-ray scattering, in particular XRES, are complementary to each other. Both are very useful in the study of magnetic structures on a macroscopic scale. It is not difficult to identify wave vectors using neutron diffraction on single crystals. This is because nuclear and magnetic scattering cross-sections are of comparable strength. On the other hand, the availability of high **Q**-resolution, the possibility to study neutron-opaque materials with ease, and the elemental selectivity make XRES a powerful probe of magnetic materials. With the availability of the new generation synchrotron sources this technique is becoming increasingly more convenient to use. Finally, with the knowledge of wave vectors and moment direction,

powder neutron diffraction can be used to determine the absolute values of the ordered moments. The expressions for the scattering cross-sections presented in this chapter are used later in model calculations.

3 MAGNETIC STRUCTURES OF ANISOTROPIC SYSTEMS: $TbNi_2Ge_2$ AND $DyNi_2Ge_2$

In this chapter experimental determination of the zero-field magnetic structures of $TbNi_2Ge_2$ and $DyNi_2Ge_2$ compounds will be presented. These neighboring isostructural compounds provide the opportunity to observe the changes brought about by the difference in the anisotropic $4f$ moments while keeping the conduction electron count or band filling fixed. The determination of their magnetic structures is not only a primary focus of the current work, but this knowledge will also provide the foundation for the future studies of the field-induced structures later.

$TbNi_2Ge_2$

Previous Investigations of the Magnetic Structures

Pinto and co-workers have studied a large number of RT_2X_2 rare earth intermetallic ternaries, including $TbNi_2Ge_2$, using neutron diffraction from polycrystalline samples [38]. In $TbNi_2Ge_2$ they observed two transitions, at $T_N = 16$ K and $T_t = 9$ K, respectively. According to their work the structure below T_N is incommensurate. However, a complete determination of the structures was not carried out.

Later, in a more detailed study, Bourée-Vigneron [39] also found two transitions, at $T_N = 17$ K and $T_t = 10.25$ K, respectively. According to this work, the magnetic structures in both phases are commensurate with Tb moments aligned with the $\hat{\mathbf{c}}$ axis.

The higher-temperature structure was shown to be a *longitudinal amplitude modulated* (AM) wave with wave vector $(0\ 0\ \frac{3}{4})$[1] in reciprocal lattice units (r.l.u.). Below T_t, additional satellite peaks, corresponding to $(0\ 0\ \frac{1}{4})$ related to $(0\ 0\ \frac{3}{4})$, and a new wave vector $(\frac{1}{2}\ \frac{1}{2}\ \frac{1}{2})$, also develop. In this phase, the $(0\ 0\ \frac{3}{4})$ structure is partially squared-up AM, similar to that above T_t. In addition, there are antiferromagnetically ordered Tb planes to account for the $(\frac{1}{2}\ \frac{1}{2}\ \frac{1}{2})$ modulation. A complete magnetic unit cell of the model structure for this phase is not given in Ref. [39]. Refinement of this model, however, leads to values of the Tb^{3+} moment up to 12.45±0.35 μ_B at some sites, which is 40% larger than the saturated value of 9.0 μ_B expected for the ionic moment.

Although it is possible to have an excess moment associated with the spin polarization of the conduction band electrons [70], such a large enhancement of the moment is surprising. To illustrate the magnitude of the polarization contribution, one can consider the isostructural $GdRh_2Si_2$ compound where the enhancement is solely due to exchange interactions since the Gd^{3+} ground state ($^8S_{\frac{7}{2}}$) is unaffected by CEF effects. In this case the polarization of the 5d conduction band contributes a maximum of 0.28±0.03 μ_B in excess of the Gd moment [71].

Susceptibility and Magnetization

The temperature dependence of the low field susceptibility (χ(T)) with applied field parallel ($\mathbf{H} \parallel \hat{\mathbf{c}}$) and perpendicular ($\mathbf{H} \perp \hat{\mathbf{c}}$) to the $\hat{\mathbf{c}}$ axis was found to be strongly anisotropic. From cusps in the susceptibility two transitions were identified which are indicated in Fig. 3.1(a). The paramagnetic-to-antiferromagnetic (AF) transition occurs at 16.7 K (T_N). The second transition is at a lower temperature of 9.6 K (T_t) [23, 44]. These transition temperatures are consistent with previously published results [38, 39].

[1] According to the paper (Ref. [39]) the modulation vector is $(0\ 0\ \frac{1}{4})$ with respect to the Brillouin zone (BZ) boundary. The definition of the propagation vectors adopted in this work is made with respect to the BZ center (Γ) which retains the full point group symmetry of the space group of the underlying crystal structure.

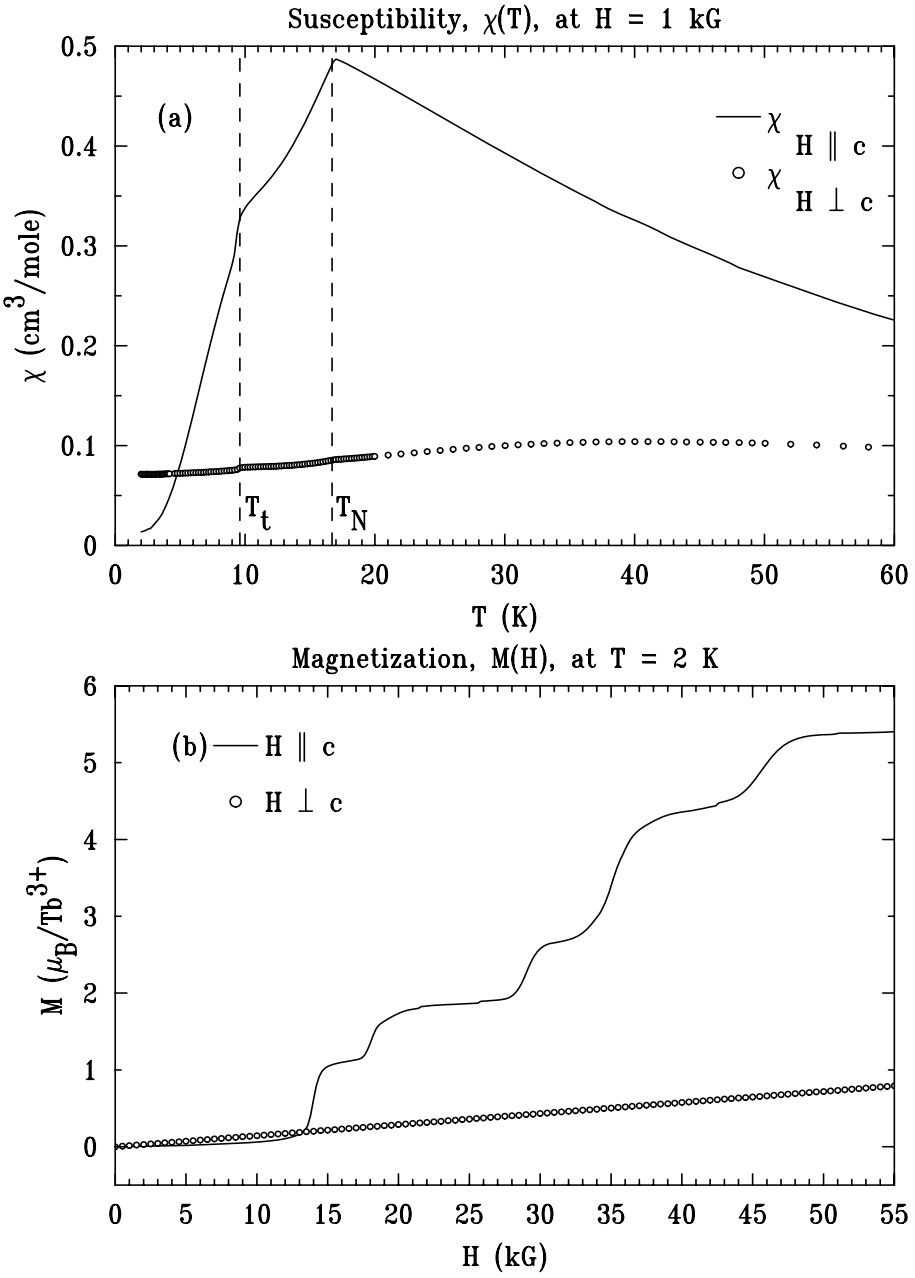

Figure 3.1 (a) Susceptibility as a function of temperature at 1 kG and (b) magnetization as a function of field at 2 K of $TbNi_2Ge_2$ single crystal.

Perhaps the most interesting behavior was found in the magnetization (M(**H**)) as a function of field applied along the $\hat{\mathbf{c}}$ axis at 2 K (Fig. 3.1(b)). As the field was increased from zero to its maximum value, a sequence of well-defined steps appeared. Up to 55 kG, five distinct transitions were observed (at 14 kG, 18.1 kG, 29 kG, 35 kG and 45.8 kG, respectively). When the magnetization data were normalized to magnetic moment per Tb^{3+} ion, the sequence of magnetization values in the metamagnetic phases was approximately $\frac{1}{8}$, $\frac{1}{5}$, $\frac{3}{10}$, $\frac{1}{2}$ and $\frac{3}{5}$ of the saturation value of 9.0 μ_B. In Ref. [23] a transition to a seventh phase at 59 kG with saturated 9.0 μ_B per Tb^{3+} is found which persists up to the maximum attainable field of 180 kG. Also, M(**H**) is hysteretic and on field ramping down from the maximum value two more states are found, giving up to nine well defined phases. When the applied field was in the basal plane, however, magnetization did not exhibit any transitions.

This anisotropic behavior is similar to that observed in the isostructural $TbNi_2Si_2$ compound [25, 26]. In zero field, $TbNi_2Si_2$ is an *incommensurate* AM antiferromagnet below 15 K. At about 9 K, the structure locks into a *commensurate equal moment* (EM) phase (see Refs. [25, 26] and references therein). In both the phases Tb moments are aligned with the $\hat{\mathbf{c}}$ axis. The most striking behavior was found [25] at 1.3 K, where five metamagnetic transitions were seen in an external field applied along the $\hat{\mathbf{c}}$ axis, although these transitions were not as clearly resolved as in Fig. 3.1(b), suggesting that $TbNi_2Ge_2$ is a better candidate for study. Neutron diffraction on a single crystal of $TbNi_2Si_2$ in a field revealed a rich phase diagram [26]. Among various phases, a field induced transition into an AM structure from an EM phase was reported. Based on the similar magnetic properties and the isostructural relationship a rich magnetic phase diagram for $TbNi_2Ge_2$ can be expected as well. Differences are likely to arise, however, due to the change in the environment of the Tb atoms brought about by Ge substitution for Si and by the differences in the lattice parameters, since the oscillatory exchange interactions are very sensitive to magnetic ion-ion separation. Also, the number and clarity of states make

$TbNi_2Ge_2$ an ideal system to study metamagnetic structures. But first it is vital to have a clear understanding of the zero-field structures. This is the focus of the rest of this section.

Determination of Magnetic Wave Vectors: Neutron Diffraction from a Single Crystal

The neutron scattering measurements on a single crystal of $TbNi_2Ge_2$ were carried out at the H4M spectrometer of High-Flux Beam Reactor (HFBR) at Brookhaven National Laboratory. Neutrons with energies of 14.7 meV and 30.5 meV were used. Most of the work was carried out at 30.5 meV with collimator settings of $40' - 40' - 40' - 40'$. A pyrolytic graphite (PG) filter was placed after the sample to eliminate second harmonic ($\frac{\lambda}{2}$) contamination of the beam. The largest crystal (166 mg) of the same batch as that used for the susceptibility measurements was chosen. No special preparation of the sample was necessary.

The single crystal was aligned with the $[h\ h\ l]$ zone in the scattering plane in order to identify all modulation vectors unambiguously. At 20 K, above T_N, as determined from the susceptibility data, scans along various symmetry directions in this zone showed only nuclear peaks consistent with the body-centered crystal structure (*i.e.* $h+k+l = 2n$ where n is an integer). Below T_N but above T_t, magnetic satellite peaks $(h\ h\ 0) \pm \boldsymbol{\tau}_1$ where $\boldsymbol{\tau}_1 = (0\ 0\ \frac{3}{4})$ developed. The absence of any magnetic peaks of the form $(0\ 0\ l) \pm \boldsymbol{\tau}_1$ indicates that the ordered moment direction is along the $\hat{\mathbf{c}}$ axis.

At 4.7 K, below the second transition at T_t, as determined from the susceptibility data, additional superlattice peaks associated with $\boldsymbol{\tau}_2 = (\frac{1}{2}\ \frac{1}{2}\ 0)$ and $\boldsymbol{\tau}_3 = (\frac{1}{2}\ \frac{1}{2}\ \frac{1}{2})$ were observed. A weak modulation, $\boldsymbol{\tau}_1' = (0\ 0\ \frac{1}{4})$, related to $\boldsymbol{\tau}_1$ also developed, indicating a squaring-up of the structure. No other modulations in this zone were found. Again, the absence of $\boldsymbol{\tau}_1$ and $\boldsymbol{\tau}_1'$ magnetic satellites of $(0\ 0\ l)$ nuclear peaks implied that the ordered moments associated with these modulations are aligned with the $\hat{\mathbf{c}}$ axis. How-

ever, there remains the possibility of a component of the ordered moments in the basal plane associated with $\boldsymbol{\tau}_2$ and $\boldsymbol{\tau}_3$ modulations which is discussed below.

The integrated intensities ('order parameters') of various magnetic Bragg peaks corresponding to (1 1 0)+$\boldsymbol{\tau}_1$, (0 0 0)+$\boldsymbol{\tau}_2$ and (0 0 0)+$\boldsymbol{\tau}_3$ are shown in Fig. 3.2 as a function of temperature. For comparison the integrated intensity of the (1 1 2) nuclear peak is also shown which has no significant variation as the temperature is changed. The intensity of the $\boldsymbol{\tau}_1$ satellite increases from zero at T_N and shows a marked discontinuity in its slope at T_t. Simultaneously, magnetic peaks corresponding to $\boldsymbol{\tau}_2$ and $\boldsymbol{\tau}_3$ appear at T_t. These show very similar dependence on temperature, suggesting that they most likely originate from the same features of the structure. The transition temperatures obtained by modeling the magnetic order parameters by Brillouin type functions ($B_{J=6}(\mid T - T_c \mid)$ where T_c is transition temperature, see Fig. 3.2) are $T_N = 16.8 \pm 0.2$ K and $T_t = 9.8 \pm 0.3$ K, respectively, in close agreement with those determined by susceptibility measurements. The large enhancement of the integrated intensity of the $\boldsymbol{\tau}_1$ satellite below T_t should be noted.

Assuming a common origin for the symmetry inequivalent modulations $\boldsymbol{\tau}_2$ and $\boldsymbol{\tau}_3$, as suggested by the intensity measurements, the intensities of some satellites corresponding to these wave vectors can be compared to infer the ordered moment direction associated with them. It is found that the intensities of these noncollinear Bragg peaks fell off as $I_{(\frac{3}{2}\frac{3}{2}0)} > I_{(\frac{3}{2}\frac{3}{2}\frac{1}{2})} > I_{(\frac{3}{2}\frac{3}{2}\frac{3}{2})}$ at a faster rate than the decrease that would be expected from the change in the magnetic form factor of Tb^{3+}. This behavior, combined with the large anisotropy in the susceptibility and the low temperature magnetization measurements, suggests that the direction of ordered moments associated with these modulations in the low temperature phase is also along the $\hat{\mathbf{c}}$ axis.

The temperature dependence of the weak $\boldsymbol{\tau}_1'$ satellite is shown in Fig. 3.3. It is seen that the intensity of this satellite drops off at a much faster rate with temperature and

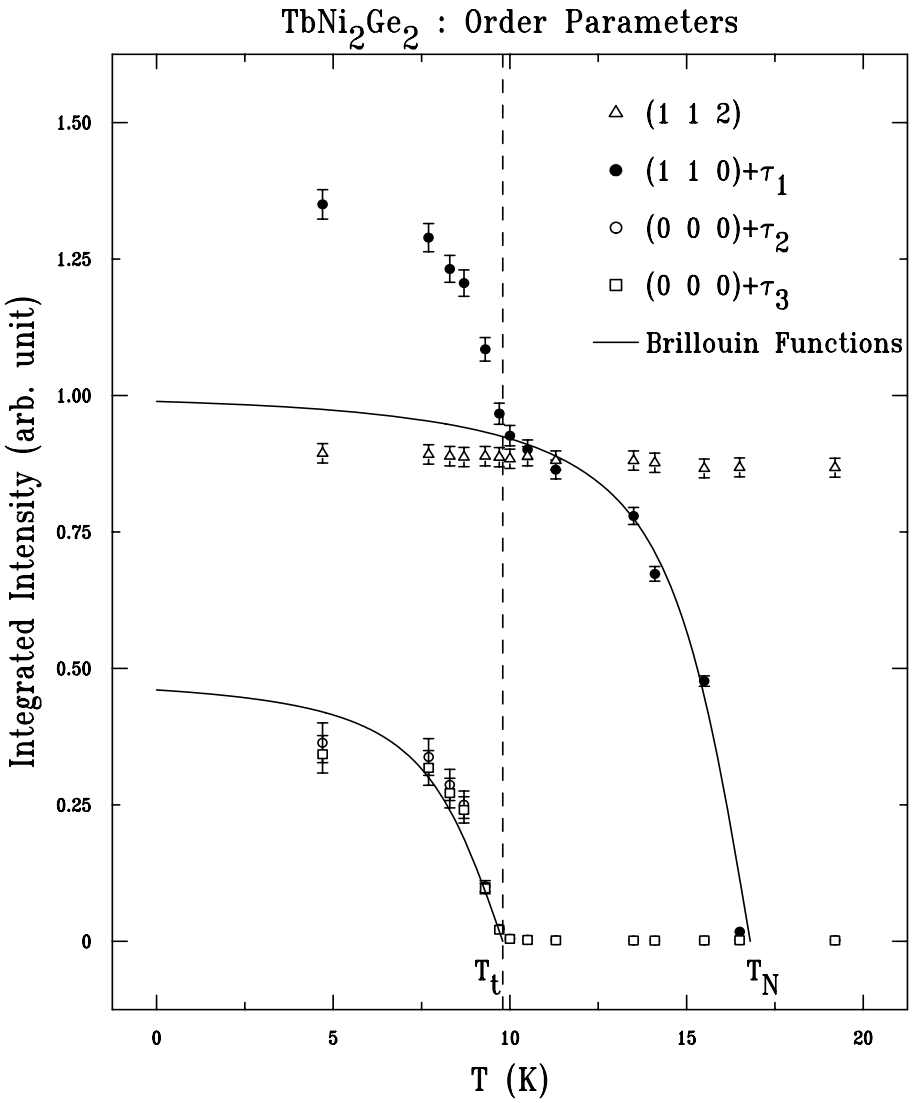

Figure 3.2 Temperature dependence of various magnetic reflections measured by neutron diffraction ($E_{neutron}$ = 14.7 meV) on a single crystal. Data were collected on raising the temperature.

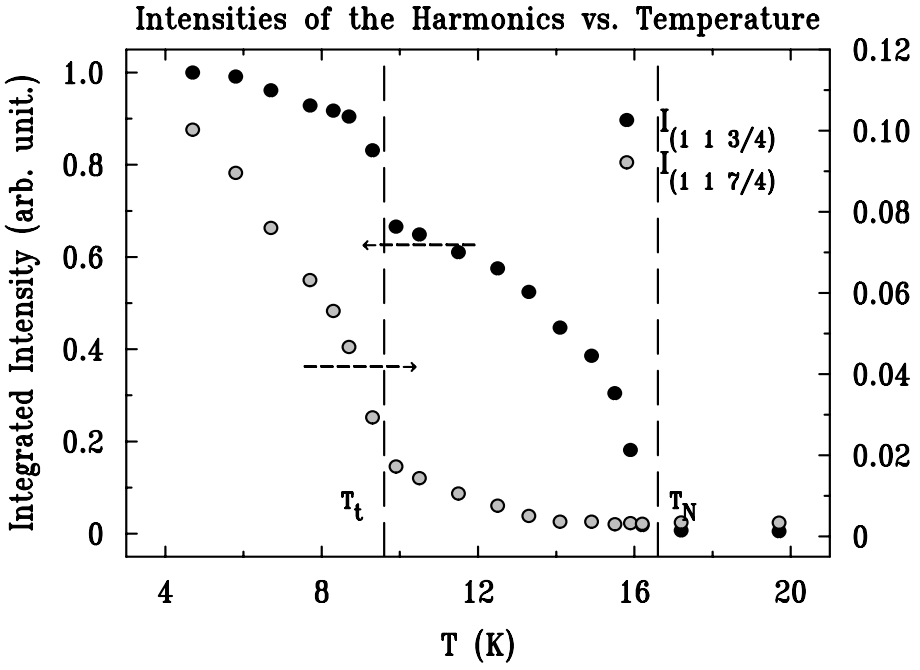

Figure 3.3 Temperature dependence of (1 1 0)+$\boldsymbol{\tau}_1$ and (1 1 2)-$\boldsymbol{\tau}_1'$ as measured by neutron diffraction ($E_{neutron}$ = 30.5 meV) on a single crystal. Both the scales correspond to the same arbitrary unit. Data were collected on raising the temperature.

becomes negligibly small above T_t. At the lowest temperature of 4.7 K, the ratio $\frac{I_{(00\frac{1}{4})}}{I_{(00\frac{3}{4})}} \approx \frac{1}{10}$ which compares favorably with $\left(\frac{1}{3}\right)^2$ expected for the ratio of the third-order and the fundamental components of a perfect square wave.

The data can be summarized as follows: below T_t, there are three magnetic modulation vectors, namely, $\boldsymbol{\tau}_1 = (0\ 0\ \frac{3}{4})$, $\boldsymbol{\tau}_2 = (\frac{1}{2}\ \frac{1}{2}\ 0)$ and $\boldsymbol{\tau}_3 = (\frac{1}{2}\ \frac{1}{2}\ \frac{1}{2})$. The weak modulation $\boldsymbol{\tau}_1' = (0\ 0\ \frac{1}{4})$ is found to be the third harmonic of $\boldsymbol{\tau}_1$. For $T_t < T < T_N$, however, there is only one propagation vector, $\boldsymbol{\tau}_1$. Although $\boldsymbol{\tau}_2$ and $\boldsymbol{\tau}_3$ are not related by symmetry, similarities in temperature dependence of their integrated intensities suggests a common origin. In both the phases, the ordered moments are parallel to the $\hat{\mathbf{c}}$ axis.

X-Ray Resonant Exchange Scattering

According to the neutron diffraction studies there is a discrepancy about the nature of the long-range order just below T_N. Whereas the current work just presented found $\boldsymbol{\tau}_1$ to be commensurate in agreement with Bourée-Vigneron's [39] result, due to low **Q**-resolution of neutron scattering techniques the possibility of incommensuration as reported by Pinto and co-workers [38] needs to be checked since incommensurate modulation was found in the other members of the series (see Table 1.1). The higher **Q**-resolution available with x-ray resonant exchange scattering (XRES) techniques can be utilized to determine $\boldsymbol{\tau}_1$ more precisely. In addition, since XRES, unlike neutron diffraction, is element selective, the moment direction associated with the Tb sublattice can be determined independently [63, 64]. In recent experiments this technique has been successfully used to determine moment directions in the Gd, Nd and Sm members of the $R\mathrm{Ni_2B_2C}$ intermetallic compounds [67, 66].

These studies were performed on the X22C beamline at the National Synchrotron Light Source. This beamline utilizes a Ni-coated toroidal mirror to focus the x-ray beam at the sample position and reject higher harmonics in the incident beam. The incident energy was selected using a double-bounce Ge(111) monochromator with an energy resolution of approximately 10 eV. The focused monochromatic beam at the sample position had a spot size of approximately 1 mm $\times$ 1 mm. In this configuration the flux was approximately 10^{11} photons/sec at 8 KeV.

For the XRES experiment, a platelet of the $\mathrm{TbNi_2Ge_2}$ crystal, from the same batch as that used for neutron diffraction measurements, was mechanically polished perpendicular to the $\hat{\mathbf{c}}$ axis to eliminate surface contamination from the residual flux and to increase the reflectivity. The sample was cut perpendicular to the $\hat{\mathbf{a}}$ axis to have the final shape of a long narrow rectangular block with approximate dimensions of $5.0\times1.0\times0.5$ mm^3. This shape allowed Bragg peaks in the $[h\ 0\ l]$ zone to be conveniently studied. The narrow

profile also ensured that the sample was completely bathed in the incident beam at all angles. The crystal was sealed inside a Be can filled with He gas and cooled in a closed cycle Heliplex-4 cryostat with a base temperature of 3.7 K. Integrated intensities were measured using a liquid-nitrogen-cooled Ge solid state detector. The sample mosaic at (0 0 6) was approximately 0.05°.

In order to use the resonant enhancement of the magnetic peaks, the primary beam energy was tuned to the L_{III} absorption edge of Tb where resonant enhancement is expected to be the largest [63, 72, 73, 62]. Above T_N, only charge peaks consistent with the body-centered tetragonal structure were observed. Below T_t, careful scans along [0 0 1] direction revealed superlattice peaks corresponding to $\boldsymbol{\tau}_1$ and $\boldsymbol{\tau}_1'$ as was found in neutron diffraction measurements. For $T_t < \mathrm{T} < T_N$, however, the $\boldsymbol{\tau}_1'$ satellite disappeared and $\boldsymbol{\tau}_1$ was observed to shift toward (0 0 0.758) (see Fig. 3.7(a)). This behavior is discussed in detail shortly.

Energy scans of the $\boldsymbol{\tau}_1$ magnetic peaks were taken through the L_{III} absorption edge to observe the resonant enhancement and to confirm the magnetic nature of these satellites. These scans of the $(0\ 0\ 8)^+$ (superscript '+' denotes a $\boldsymbol{\tau}_1$ satellite) magnetic satellite and the (0 0 4) charge Bragg peak are shown in Fig. 3.4(a) and (b), respectively. The inflection point of the fluorescence yield (shown in Fig. 3.4(c)) was used to define the absorption edge ($\mathrm{E}_{\mathrm{L}_{III}}$). A large resonant enhancement of the intensity (a factor of ≈ 55 relative to the intensity at 25 eV below the edge) was seen a few eV above the edge, which is the signature of electric dipole (E1) resonance involving electronic transitions, $2p_{\frac{3}{2}} \leftrightarrow 5d$. Similar resonant enhancement was also observed (a factor of ≈ 26 in this case) in the vicinity of the L_{II}-edge. Due to the larger enhancement at the L_{III}-edge, however, XRES measurements described below were taken at the resonant energy (dashed line at $\mathrm{E}_{\mathrm{res.}}$ in Fig. 3.4 (a)) above this edge. Polarization analysis of magnetic scattering was not performed.

Longitudinal scans of the $(0\ 0\ 10)^+$ magnetic satellite at selected temperatures are

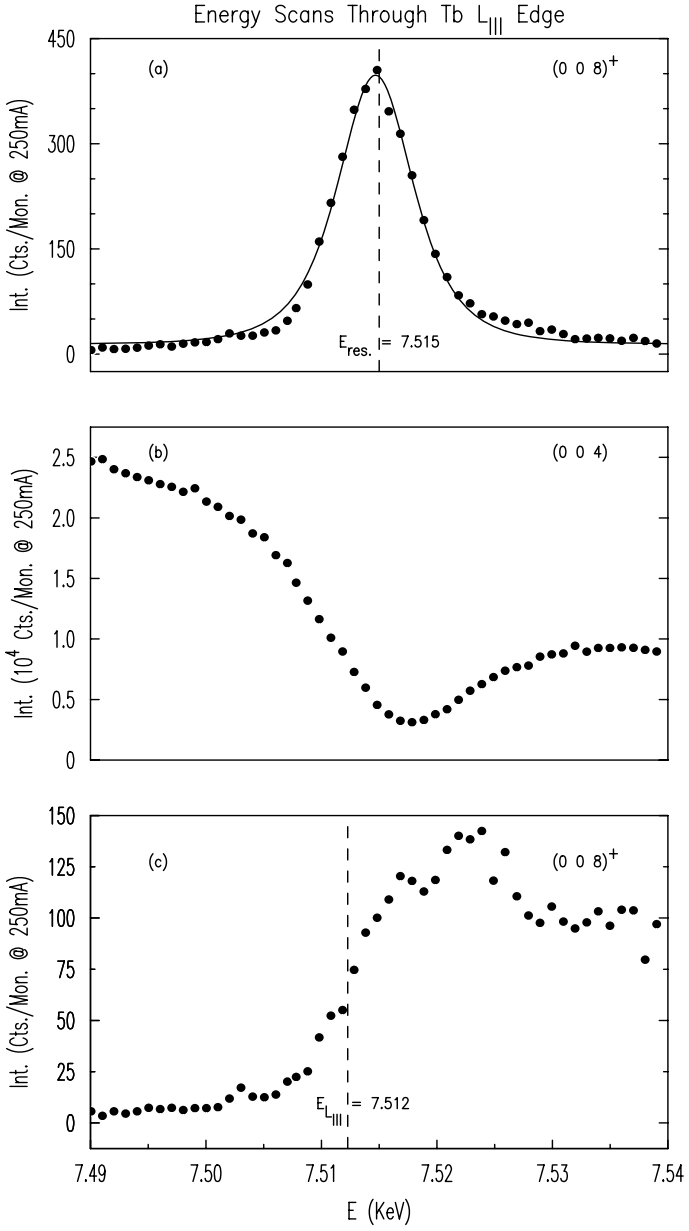

Figure 3.4 Energy scans through the L_{III}-edge of Tb at $T = 3.7$ K. (a) (0 0 $8)^+$ magnetic satellite peak, (b) (0 0 4) charge Bragg peak, and (c) fluorescence yields used to define the absorption edge. Solid line in (a) is a Lorentzian-squared fit used to obtain the resonant energy.

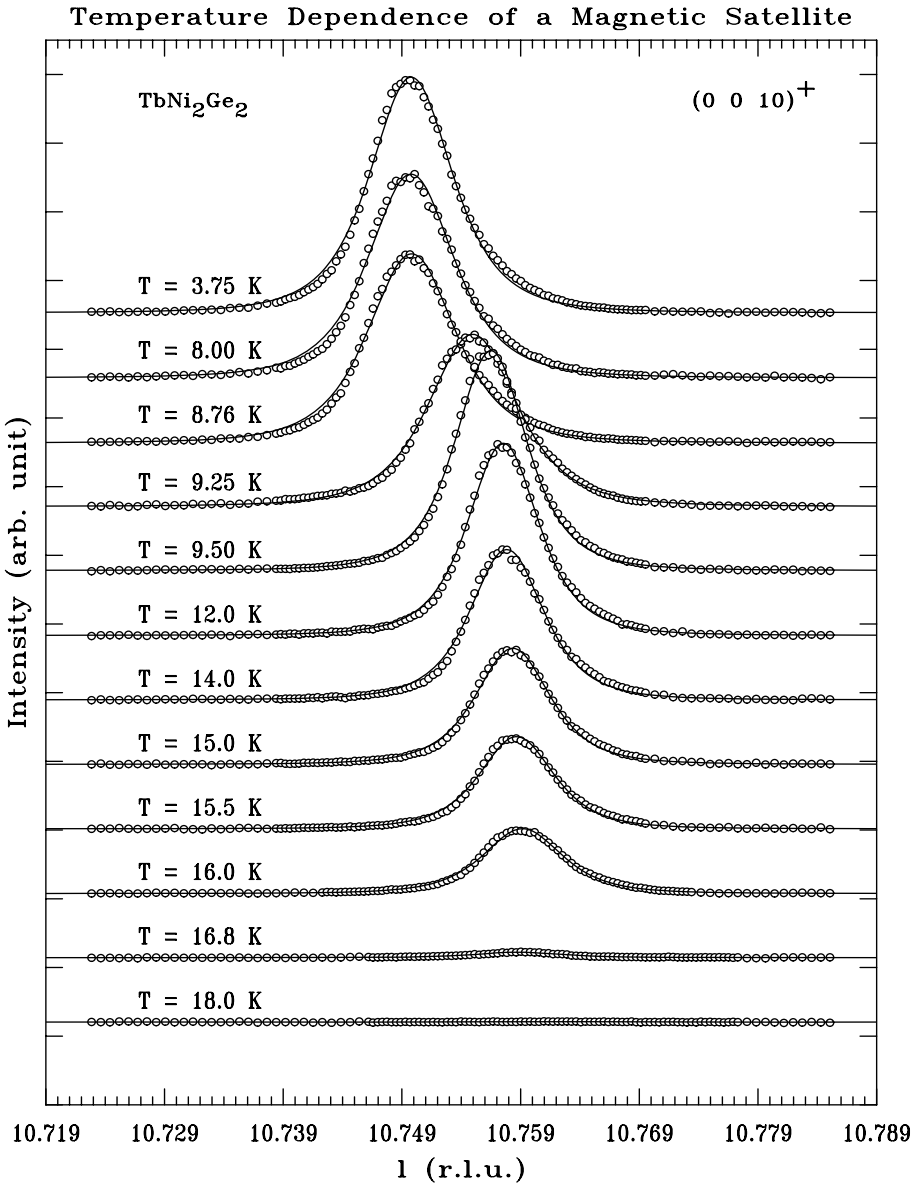

Figure 3.5 Longitudinal scans of the $(0\ 0\ 10)^+$ magnetic satellite peak at selected temperatures. Note the shift of the peak position to higher Q as the temperature is raised above T_t. Solid lines are fits to Lorentzian-squared line profiles used to extract I_{Max}s, HWHMs and peak positions. 1 r.l.u. = 0.6424 $Å^{-1}$.

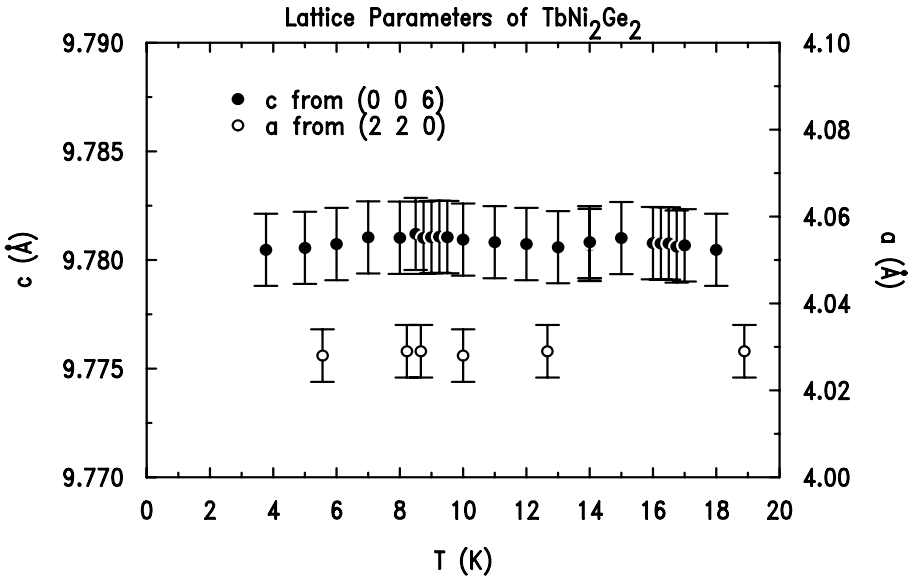

Figure 3.6 Temperature dependence of the c lattice parameter as obtained from the (0 0 6) charge Bragg reflection in XRES measurements. Also shown is the lattice parameter a obtained from (2 2 0) reflection in neutron diffraction measurements on a single crystal.

shown in Fig. 3.5. The most notable feature in these measurements is the shift of the peak position to higher Q value as the temperature increases, suggesting a change in the modulation vector. Since the lattice parameter c does not change appreciably with temperature (see Fig. 3.6) this shift reflects a change in $\boldsymbol{\tau}_1$.

The Bragg peak intensities (I_{Max}), widths (half-width at half-maximum, HWHM) and the modulation vectors obtained as a function of temperature are shown in Fig. 3.7. The main result of the XRES measurements is the temperature dependence of the $\boldsymbol{\tau}_1$ = (0 0 τ_z) propagation vector (Fig. 3.7(a)). Below T_t, it remains locked at (0 0 $\frac{3}{4}$) as was found in neutron measurement. However, above T_t it changes to (0 0 0.758$\pm$0.002), within a temperature inteval of 0.25 K. The neutron diffraction measurements were not able to resolve this steplike feature. In the temperature range $T_t < T < T_N$, the modulation vector $\boldsymbol{\tau}_1$ remains nearly constant within the error bars making it difficult to say whether the structure is *higher order commensurate* or *incommensurate*.

As shown in Fig. 3.7(b) and (c), both I_{Max} and HWHM show a discontinuity at the second phase transition from which T_t is found to be 9.3±0.2 K. It is surprising, however, that the magnetic peak broadens, corresponding to a reduced correlation length, at the transition to a commensurate phase. The measured longitudinal linewidth of the (0 0 6) charge peak is ±0.0038 r.l.u. and is indicated by the dotted-dashed line in Fig. 3.7(c) for comparison. The rocking curve width of the $(0\ 0\ 8)^-$ satellite (not shown) was found to be equal to the sample mosaic at (0 0 6), both of which are independent of temperature. One can compare the magnetic correlation lengths of the ordered phases by assuming that they are given simply by the inverse of the peak width (HWHM) in $Å^{-1}$, corrected for the instrumental resolution. Since the instrumental q-resolution was not measured it was assumed to be the same as the charge peak linewidth. At 3.7 K, in the commensurate phase, the magnetic correlation length is then 600 Å, whereas at 9.75 K, in the higher-temperature phase, it is on the order of 1200 Å.

The integrated intensity (I) of the $(0\ 0\ 10)^+$ satellite peak is shown in Fig. 3.7(d) as a function of temperature, complementing similar measurements by neutron diffraction. The Néel temperature (T_N), determined by modeling the temperature dependence with a Brillouin function ($B_{J=6}(\mid T - T_N \mid)$), is 16.8 ± 0.2 K. As was true for the order parameters measured by neutrons, there is a break in slope at T_t and the intensity is significantly enhanced at low temperature.

The direction of the ordered Tb moments were also determined by XRES from the **Q**-dependence of the integrated intensities of a series of magnetic satellites. As was mentioned earlier, at the resonance, x-ray scattering probes primarily the element selected. Thus, one can determine directly the moment direction of the Tb sublattice irrespective of any induced moments at the Ni sites. Fig. 3.8 shows the **Q**-dependence measured in three different scattering geometries at 3.7 K along with model calculations. The cross-section and the geometric factors have been given in the previous chapter. The only adjustible parameter in the calculations is an arbitrary scale factor which is the

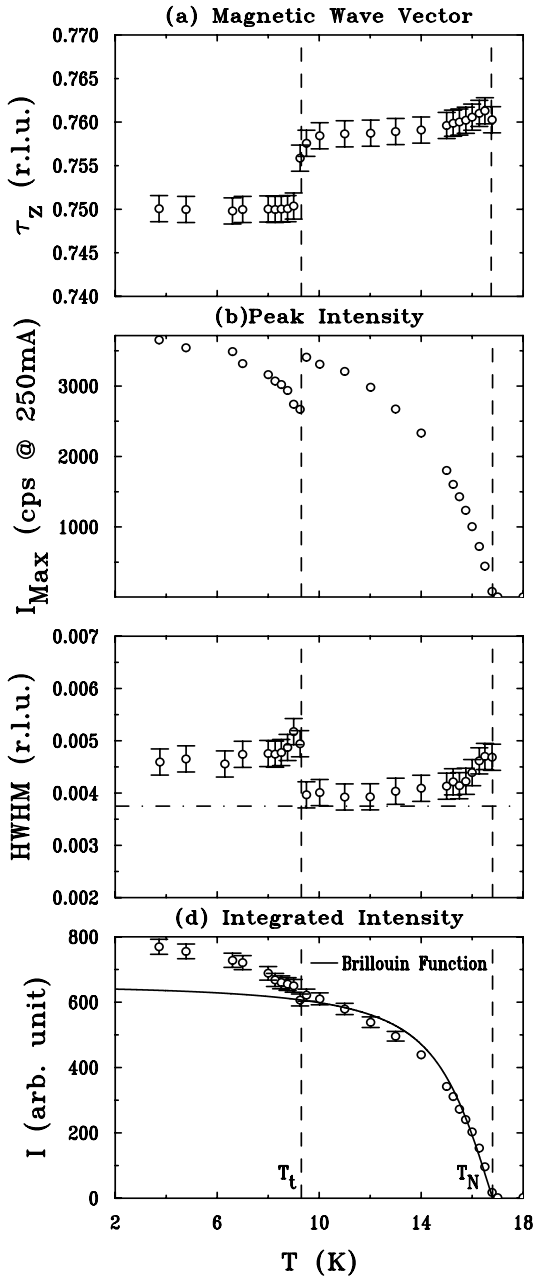

Figure 3.7 Temperature dependence of (a) the modulation vector, $\boldsymbol{\tau}_1 = (0\ 0\ \tau_z)$, (b) Bragg peak intensity, I_{Max}, (c) width, HWHM, and (d) the order parameter, I. The horizontal dotted-dashed line in (c) shows the position of the assumed instrumental q-resolution. Data were collected on raising the temperature.

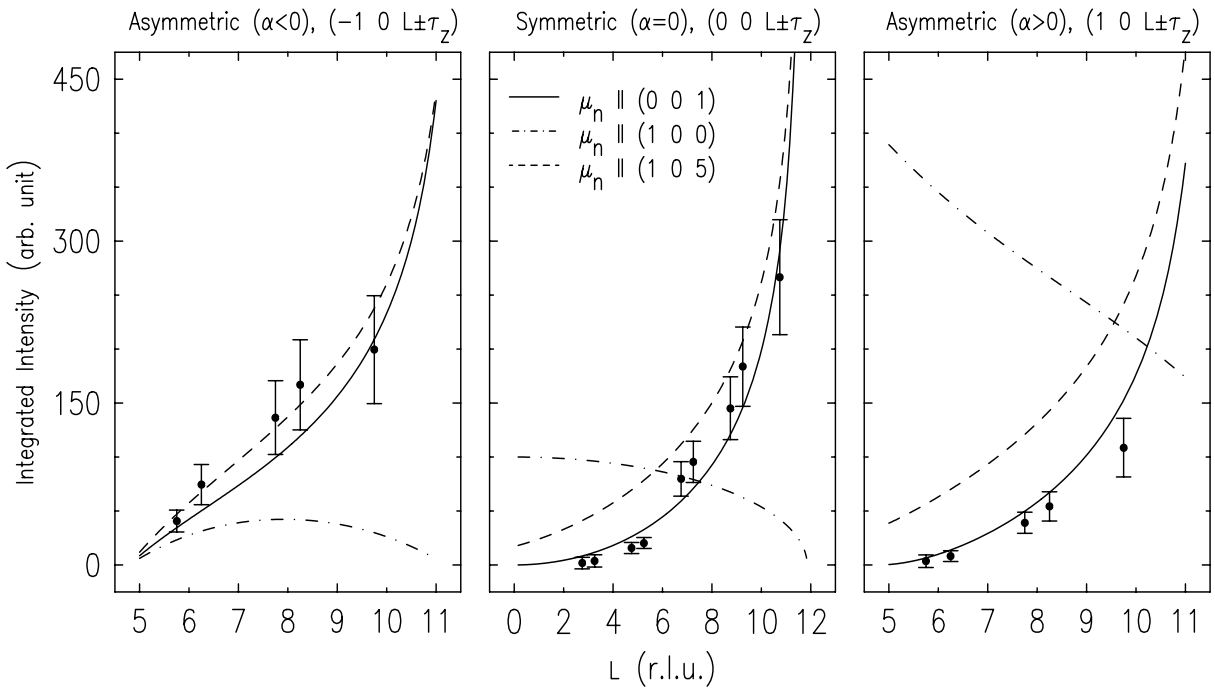

Figure 3.8 **Q**-dependence of the integrated intensities of magnetic Bragg peaks of the form $(h\ 0\ l)^{\pm}$ at 3.7 K. Measured intensities are shown in filled circles. Solid line is for a model with Tb moments $\parallel \hat{\mathbf{c}}$ axis ($\beta = 0$), dotted-dashed line is for moments $\perp \hat{\mathbf{c}}$ axis ($\beta = 90°$) and the dashed line is for $\beta = 20°$. All the scattering geometries are shown in Fig. 2.2.

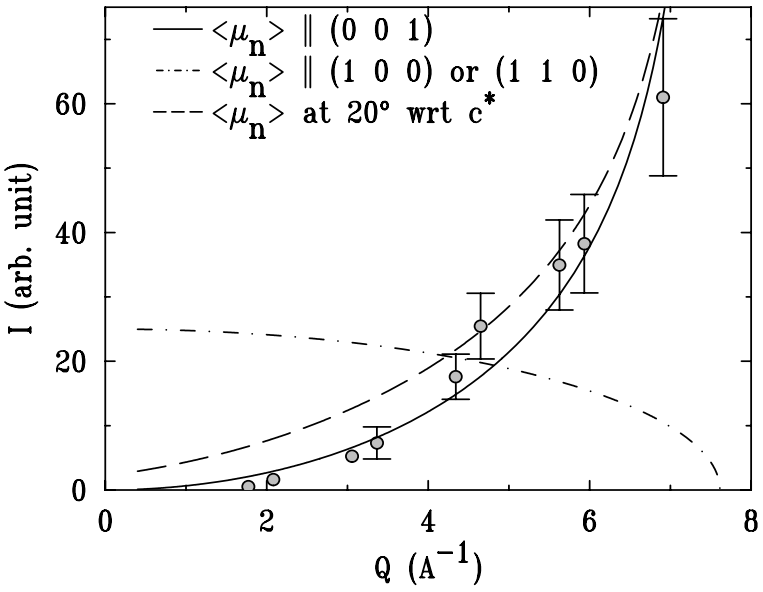

Figure 3.9 **Q**-dependence of the integrated intensities of magnetic Bragg peaks of the form $(0\ 0\ l)^{\pm}$ at 12 K.

same for all three geometries. As shown in Figs. 3.8 a model with the Tb moments in the basal plane results in a **Q**-dependence manifestly in disagreement with the data, while for moments along the $\hat{\mathbf{c}}$ axis the **Q**-dependence can be modeled quite well. Model calculations with a tilt angle $\beta \sim 20^{\circ}$ with respect to the $\hat{\mathbf{c}}$ axis are also shown. If considered alone, symmetric geometry will give a large error in β. However, this model does not agree well with the data in the $\alpha > 0$ geometry. As β is made smaller the agreement improves and all the dashed lines collapse on the solid lines. Thus, by using all three geometries simultaneously it was possible to measure the moment direction with 5° accuracy. Similar measurements in the symmeteric geometry were performed at 12 K above T_t. The **Q**-dependence as displayed in Fig. 3.9 clearly shows that in this phase too the moments are along the $\hat{\mathbf{c}}$ axis.

In summary, the principal finding of the XRES experiment is the temperature dependence of $\boldsymbol{\tau}_1$, which moves to $\approx (0\ 0\ 0.758)$ at T_t, and remains nearly constant above this transition. This shows that the structure above T_t has a long period and may be

incommensurate. Below T_t, $\boldsymbol{\tau}_1$ is locked at $(0\ 0\ \frac{3}{4})$. Also, a surprising broadening of the magnetic peak was also observed, corresponding to a reduced magnetic coherence length, at the phase transition from the higher temperature phase to the commensurate structure. In addition, this technique was used to confirm the uniaxial ordering of the Tb sublattice with the moments parallel to the $\hat{\mathbf{c}}$ axis in both the ordered phases in agreement with the neutron diffraction measurements.

Measuring the Absolute Values of the Moments: Neutron Diffraction on Powder Samples

With the propagation vectors and the moment direction known from neutron, XRES and magnetization measurements on single-crystal samples, powder neutron diffraction data were used to determine accurately the value of the ordered moments in order to eliminate uncertainties from single-crystal samples related to crystal shape and extinction effects. The procedure used and the assumptions made for the powder pattern calculations have been explained in the previous chapter.

Polycrystalline samples for neutron diffraction measurements were synthesized by arc-melting the stoichiometric mixture of the respective elements in an argon atmosphere and were subsequently annealed. The phase purity of the sample was verified by an x-ray powder diffraction pattern. The susceptibility measured on this powder showed the Néel transition at the expected temperature, ensuring that the magnetic ordering was not destroyed by strain during the grinding process, although the transition at T_t was not clearly discernible. Neutron diffraction measurements on this sample were performed at the high-resolution neutron powder diffractometer (HRNPD) located at the HFBR. Neutrons with wavelength of 1.8857 Å were used. The sample was sealed in a cylindrical vanadium container of diameter 0.9 cm and cooled inside a pumped He cryostat. Diffraction patterns were collected at several temperatures over the angular range 0°-155° in 2θ with a step size of 0.05° . The zero of 2θ is defined within ±0.05°.

The neutron diffraction patterns at three different temperatures for a selected range of angles are shown in Fig. 3.10. At 20 K, well above the transition temperature, only nuclear Bragg peaks corresponding to the body-centered tetragonal crystal structure were observed. Fig. 3.10(a) shows a few such low-angle nuclear peaks. A conventional unit cell was used to index these peaks with $a = 4.04$ Å and $c = 9.784$ Å, consistent with the lattice parameters determined from the single-crystal samples. In addition to sharp peaks, magnetic diffuse scattering is also seen in the low-angle region (see Appendix A).

The calculated pattern, based upon the published [22] structure for $TbNi_2Ge_2$ and the above lattice parameters, was found to be in very good agreement (see Appendix B) with the observed intensities, confirming the low-temperature structure to be of the $ThCr_2Si_2$ type. The scale factor thus found is used in the model calculations for the magnetic peaks in order to put them on an absolute scale with the nuclear peaks.

Above T_t, but below T_N, all of the magnetic peaks in the pattern (Fig. 3.10(b)) can be indexed using only $\boldsymbol{\tau}_1 = (0\ 0\ 0.758)$ modulation (see the Table in Appendix C). The small peak at the position of (0 0 2) is an artifact of the subtraction method, as are the "negative" peaks. As expected, the $\boldsymbol{\tau}_1$ satellites of (0 0 l) nuclear peaks are absent due to the fact that the moment direction is parallel to the $\hat{\mathbf{c}}$ axis in both magnetic phases. All of the superlattice peaks in the powder neutron diffraction pattern at 4 K can be indexed (Fig. 3.10(c) and column $(h\ k\ l)_{\mathrm{c}} \pm \boldsymbol{\tau}_{\mathrm{mag}}$ in Appendix D) using the wave vectors found in the measurements on single-crystal samples. This indicates that there are no additional modulations in this phase.

Below T_t, a magnetic unit cell of the commensurate structure can be constructed by doubling the chemical unit cell along the (1 1 0) direction, implied by $\boldsymbol{\tau}_2$, and stacking four such groups of unit cells along the (0 0 1) direction, implied by $\boldsymbol{\tau}_1$. All magnetic peaks can also be indexed with respect to this supercell. These indices are shown in the second column of the Table in (column $(h\ k\ l)_{\mathrm{m}}$) in Appendix D.

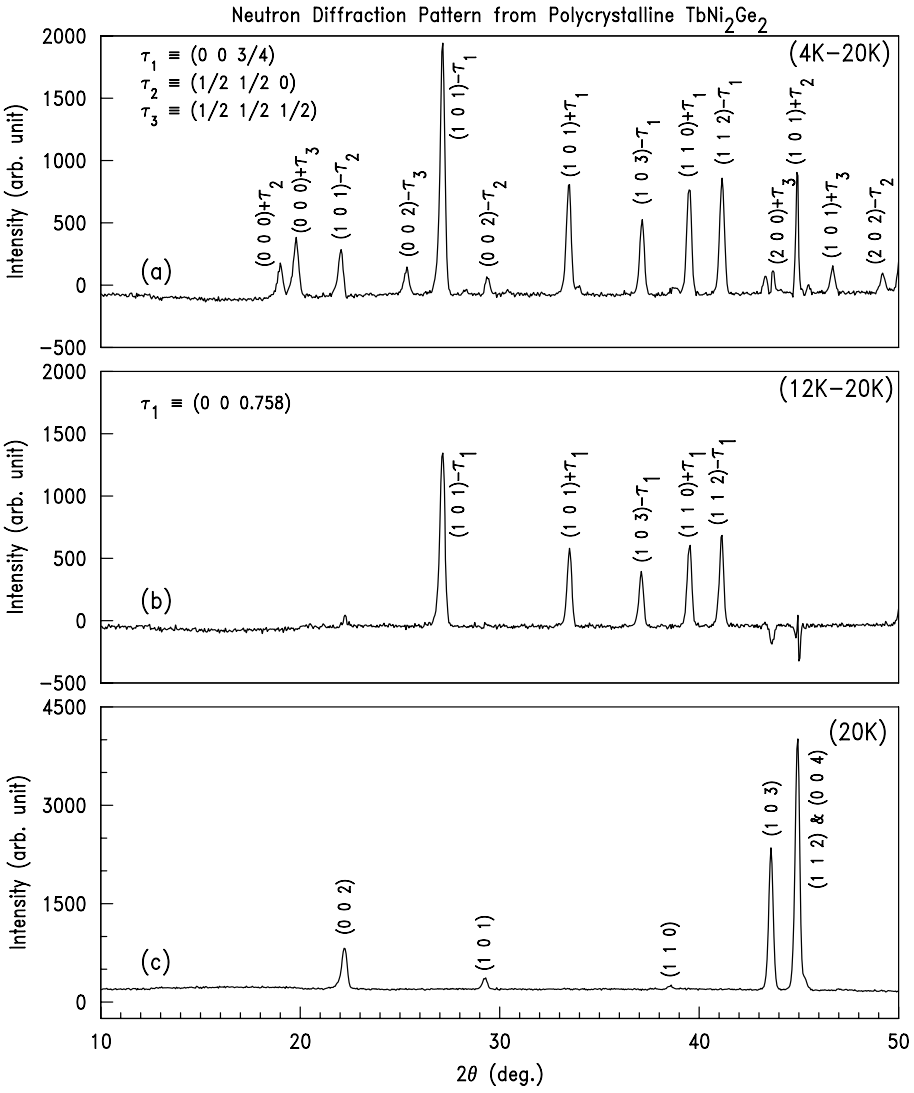

Figure 3.10 Neutron diffraction patterns from polycrystalline $TbNi_2Ge_2$ sample at (a) 4 K, (b) 12 K, and (c) 20 K, respectively. Diffraction pattern at 20 K was subtracted from those at 4 K and 12 K in order to identify the magnetic peaks. These are shown in (a) and (b). Indices of some of the weak peaks in (a) are not shown.

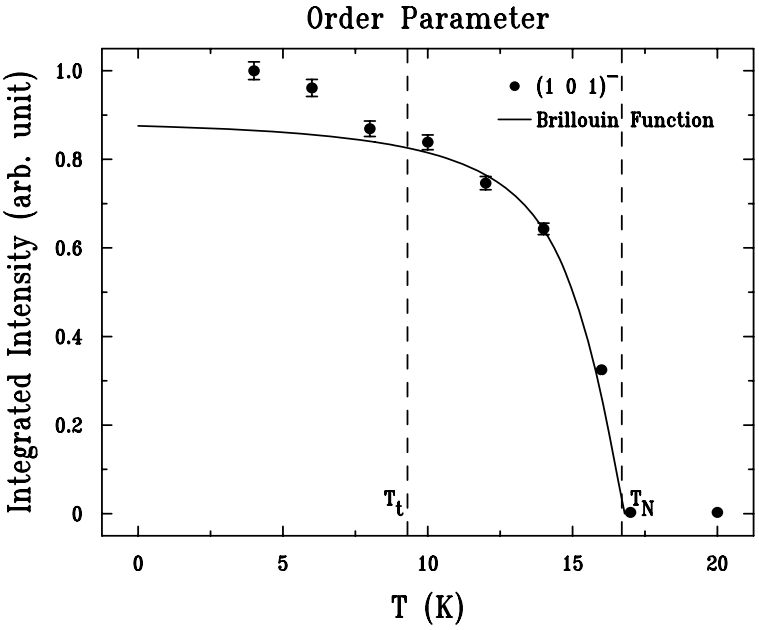

Figure 3.11 Temperature dependence of the integrated intensity of $(101)^-$ magnetic peak measured by powder neutron diffraction.

The temperature dependence of $(\frac{1}{2}\ \frac{1}{2}\ 0)$, $(\frac{1}{2}\ \frac{1}{2}\ \frac{1}{2})$, $(0\ 0\ 10)^+$ and peaks of the form $(1\ 1\ l)^\pm$ was measured on the single-crystal sample. In Fig. 3.11 the integrated intensity of the $(1\ 0\ 1)^-$ satellite peak, as measured on the powder sample, is plotted to obtain a unified picture. As was the case previously, the temperature dependence below T_N can also be modeled by a Brillouin function which yields a Néel temperature of 16.8±0.3 K. Although there is a large enhancement of the intensity below T_t, the break in slope at this transition is less discernible than in the former cases.

The superlattice peak associated with $\boldsymbol{\tau}_1$, as observed at $(0\ 0\ 10)^+$ (Fig. 3.7), $(1\ 1\ 0)^+$ (Fig. 3.2) and $(1\ 0\ 1)^-$ (Fig. 3.11), respectively, has a marked discontinuity of the slope at T_t and a large increase of the low temperature intensity relative to that above this transition. These can be explained as consequences of the Tb moments acquiring the full saturation value of 9.0 μ_B below T_t from an AM phase above this temperature. If the structure remained AM below T_t a smoothly varying order parameter would be expected.

Amplitude Modulated Phase ($T_t < T < T_N$)

In this model all the ordered moments in a given Tb plane (j) have the same magnitude and direction while they vary sinusoidally from plane to plane according to:

$$\langle \boldsymbol{\mu}_j \rangle = \mu_s \cos(2\pi \boldsymbol{\tau}_1 \cdot \mathbf{r}_j + \phi)\hat{\mathbf{c}}, \tag{3.1}$$

where $\boldsymbol{\tau}_1$=(0 0 z); μ_s is the saturation moment (9.0 μ_B) of Tb^{3+}; $\mathbf{r}_j$, the position of the j-th Tb ion, is in units of lattice parameter c; and ϕ is an arbitrary phase factor. For intensity calculations $\boldsymbol{\tau}_1$ was approximated by (0 0 $\frac{25}{33}$) and ϕ=0 was used. Zero magnetic moment was assumed for the Ni atoms. The calculated intensities (I_{Cal}) for this model agree quite well with the observed ones (I_{Obs}) (see the Table in Appendix C). For comparison, some of the calculated intensities for an AM model with $\boldsymbol{\tau}_1$=(0 0 $\frac{3}{4}$) which is the model proposed in a previous experiment [39] have also been listed (column headed $I_{(00\frac{3}{4})}$). Although the agreement between this model and the powder pattern is as good as in the long-period model's case the modulation vector is not correct, as known from the XRES measurements.

Equal Moment Commensurate Phase ($T < T_t$)

The model for the low temperature ordered phase is shown in Fig. 3.12. As in the AM phase, zero magnetic moment was assumed for the Ni atoms. As can be seen, while the ferromagnetic planes account for $\boldsymbol{\tau}_1$ and $\boldsymbol{\tau}_1'$, the antiferromagnetic planes give rise to $\boldsymbol{\tau}_2$ and $\boldsymbol{\tau}_3$ superlattice peaks. The calculated intensities (I_{Cal}) according to this model agree very well with the observations (see Appendix D). The value for the Tb ordered moment was found to be 9.0±0.2 μ_B, which is the expected saturation value of the Hund's rule ground state ($^7F_6$) of Tb^{3+}.

Next, the possibility of induced moment ($\leq \frac{1}{2}$ μ_B) at the Ni sites was considered. A ferromagnetic coupling to the nearest Tb neighbor was assumed. In this scheme induced moments can exist only on the Ni sites between planes such as #2 and #3 in Fig.

3.12. At all other Ni planes the exchange field vanishes by symmetry. The calculated intensities, however, were insensitive to the value of induced moment up to 0.3 μ_B and produced equally good 'fits'. Above this value they disagreed with the observed ones. Thus, an upper bound of 0.3 μ_B for an induced moment at the Ni site was obtained.

Discussion

The zero-field magnetic structures of $TbNi_2Ge_2$ have been determined using neutron diffraction and XRES measurements. In the low-temperature ($T < T_t$) phase, propagation vectors $\boldsymbol{\tau}_1$=(0 0 $\frac{3}{4}$) (along with the third harmonic $\boldsymbol{\tau}'_1$=(0 0 $\frac{1}{4}$)), $\boldsymbol{\tau}_2$=($\frac{1}{2}$ $\frac{1}{2}$ 0) and $\boldsymbol{\tau}_3$=($\frac{1}{2}$ $\frac{1}{2}$ $\frac{1}{2}$) were identified by neutron diffraction on a single crystal. The subtle change of the wave vector $\boldsymbol{\tau}_1$ to (0 0 0.758) at T_t which was not detected in the earlier work [39] was resolved using the high **Q**-resolution of XRES. Above T_t, it was difficult to determine whether the structure was higher order commensurate or incommensurate. According to the models proposed in this work, the phase transition at T_t is from an EM *commensurate* phase ($T < T_t$) (Fig. 3.12) to an AM *long period* AF structure ($T_t <$ T $< T_N$). From powder neutron diffraction measurements, the magnitude of the Tb ordered moments in the EM phase was found to be 9.0 $\pm$0.2 μ_B. In the earlier work [39] the low temperature phase was found to be AM. In both the phases the ordered moments of Tb were found to be parallel to the $\hat{\mathbf{c}}$ axis. In addition, an upper bound of 0.3 μ_B for any induced moments at Ni sites has been found.

The low temperature EM phase is an antiphase domain structure consisting of triplets of antiferromagnetically coupled ferromagnetic Tb planes (#0-2 and #4-6 in Fig. 3.12) separated by planes ordered antiferromagnetically (#3 and #7). The formation of triplets can be explained by a ferromagnetic coupling within the plane and two dominant interplanar coupling constants, nearest-neighbor antiferromagnetic and next-nearest-neighbor ferromagnetic interactions. Since the modulation vector is (0 0 $\frac{3}{4}$) two such neighboring triplets have opposite phase. Due to the antiferromagnetic coupling

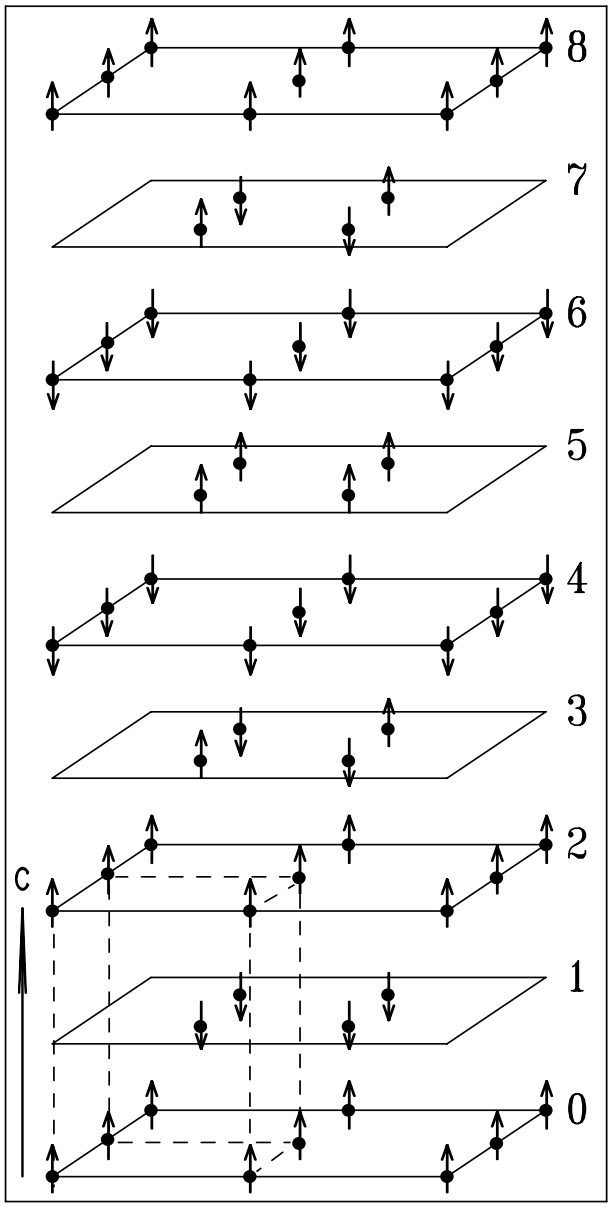

Figure 3.12 The magnetic structure of $TbNi_2Ge_2$ at 4 K. One magnetic unit cell is shown. The dashed lines indicate a conventional unit cell. $\uparrow(\downarrow)$ represents the magnetic moment of a Tb atom (depicted by solid circles) 'up'('down') along the $\hat{\mathbf{c}}$ axis. Ni and Ge atoms are not shown. Planes are numbered for reference.

between the nearest-neighbor planes, the moments on planes such as #3 and #7 are 'frustrated', which can lead to antiferromagnetic ordering in these planes. In the pure AM phase above T_t this frustration is absent. Due to the presence of this 'frustration' in the EM phase it is conceivable that the magnetic structure could break up into smaller domains compared to the domain sizes in the AM phase. This reduces the magnetic coherence length below T_t and can give rise to the magnetic peak broadening as was observed (Fig. 3.7(c)) in XRES measurements.

Although the mechanism driving the lock-in transition at T_t is not clear, it is interesting to consider a simple phenomenological model first introduced by Elliot [31] (see also Kaplan [74]) which seems to account for the observed magnetic behavior of $TbNi_2Ge_2$. In his mean field theory of an Ising model with a ferromagnetic in-plane coupling and interactions only between nearest and next-nearest neighbor planes, he shows that an AM structure is stable at finite temperature below the highest ordering temperature (T_N). This is because the free energy ($F = U$ - TS) is lower due to higher entropy of the sinusoidal arrangement relative to that of an EM phase. As the temperature is lowered the entropic term decreases[2] and the stable structure is that which minimizes the internal energy, U. As a consequence, in this model, the modulated structure squares up and possibly changes into an antiphase domain structure at a temperature slightly above $\frac{1}{2}T_N$ where the moment saturates [31, 75]. This general behavior is observed in both $TbNi_2Ge_2$ and $TbNi_2Si_2$ where the AM to an EM phase transition takes place at $T_t \sim 0.55T_N$ and $T_t \sim 0.6T_N$, respectively.

Finally, it is pointed out that since Tb^{3+} is a non-Kramers ion it can have a singlet ground state due to the CEF splitting of its degenerate $J = 6$ multiplet. On the other hand, in order to form a large moment at low temperatures the presence of at least one low-lying CEF level at an energy comparable to the exchange energy above the ground state is also necessary [32, 33]. These two levels can mix to form a 'compound' ground

[2]This is also to be expected on general grounds from Nernst's theorem.

state by the exchange interaction which varies in space according to the propagation vector. Since in the case of $TbNi_2Ge_2$ the moments saturate in the EM phase, the low-lying CEF eigenstates must also have a large $|J_z = \pm 6\rangle$ component where the axis of quantization, $\hat{\mathbf{z}}$, is along the direction ($\hat{\mathbf{c}}$ axis) of the ordered moments. Although CEF levels for $TbNi_2Ge_2$ are not known, for the isostructural $TbNi_2Si_2$ the ground state is a Γ_4^+ singlet with a Γ_3^+ singlet as the first excited state [76]. This excited state is only 6.6 K above the ground state and together they form a 'pseudo-doublet.' The measured entropy above T_N is $R\ln(2.4)$ which is consistent with this [76]. Other CEF levels are 38 K above the ground state. As was shown in Ref. [76], $|J_z = \pm\ 6\rangle$ predominates in both the low-lying singlets. The overall CEF splitting relative to the free ion degenerate J-multiplet is $\Delta \approx \pm 50$ K which is comparable to ≈ 40 K estimated from the susceptibility data [23] for $TbNi_2Ge_2$. Based on these similarities, a CEF level scheme such as that in $TbNi_2Si_2$ seems probable for $TbNi_2Ge_2$. Such CEF level scheme is likely to play an important role in various metamagnetic phases at low temperature mentioned earlier. One can then expect to find a series of intricate field-induced phases as the balance of exchange and CEF is varied by the external field. A likely possibility is the magnetization of the AF planes. One can also speculate that these AF 'domain walls' will be rearranged to give way to new periodicities as ferromagnetism is induced. Another possibility is the emergence of an AM structure from the low temperature EM phase, as was reported to occur in $TbNi_2Si_2$ crystal [26]. The neutron diffraction studies of the metamagnetic structures are presented in Chap. 6.

$DyNi_2Ge_2$

Previous Investigations of Magnetic Structures

The magnetic properties of this material have been studied by various groups. The ordering temperature of 11 K reported by earlier groups [3] is considerably different than

those found by André and co-workers who have carried out a detailed study on polycrystalline $DyNi_2Ge_2$ samples [40]. They observed a paramagnetic to an antiferromagnetic phase transition at $T_N = 7.5$ K in their susceptibility measurement. According to their powder neutron diffraction measurements, this transition takes place at 8.5 K. Using neutron diffraction methods on a powder sample they found the ordered phase, at 1.4 K, to be an incommensurate AM structure with propagation vector (0 0 0.788). Further, they found that the ordered Dy moments form an angle of 20° with the $\hat{\mathbf{c}}$ axis. As shown below the transition temperatures and the propagation vectors are significantly different in high-quality single crystals.

Susceptibility and Magnetization

The temperature dependence of the low field susceptibility with applied field parallel ($\mathbf{H} \parallel \hat{\mathbf{c}}$) and perpendicular ($\mathbf{H} \perp \hat{\mathbf{c}}$) to the $\hat{\mathbf{c}}$ axis was found to be anisotropic in the paramagnetic phase. From cusps in the susceptibility two transitions were identified, and are indicated in Fig. 3.13(a). The paramagnetic-to-antiferromagnetic transition occurs at $T_N = 8.2$ K. The second transition is at a lower temperature, $T_t = 3.2$ K [45, 23]. This is in contrast to a previous susceptibility measurement [40] where only one transition, at $T_N = 7.5$ K, was observed. This may be a consequence of polycrystalline averaging which often makes the lower transition less pronounced, as was found to happen in $GdNi_2B_2C$ (see Ref. [35]). In this material a second transition at 14 K (T_N=20 K) due to the Gd spin reorientation was observed using XRES [67]. Such subtle transitions are particularly difficult to detect in a polycrystalline sample.

The magnetization as a function of field applied along the $\hat{\mathbf{c}}$ axis at 2 K (Fig. 3.13(b)) shows two metamagnetic transitions at 18 kG and 27 kG, respectively. It is likely that on further lowering of the temperature, these transitions would become sharper (similar to data in Ref. [44]), with the appearance of at least one more transition approximately at 9 kG, which is barely discernible at this temperature. Also, since the moment does

not acquire the full saturation value of 10 μ_B up to 55 kG, it is conceivable that there may be one or more metamagnetic transitions in higher fields. When the field is in the basal plane, however, the magnetization does not manifest any transitions.

This magnetic behavior is very similar to that of the isostructural $DyNi_2Si_2$ compound which has two magnetic phase transitions, at 3.4 K and 6 K, respectively [27, 28, 29]. As in $DyNi_2Ge_2$, the anisotropy is not very strong. At 1.5 K, there are four metamagnetic transitions with field applied along the $\hat{\mathbf{c}}$ axis [27]. This behavior was found to be qualitatively like that of $TbNi_2Si_2$ [25]. The zero-field magnetic structures in these two materials were found also to be quite similar [28, 26].

Interestingly, the magnetic behavior of $DyNi_2Ge_2$ is also qualitatively similar to that of the neighboring member of the series, $TbNi_2Ge_2$, which exhibits two magnetic transitions [23, 44], at $T_N = 16.8$ K and $T_t = 9.3$ K, respectively, in zero field as was discussed in the previous section. The magnetization measurements on this material at 2 K with the field parallel to the $\hat{\mathbf{c}}$ axis shows a sequence of five metamagnetic transitions below 55 kG. Both the susceptibility and magnetization showed strong anisotropy with the $\hat{\mathbf{c}}$ axis as the easy axis of magnetization. Neutron and XRES measurements showed indeed the ordered moments are aligned with the $\hat{\mathbf{c}}$ axis. In the case of $DyNi_2Ge_2$ the anisotropy is not as strong as in $TbNi_2Ge_2$. This implies that there may be ordered component of Dy moments in the basal plane. Also, as mentioned above, the metamagnetic phase transitions in $DyNi_2Ge_2$ may become sharper as the temperature is lowered below 2 K, making this material another system for the study of metamagnetism.

Neutron Diffraction Measurements

The neutron scattering measurements on a single crystal of $DyNi_2Ge_2$ were carried out at the H4M spectrometer of High Flux Beam Reactor (HFBR) at Brookhaven National Laboratory. Neutrons with energies of 14.7 meV were used with collimator settings of 40′-40′-80′-none. Pyrolytic graphite filters were used to eliminate second harmonic

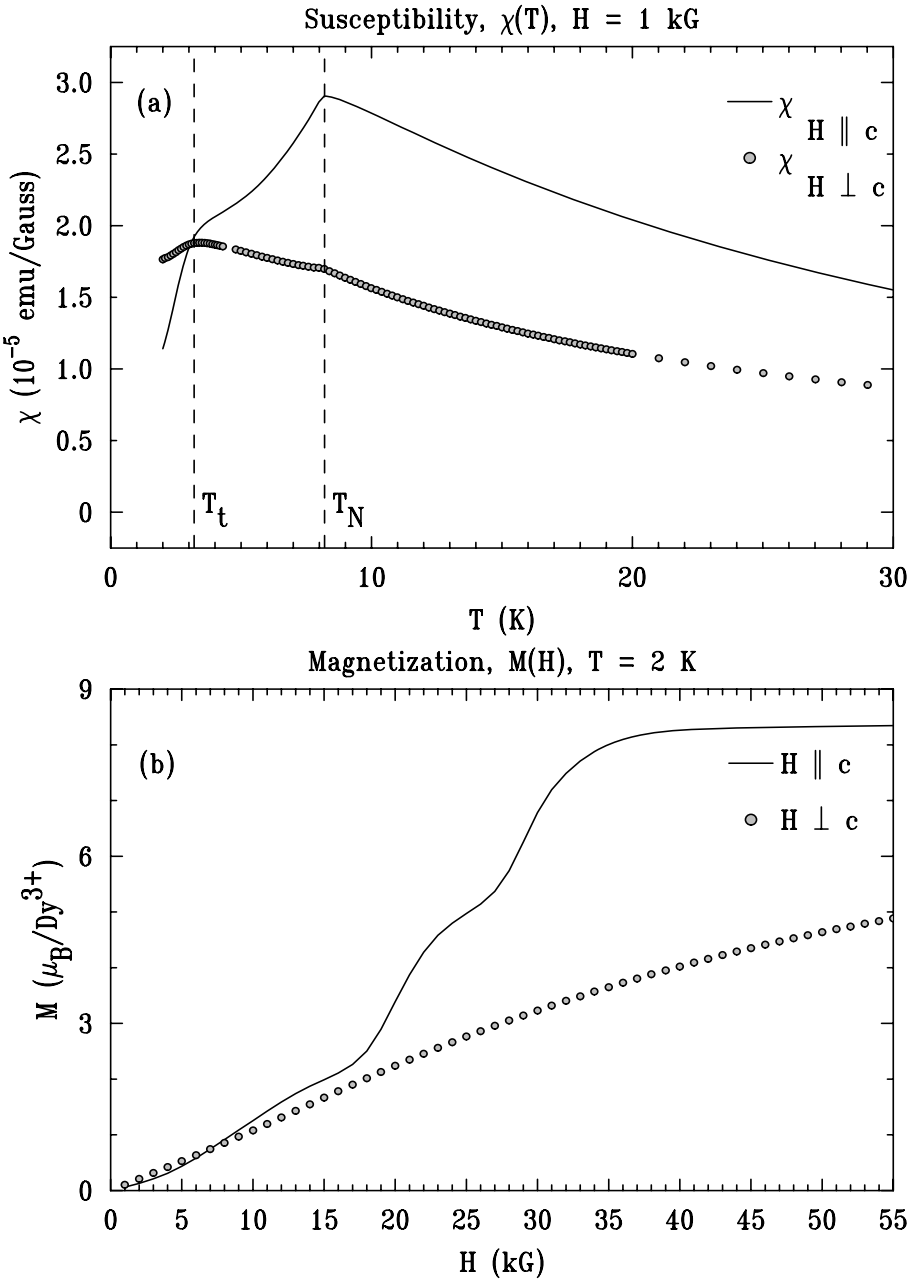

Figure 3.13 (a) Susceptibility and (b) magnetization of $DyNi_2Ge_2$ single crystal. The dashed vertical lines in (a) indicate the positions of the transition temperatures, T_N and T_t, respectively.

($\frac{\lambda}{2}$) contamination of the beam. No special preparation of the sample was necessary. The largest crystal of the same batch used for the magnetization measurements was chosen. The sample was closely a square plate with dimensions of 7 mm×7 mm×1.5 mm, weighing about 300 mg.

For the neutron diffraction measurements, a single crystal of $DyNi_2Ge_2$ was aligned in the $[h\ h\ l]$ zone. At 11 K, well above T_N determined from the susceptibility data, scans along various symmetry directions in this zone showed only nuclear peaks consistent with the body-centered tetragonal crystal structure (*i.e.* $h+k+l = 2n$ where n is an integer) with lattice parameters $a = 4.031\pm0.003$ Å and $c = 9.776\pm0.004$ Å at this temperature. No significant variations of the lattice parameters with temperature were observed. Below T_N, magnetic satellite peaks corresponding to $\boldsymbol{\tau}_1 = (0\ 0\ \frac{3}{4})$ developed. The presence of weak magnetic satellites of $(0\ 0\ l)$ associated with $\boldsymbol{\tau}_1$ indicated that there is a small component of the ordered moments in the basal plane perpendicular to the $\hat{\mathbf{c}}$ axis.

At 1.5 K, below the second transition at T_t, additional superlattice peaks associated with $\boldsymbol{\tau}_2 = (\frac{1}{2}\ \frac{1}{2}\ 0)$ and $\boldsymbol{\tau}_3 = (\frac{1}{2}\ \frac{1}{2}\ \frac{1}{2})$ emerged (see Fig. 3.14(a)). A third harmonic, $\boldsymbol{\tau}_1'$ $= (0\ 0\ \frac{1}{4})$, related to $\boldsymbol{\tau}_1$ also developed, indicating a squaring up of the structure. No other modulations in this zone were found. Again, the presence of relatively weak $\boldsymbol{\tau}_1$ satellites of $(0\ 0\ l)$ nuclear peaks implies a small component of the ordered moments in the basal plane. The magnetic unit cell of this structure consists of 16 chemical unit cells, as implied by the simultaneous existence of $\boldsymbol{\tau}_1$ and $\boldsymbol{\tau}_2$.

The integrated intensities of various magnetic Bragg peaks corresponding to (1 1 2)-$\boldsymbol{\tau}_1$, (1 1 2)-$\boldsymbol{\tau}_1'$, (1 1 2)+$\boldsymbol{\tau}_2$ and (2 2 2)-$\boldsymbol{\tau}_3$ are shown in Fig. 3.15 as a function of temperature. The intensity of the $\boldsymbol{\tau}_1$ satellite increases continuously from zero at T_N and has a small break at the lower phase transition at T_t. Below this temperature, magnetic peaks corresponding to $\boldsymbol{\tau}_2$ and $\boldsymbol{\tau}_3$ appear. Both $\boldsymbol{\tau}_2$ and $\boldsymbol{\tau}_3$ show very similar dependencies on temperature which suggests that these modulation vectors are related.

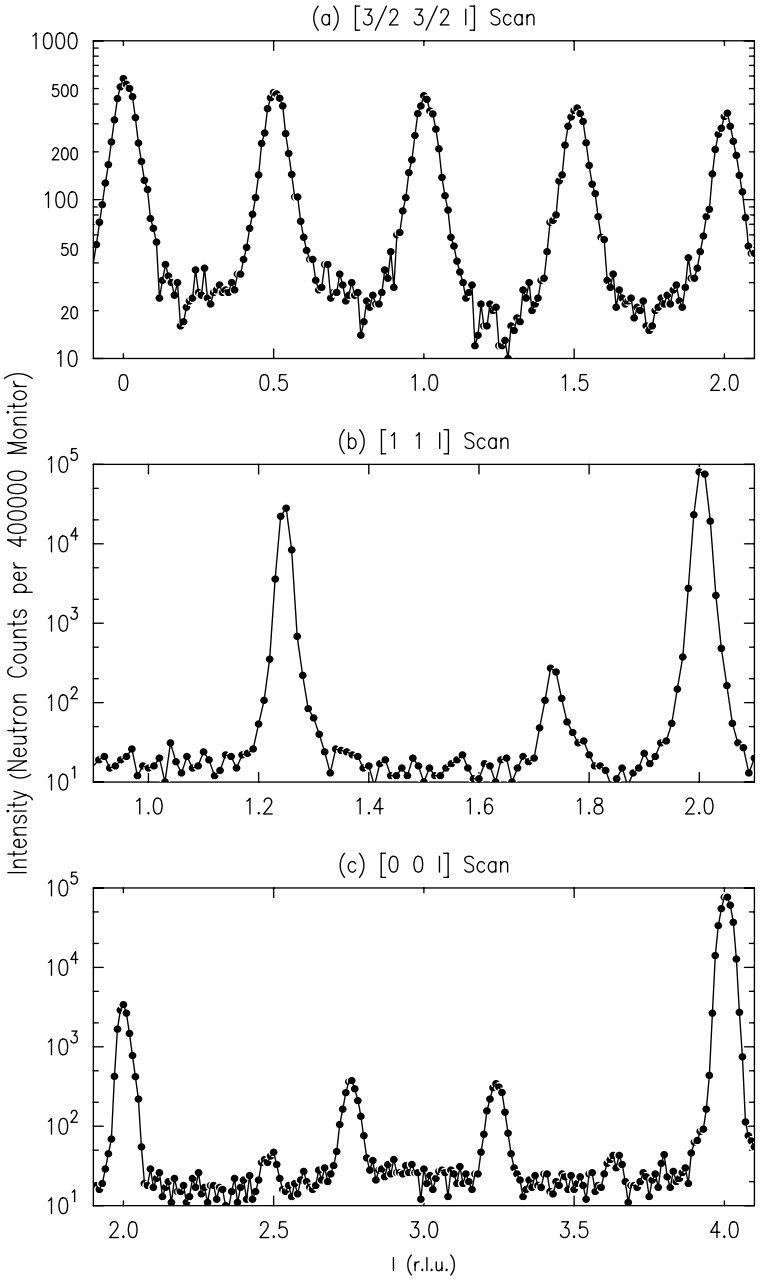

Figure 3.14 Selected reciprocal lattice scans at 1.5 K in the $[h\ h\ l]$ zone showing various magnetic peaks. (a) $[\frac{3}{2}\ \frac{3}{2}\ l]$ scan, (b) $[1\ 1\ l]$ scan and (c) $[0\ 0\ l]$ scan. The small peaks near 2.5 and 3.6 in (c) are from a second grain in the sample. The $\boldsymbol{\tau}_1'$ satellites in the $[0\ 0\ l]$ scan were too weak to be observed. Note that the intensities are shown on logarithmic scales.

The third harmonic becomes negligibly small above T_t indicating that the structure in this phase is essentially sinusoidal. As T_t is approached from above, the structure starts to square up giving rise to the harmonic.

The temperature dependence of these intensities can be modeled by Brillouin type functions, $B_J(\mid T - T_c \mid)$ where T_c is the transition temperature, shown by the solid lines in Fig. 3.15. In the case of $\boldsymbol{\tau}_1$, $J = \frac{15}{2}$ was used, whereas for $\boldsymbol{\tau}_2$ and $\boldsymbol{\tau}_3$, $J = \frac{1}{2}$ was used. The transition temperatures thus obtained are $T_N = 8.3 \pm 0.1$ K and $T_t = 3.1 \pm 0.2$ K, in close agreement with those determined by susceptibility measurements. The fact that, below T_t, the $\boldsymbol{\tau}_2$ and $\boldsymbol{\tau}_3$ order parameters can be modeled by $B_{J=\frac{1}{2}}$ suggests that the CEF ground state is a magnetic doublet. This is possible since Dy^{3+} is a Kramers ion. The CEF split $J = \frac{15}{2}$ multiplet of Dy^{3+} will always be at least doubly degenerate in the absence of an external magnetic field. In the case of $DyNi_2Si_2$ the magnetic entropy reaches $\sim R \ln(10.7)$ at 30 K which suggests that the CEF level scheme contains at least five doublets within 50 K [27]. Due to the isostructural relationship and similar magnetic behavior with this compound a similar set of CEF levels in $DyNi_2Ge_2$ seems feasible. In the temperature region below T_t only the low-lying CEF levels are important due to thermal depopulation of the higher excited levels. Since more CEF eigenstates are likely to be involved above T_t, the temperature dependence of $\boldsymbol{\tau}_1$ is different than those of $\boldsymbol{\tau}_2$ and $\boldsymbol{\tau}_3$ below T_t.

Also, in the case of the $\boldsymbol{\tau}_1$ superlattice peak below T_t, there is a small enhancement of the intensity above that expected from the Brillouin function behavior. This is due to the Dy ions acquiring their full saturation value of 10 μ_B upon going through the transition at T_t from an AM structure above this temperature. If the structure remained AM below T_t then the break as shown in Fig. 3.15 is not expected.

The magnetically ordered phases of $DyNi_2Ge_2$ are very similar to those found in the neighboring, isostructural, $TbNi_2Ge_2$ compound [44]. This material orders below 16.8 K (T_N) in a longitudinal AM structure with propagation vector $\boldsymbol{\tau}_1 \approx (0\ 0\ 0.758)$

whereas below 9.3 K (T_t) the structure becomes EM commensurate with the same set of modulation vectors ($\boldsymbol{\tau}_1$, $\boldsymbol{\tau}_1'$, $\boldsymbol{\tau}_2$, $\boldsymbol{\tau}_3$) as was found in $DyNi_2Ge_2$ below 3.2 K. The transition from the AM to an EM structure in $TbNi_2Ge_2$ was also evidenced by the break and increase in intensity, of the $\boldsymbol{\tau}_1$ satellite at T_t. Unlike the Tb compound, where the ordered moments in both the phases are along the $\hat{\mathbf{c}}$ axis, there is a component of Dy moment in the basal plane, consistent with the susceptibility and low temperature magnetization measurements.

Magnetic Structures and Discussion

Based on these results, and the isostructural relationship to $TbNi_2Ge_2$, a magnetic structure as shown in Fig. 3.16 for $DyNi_2Ge_2$ below $T_t = 3.1$ K seems feasible. In this EM phase all the Dy moments have their full saturation moment of 10 μ_B (consistent with the Hund's rule ground state, ${}^6H_{\frac{15}{2}}$) aligned at an angle β with respect to the $\hat{\mathbf{c}}$ axis. This structure consists of antiferromagnetically coupled, ferromagnetically ordered, Dy planes forming triplets (planes #0-#2 and #5-#7). Since two such neighboring triplets have opposite phases, the moments on planes #3 and #7 are 'frustrated' which can lead to antiferromagnetic ordering in these planes. This element of frustration can give rise to magnetic peak broadening below T_t as was observed to occur with high resolution XRES in $TbNi_2Ge_2$ [44]. Due to extinction, shape and absorption effects in the neutron diffraction measurements on a single-crystal sample, a precise determination of the tilt angle β at this temperature could not be carried out. However, a rough estimate is $\beta = 17^\circ \pm 6^\circ$. Neutron diffraction from powdered single grains sample is clearly needed for a better determination of β. Due to the high neutron absorption cross-section of Dy ($\sigma_a = 940$ barns, see Ref. [56]), however, a better technique in this case is XRES on a single-crystal sample for the moment direction determination as has been done in the $GdNi_2B_2C$, $SmNi_2B_2C$, $NdNi_2B_2C$ and $TbNi_2Ge_2$ compounds (see Refs. [67, 66, 44]).

The magnetic structure above T_t but below T_N is an AM structure described by a

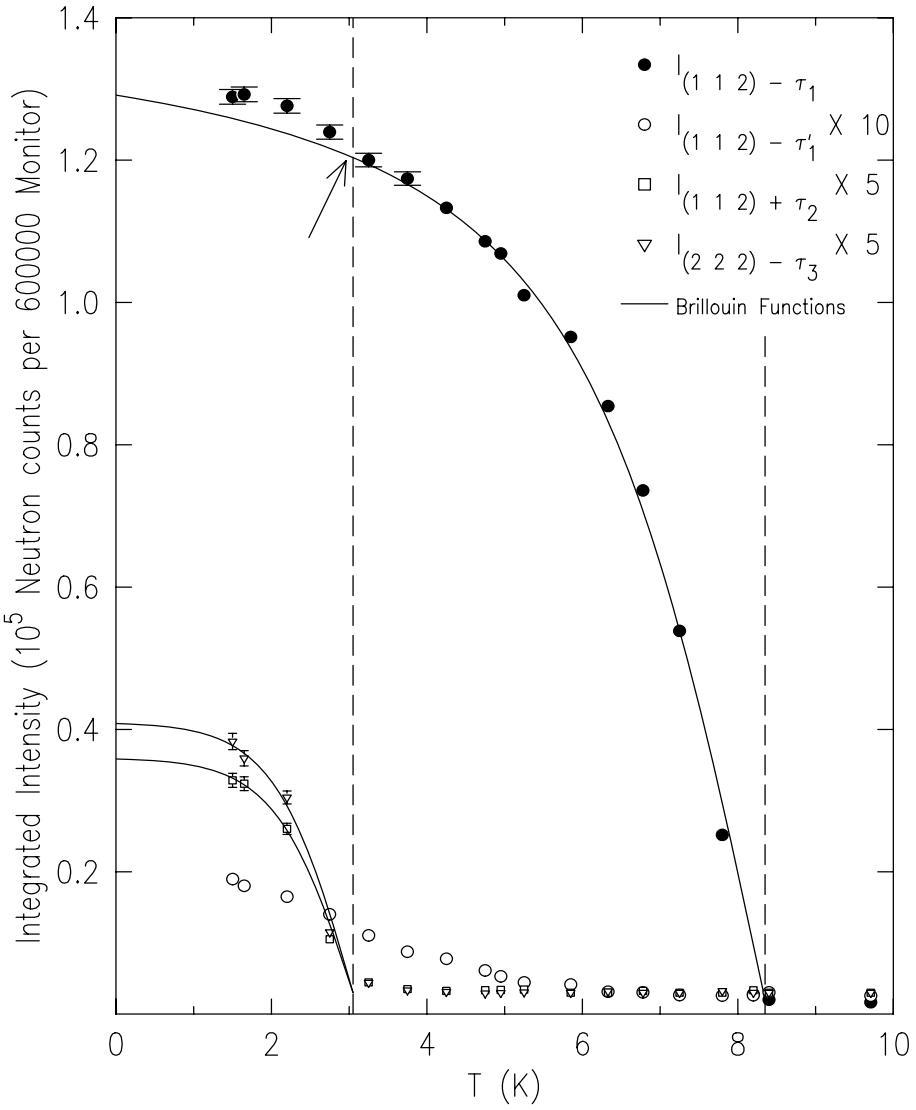

Figure 3.15 Temperature dependence of various magnetic reflections measured by neutron diffraction ($E_{neutron}$ = 14.7 meV) on a single crystal. The arrow shows the break in the $\boldsymbol{\tau}_1$ order parameter. The intensities of $\boldsymbol{\tau}_1'$ was multiplied by 10 and those of $\boldsymbol{\tau}_2$ and $\boldsymbol{\tau}_3$ satellites were multiplied by 5. Data were collected on raising the temperature. The vertical dashed lines locate the positions of the transition temperatures, T_N and T_t, respectively.

single propagation vector, $\boldsymbol{\tau}_1$, with no antiferromagnetic planes. The ordered moments are at an angle β from the $\hat{\mathbf{c}}$ axis. It is not clear if this β is different than that in the EM phase. The ordering scheme in $DyNi_2Ge_2$ just described is like that in $DyNi_2Si_2$. [27, 29] The magnetic structure of $DyNi_2Si_2$ below T_N=6 K but above T_t=3.7 K is sinusoidally AM. Below T_t, the structure becomes EM commensurate. It is surprising, however, unlike the magnetic structures in $DyNi_2Ge_2$, the ordered moments in $DyNi_2Si_2$ are aligned with the $\hat{\mathbf{c}}$ axis in both the phases, although the magneto-crystalline anisotropies in both the materials are comparable. On the other hand, $TbNi_2Ge_2$ and $TbNi_2Si_2$ are strongly anisotropic with the ordered Tb moments strictly aligned with the $\hat{\mathbf{c}}$ axis [44, 26].

The magnetic orderings in the three compounds $TbNi_2Ge_2$, $TbNi_2Si_2$ and $DyNi_2Si_2$, respectively, have two features in common. Below the respective ordering temperature, T_N, they all order in a long period AM structure. On further reducing the temperature the AM structure locks-into the lattice, becoming EM commensurate at a lower transition temperature, T_t. Due to the similar magnetic behavior of $DyNi_2Ge_2$, in particular with that found in $TbNi_2Ge_2$, one expects the modulation vector below T_N to be slightly different from $(0\ 0\ \frac{3}{4})$, found in the present neutron diffraction study, which implies a longer period of modulation, as is the case in the other materials above T_t but below T_N. The high resolution available to XRES measurements should be utilized in order to determine $\boldsymbol{\tau}_1$ more precisely.

Next, it should be noted that due to the four-fold symmetry of the tetragonal basal plane the possibility of a conical antiferromagnetic structure can not be ruled out. If, however, there is an in-plane easy direction of magnetization then all the ordered moments within a magnetic domain can be confined to a single plane formed by the easy in-plane direction and the $\hat{\mathbf{c}}$ axis, such as the model proposed in Fig. 3.16. One way to search for in-plane anisotropy is to measure the angular dependence of dc magnetization (see Ref. [77]) within the basal plane. Similarly, one can try to determine β in the paramagnetic phase if the anisotropy is solely due to CEF effects. Such measurements to

look for any such in-plane easy direction as well as to determine β are left for the future. In addition, the difference between a collinear EM structure and a spiral one can also be determined with x-rays as well, using circularly polarized light (see Ref. [78]). Also, Mössbauer spectroscopic measurements can be useful. Recently, this technique was employed [79] to distinguish between transverse sine-modulated and spiral-like structures that were proposed for the $GdNi_2B_2C$ by the XRES investigations [67].

Finally, the Néel transition temperature determined from the current neutron diffraction measurements is in agreement with that from the susceptibility measurements on single crystals and also with the one found in the earlier neutron work on a polycrystalline sample [40]. However, the results are inconsistent with the value of $\boldsymbol{\tau}_1$ = (0 0 0.788) found by the previous workers [40]. The $\boldsymbol{\tau}_2$ and $\boldsymbol{\tau}_3$ satellites were not detected in the earlier work on a powder sample because they are very weak and Dy has a very large absorption cross-section (see above). However, the large discrepancy of $\boldsymbol{\tau}_1$ cannot be explained so easily. Although strains induced by the grinding process can change the modulation, it is surprising that this could happen without significantly affecting T_N. An independent measurement using XRES can help resolve this discrepancy.

Summary

Both $TbNi_2Ge_2$ and $DyNi_2Ge_2$ have an AM structure below T_N with propagation vectors, $\boldsymbol{\tau}_1$, (0 0 $\sim$0.758) and (0 0 $\sim$0.75), respectively. The phase below T_t in both the compounds is an EM commensurate structure. This EM phase is described by a set of three modulation vectors, namely, $\boldsymbol{\tau}_1$=(0 0 $\frac{3}{4}$), along with its third harmonic, $\boldsymbol{\tau}_1'$=(0 0 $\frac{1}{4}$), $\boldsymbol{\tau}_2$=($\frac{1}{2}$ $\frac{1}{2}$ 0) and $\boldsymbol{\tau}_3$=($\frac{1}{2}$ $\frac{1}{2}$ $\frac{1}{2}$). The $\boldsymbol{\tau}_2$ and $\boldsymbol{\tau}_3$ modulations are due to the antiferromagnetically ordered planes present in the structure which may be the result of 'exchange frustrations' built into the EM structure. In both the phases the ordered moments in $TbNi_2Ge_2$ are aligned with the $\hat{\mathbf{c}}$ axis. In $DyNi_2Ge_2$, on the other hand,

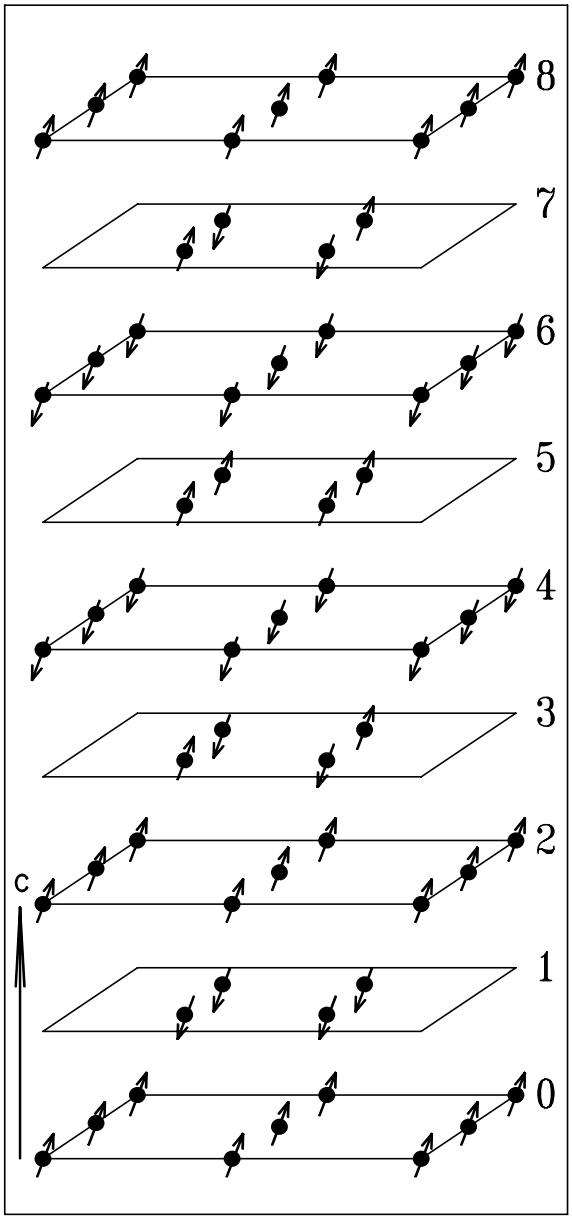

Figure 3.16 The magnetic unit cell of $DyNi_2Ge_2$ crystal below $T_t = 3.1$ K. The $\uparrow$ ($\downarrow$) represents the magnetic moment of Dy atoms (solid circles). Ni and Ge atoms have been omitted. The planes are numbered for reference.

the moments are canted away from the $\hat{\mathbf{c}}$ axis due to in-plane ordered component. At 1.5 K, this canting angle (β) is estimated to be $\sim 17°$. It is possible that β in the AM phase is slightly different from this value due to thermal population of the higher CEF levels. The rotation of the ordered moments away from the $\hat{\mathbf{c}}$ axis is consistent with the weaker anisotropy in $DyNi_2Ge_2$ observed in the paramagnetic phase compared to that of the uniaxial $TbNi_2Ge_2$.

4 BAND STRUCTURE ANALYSIS OF $R^{3+}Ni_2Ge_2$

Rare earth intermetallics with the tetragonal $ThCr_2Si_2$ structure have been the subject of intensive study for several decades because of their intricate magnetic structures and various correlated electron phenomena [1]. The complex crystal structure and multi-atom composition of these materials relative to the elemental rare earth metals allow for more involved band structures and magnetic interactions. While the experimental studies of their magnetism have focused on determination of the ordered states, a quantitative theoretical understanding of their magnetic phase transition is lacking. In this chapter a computational study of the band structure and magnetic interactions responsible for long-range order in the RNi_2Ge_2 compounds is initiated.

Diffraction studies on $TbNi_2Ge_2$ and $DyNi_2Ge_2$ presented in the previous chapter showed that at the onset of magnetic ordering at T_N the modulation vector in both the systems is of the form (0 0 q_z). Earlier neutron diffraction studies, reviewed in the first chapter, on other members of this series such as Nd, Ho, Er and Tm, also observed the propagation vectors to be of the same form as above with q_z in the range of 0.75-0.81 (see Table 1.1). Recently, XRES studies of $PrNi_2Ge_2$ and $SmNi_2Ge_2$ also revealed their magnetic wavevector to be (0 0 0.809) and (0 0 0.791), respectively (see Appendix E). As was already discussed, in these metallic systems with low ordering temperatures ($\lesssim$ 30 K) R atoms are well separated from each other ($\gtrsim$4 Å) so that direct overlap of two neighboring $4f$ shells is negligible. The interactions among these moment bearing atoms responsible for the magnetic ordering are believed to be of the RKKY indirect exchange type. This interaction is determined by the electronic band structure and Fermi surface

topology. In the case of elemental rare earths it is well established that nesting of the Fermi surface is responsible for their magnetic ordering. These observations suggest, by analogy, the hypothesis that Fermi surface nesting with $\mathbf{q}_{nest} = (0\ 0\ q_z)$ may also be responsible for magnetic ordering in $R\mathrm{Ni}_2\mathrm{Ge}_2$ compounds. In this chapter band structure analysis of the RKKY interaction is undertaken to investigate the hypothesis of nesting pertaining to magnetic ordering in the trivalent R members of this family of isostructural compounds.

RKKY Exchange Interaction and Generalized Susceptibility

In the simplest form of the RKKY theory the indirect exchange interaction between two well-separated rare earth ions takes place via the spin polarization of the conduction band electrons. The total exchange energy due to such pair-interactions of a set of N localized rare earth moments when their total angular momentum ($\mathbf{J}$) is a good quantum number may be written as [70]

$$\mathcal{H}_{\mathrm{RKKY}} = -\sum_{m>n}\left(\sum_{\mathbf{q}} J(\mathbf{q}) e^{i\mathbf{q}\cdot(\mathbf{R}_m-\mathbf{R}_n)}\right)\mathbf{J}_m\cdot\mathbf{J}_n, \tag{4.1}$$

where

$$J(\mathbf{q}) = \frac{2}{N}(g_J-1)^2\left|I(\mathbf{q})\right|^2\chi_0(\mathbf{q})\cdot \tag{4.2}$$

Here $\mathbf{q} = \mathbf{k}'$ - $\mathbf{k}$ is the wave vector difference between incident and scattered conduction electrons. $I(\mathbf{q})$ is the generalized exchange integral which is assumed to be a well-behaved, smoothly varying function only of $\mathbf{q}$. The expression for the $\mathbf{q}$-dependent bare static susceptibility for a noninteracting electron gas, is given by

$$\chi_0(\mathbf{q}) = \frac{1}{N}\sum_{n,n',\mathbf{k}}\frac{f(\epsilon_{n,\mathbf{k}})[1-f(\epsilon_{n',\mathbf{k}+\mathbf{q}+\mathbf{G}})]}{\epsilon_{n',\mathbf{k}+\mathbf{q}+\mathbf{G}}-\epsilon_{n,\mathbf{k}}}, \tag{4.3}$$

where $f(\epsilon)$ is the Fermi-Dirac occupation factor, ϵ's are the electronic energies, n and n' are the band indices and $\mathbf{G}$ is a reciprocal lattice vector needed to reduce $\mathbf{k}+\mathbf{q}$. When

$\mathcal{H}_{\text{RKKY}}$ is the dominant term to the free energy the stable magnetic structure is the one that minimizes this energy. By explicit consideration of a general helical structure[1] Nagamiya has shown [80] that the minimum of the exchange energy occurs at a single $\mathbf{q}$ where $J(\mathbf{q})$ is the maximum. Within the above approximations this happens at a $\mathbf{q}$ where $\chi_0(\mathbf{q})$ is a maximum (see Eqns. 4.1 and 4.3) assuming the variation of $I(\mathbf{q})$ to be small. The $\mathbf{q}$ that maximizes $\chi_0(\mathbf{q})$ also determines the modulation vector at the onset of magnetic ordering.

At this point some comments about the exchange integral, $I(\mathbf{q})$, are in order. In general, this integral should be written as $I_{n,n'}(\mathbf{k},\mathbf{k}')$ where n and n' are the band indices. In Eqn. 4.2 the variation of the exchange integral due to interband and intraband transitions has been ignored, allowing it to be factored out from the $\chi_0(\mathbf{q})$ summation in Eqn. 4.3. For the case of localized $4f$ electrons the $I_{n,n'}(\mathbf{q})$ approximation was found by Watson and Freeman [81, 82] to have some justification for the case of elemental Gd when the conduction electrons were described by simple orthogonalized plane waves (OPW) which are appropriate for a free-electron metal. This approximation leads to the intuitively appealing expectation that $I_{n,n'}(\mathbf{q})$ should be a deceasing function of $\mathbf{q}$ which can be seen as follows. Since the exchange is determined by the overlap of the conduction electron with the $4f$ electrons, a large $\mathbf{q}$ implies a rapid oscillation cancellation of this overlap, diminishing the exchange integral. This form of $\mathbf{q}$-dependence for the matrix elements has been used by Evenson and Liu in their theory of magnetic ordering in heavy rare earth metals [83]. However, this is undoubtedly an oversimplified picture, since augmented plane wave (APW) band structure calculations clearly showed that rare earth bands can not be approximated by those of free-electron metals [70]. Indeed, by explicitly determining the conduction electron wave function using the APW method, Harmon and Freeman [84] have made realistic calculations of the indirect exchange

[1]Note that collinear or longitudinal spin waves, flat spirals and conical antiferromagnet, all are special cases of this structure.

matrix elements for Gd metal which to date are the only such rigorous computations available. Their calculations revealed that, due to band crossing, the character of the wave function, changes rapidly. So, any analytical arguments for $I_{n,n'}(\mathbf{k},\mathbf{k}')$ based on simplified band structure and wave function such as those used in earlier work cited above, do not have general validity. Therefore, the exchange matrix elements can not be well described as slowly varying functions of $\mathbf{q}$. This work also showed the magnitude of the matrix elements to be largest for Bloch states with large $5d$ character [84, 85].

However, due to the complex band structure of a real material, one may expect the characteristics of the indirect exchange between two R ions to be determined primarily by the complicated energy dependence of the denominator in Eqn. 4.3. This assumption underlies the theory of magnetic phase transitions of rare earths which has been successful in correlating Fermi surface nesting to magnetic ordering in these metals. The reason is that Fermi surface topology has dramatic effects on the range of indirect exchange interaction between a pair of R atoms in real space as shown by L. Roth and co-workers [86]. Without recourse to the $\mathbf{q}$-approximation for $I_{n,n'}(\mathbf{k},\mathbf{k}')$ they found that for a general nonspherical Fermi surface the range of the exchange interaction falls off as $\frac{1}{r^3}$ where r is the distance between two atoms. In the special case of the spherical Fermi surface they rederived the RKKY expression [86]. $\chi_0(\mathbf{q})$ for this case is the classical Lindhard response function. However, for a cylindrical region with diameter $2k_f$, where k_f is the Fermi wavevector and an axis perpendicular to $\mathbf{r}$, where $\mathbf{r}$ is the separation vector between two R atoms, the exchange interaction between the two falls off as $\frac{1}{r^2}$ [86]. The corresponding $\chi_0(\mathbf{q})$ remains flat for $\mathbf{q} < 2k_f$ and rapidly drops off when $\mathbf{q} > 2k_f$ with a cusp at $2k_f$. Finally, in the case of flat regions separated by $2k_f$, which is known as nesting, or webbing, perpendicular to $\mathbf{r}$ this decay is only $\frac{1}{r}$ [86]. Such a large increase in the range of the exchange can be critical in cooperative phenomena such as a magnetic phase transition in metallic systems. Contributions to $\chi_0(\mathbf{q})$ from these regions exhibit a logarithmic divergence at $\mathbf{q} = 2k_f$. Therefore, one can indeed expect

nesting to play the key role in driving phase transitions as was originally proposed by Lomer [87] to explain the AF transition of Cr.

The computational procedure for correlating nesting to magnetic ordering then consists of three steps. First, the real band structure for a given material is calculated. Secondly, using these bands $\chi_0(\mathbf{q})$ is computed for $\mathbf{q}$ along the direction of interest, which is typically a high symmetry direction of the Brillouin zone, and the $\mathbf{q}_{peak}$ at the maximum is obtained. Finally, the regions of Fermi surface that nest with $\mathbf{q}_{nest}$=$\mathbf{q}_{peak}$ are found which determine the maximum of $\chi_0(\mathbf{q})$.

Band Structure and $\chi_0(\mathbf{q})$ Calculations for $LuNi_2Ge_2$

The goal of this section is to calculate $\chi_0(\mathbf{q})$ for $LuNi_2Ge_2$ and look for the maximum. Although nonmagnetic, this calculation is an important first step. The peak in $\chi_0(\mathbf{q})$ is expected to be close to the observed ordering vectors. Since Lu has a filled $4f$ shell, the $4f$ electrons can be treated conveniently and accurately as part of the core. It can be expected that if the unfilled $4f$ shells are treated as core electrons their paramagnetic bands will be similar to those of $LuNi_2Ge_2$. *Ab initio* local density approximation (LDA) electronic bands were calculated using the tight-binding linear-muffin-tin-orbital (TB-LMTO) method developed by the group of O. K. Andersen [88]. The atomic sphere approximation (ASA) with combined corrections was utilized. The scalar relativistic Schrödinger equation was solved. The von Barth-Hedin local potential was used to include exchange and correlation effects. The experimental structural constants at room temperature [22] were used for the calculations. Figure 4.1 shows the electronic bands calculated along various symmetry directions in the Brillouin zone (BZ).

Not all the bands are necessary for the $\chi_0(\mathbf{q})$ calculations, however. For example, flat bands close to the Fermi surface yield a $\mathbf{q}$-independent contribution to $\chi_0(\mathbf{q})$ unless they cross the Fermi surface. Bands far in energy from the Fermi level yield small

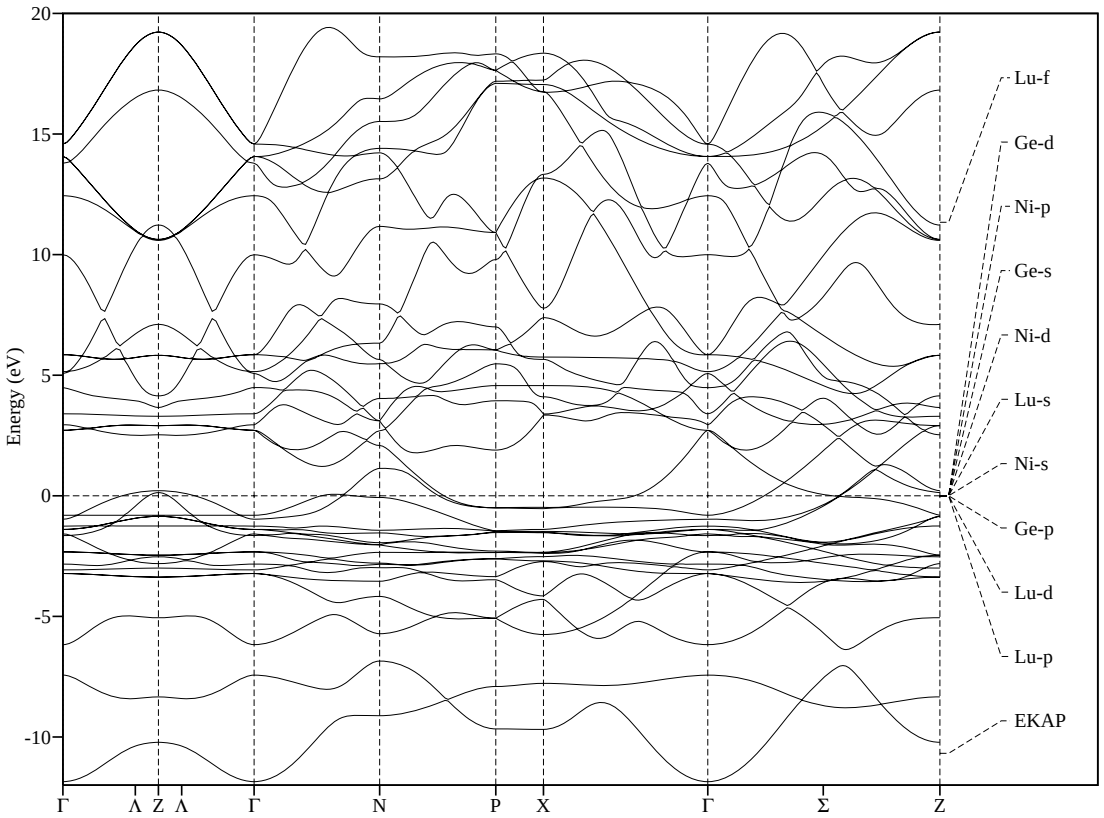

Figure 4.1 LDA paramagnetic electronic TB-LMTO-ASA band structure of $LuNi_2Ge_2$. The horizontal dashed line indicates E_f. The COG of each partial wave was held at E_f during the band calculation in the final iteration. That of Lu-5f was held at its SFC value. The two bands referred to as A and B lie right below E_f at Γ. The two bands crossing E_f along the ΓN line are also A and B. At Z these two bands are located right above E_f. Notice that there are significant number of band crossings. EKAP is related to the muffin-tin-zero.

contributions due to the large energy denominators. Thus, only the bands that cross the Fermi surface need to be considered [83]. For the $\chi_0(\mathbf{q})$ calculations four such bands were included. In order to get accurate bands close to the Fermi level (E_f) and an accurate description of the Fermi surface the center-of-gravity (COG) of each partial wave[2] was held fixed at E_f. This was done after the full self-consistent (SC) calculations to obtain the best potential were made, using a mesh of 16-16-8 along the three primitive reciprocal lattice vectors, respectively. Then one final iteration was performed to calculate the band structure with a high density of $\mathbf{k}$-points. For the $\chi_0(\mathbf{q})$ calculations, the analytical linear tetrahedron method, developed by Rath and Freeman [89], was used. $\chi_0(\mathbf{q})$ at T =0 K was calculated for $\mathbf{q}$ along [0 0 1] (ΓZ line) since all the ordering vectors cited above lie along this line. The irreducible section ($\frac{1}{16}$th of the BZ) was divided into 3584 small tetrahedra for the summation in Eqn. 4.3. The calculated susceptibility is shown in Fig. 4.2. It is gratifying to find a maximum at (0 0 0.86), close to the observed ordering vectors. Although all four bands that cross E_f were included, the peak in $\chi_0(\mathbf{q})$ was determined by the dominant interband contributions (see Fig. 5.6) from two bands, hereafter referred to as A and B. At any $\mathbf{k}$-point A and B refer to the 15th and 16th bands, respectively, where the valence band with the lowest energy is considered to be the 1st band. The interband (A$\leftrightarrow$B) nesting responsible for the maximum is similar to those shown in Fig. 5.7.

The results presented above strongly support the connection of nesting to magnetic ordering in RNi$_2$Ge$_2$. Similar calculations [6] for LuNi$_2$B$_2$C also suggested nesting to be responsible for magnetic ordering in RNi$_2$B$_2$C compounds. Although such suggestions have qualitative theoretical basis as presented above, they do not establish any direct correlation. In all the RNi$_2$Ge$_2$ compounds cited at the beginning of this chapter the R ions are trivalent with different anisotropic $4f$ moments but the same band filling. In order to establish a direct correlation between Fermi surface nesting and the magnetic

[2]Lu-5f COG was kept at its SC value which is much higher in energy.

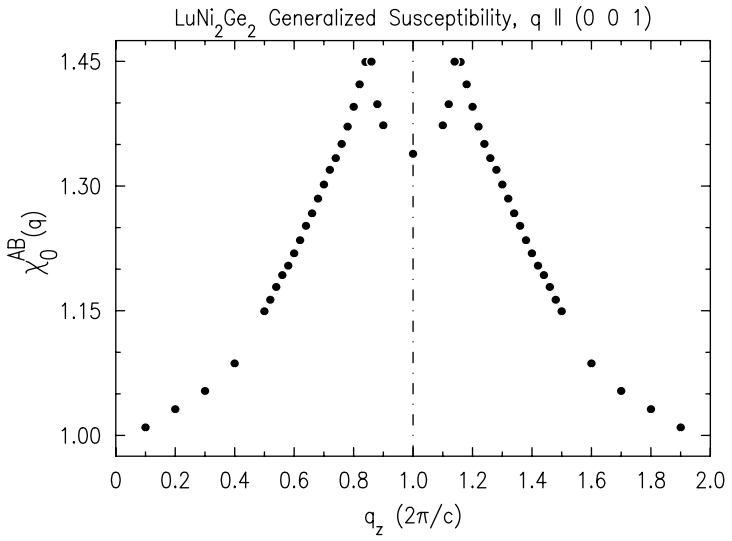

Figure 4.2 The generalized interband (A↔B) susceptibility of $LuNi_2Ge_2$. Note the maximum at 0.86 with ∼45% enhancement relative to $\chi_0(0)$. $\chi_0(\mathbf{q})$ was calculated across two zones to show the periodicity. The vertical dotted-dashed line is the zone boundary at Z, (0 0 1).

ordering observed, one needs to change manifestly the band filling and keep the same moment in isostructural systems. Since band filling alters the Fermi surface topology, nesting is also changed. So, if nesting features are truly responsible for magnetic ordering, such changes in band filling should also transform the magnetic structures, which can be dramatic. $EuNi_2Ge_2$ and $GdNi_2Ge_2$ are precisely such systems providing the opportunity to further explore, both experimentally and computationally, the conjecture of nesting and the effects of band filling on magnetic structure.

5 THE EFFECTS OF BAND FILLING ON MAGNETIC STRUCTURE: THE CASE OF $GdNi_2Ge_2$ AND $EuNi_2Ge_2$

In the previous chapter band structure analysis of the $R^{3+}Ni_2Ge_2$ compounds provided strong support for the hypothesis of Fermi surface nesting as the driving mechanism of the magnetic phase transition in these materials and suggested that band filling may have significant effect on the ordered ground state. This chapter is focused on two particularly interesting members, $GdNi_2Ge_2$ and $EuNi_2Ge_2$, of this series in order to further investigate the nesting hypothesis for the Néel transition and to study the effects of band filling on magnetic structures of these intermetallics.

From the susceptibility (see Ref. [23] and below) and Mössbauer spectroscopic [37] measurements, Gd and Eu in these compounds are known to be trivalent and divalent, respectively, in ambient pressure. This means that the orbital angular momentum in both of them is zero due to their half-filled $4f$ shells. The Hund's rule ground state is ${}^8S_{\frac{7}{2}}$ which gives an isotropic magnetic moment unaffected by the CEF. So, their magnetic long-range order and concomitant anisotropy are determined solely by the RKKY interaction, $\mathcal{H}_{\text{RKKY}}$. This isotropic bilinear exchange interaction, $\mathcal{H}_{\text{RKKY}}$, discussed in the earlier chapters is strictly valid for the isotropic systems like Gd^{3+} and Eu^{2+} compounds [90]. In the case of rare earths with orbital angular momentum in their ground state, such as Tb and Dy studied earlier, two further approximations, that the conduction electron wave functions have spherical (s-type) symmetry and its wavelength is large compared with the size of the $4f$ shell, must be made [90]. Although the second approximation

has some justification, since the size of the $4f$ shell is $\sim$0.4 Å, the validity of the first assumption is dubious, since the conduction electron wave functions can have considerable angular dependence due to their large $5d$ character [84, 85]. Since such restrictions do not apply to the Gd and Eu systems one can expect to make systematic changes in the RKKY interactions by band filling without nullifying the validity of the isotropic bilinear form of $\mathcal{H}_{\text{RKKY}}$. Therefore, they provide a good opportunity to study the effects of band filling on magnetic ground states in a complex crystal structure such as that of $R\text{Ni}_2\text{Ge}_2$ intermetallic compounds which allow for complicated electronic structure involving crossings of multiple bands with different orbital character.

According to the hypothesis of nesting, an incommensurate ordering wave vector, such as those found in the other trivalent members of the series, in GdNi_2Ge_2, can be expected. However, due to the divalency of Eu in EuNi_2Ge_2, its magnetic ordering, in particular the modulation vector, is expected to be significantly different. From the experimental point of view it is advantageous to solve these magnetic structures by employing the XRES technique, since naturally abundant isotopes of Eu and Gd having large neutron absorption cross-sections render theses compounds neutron opaque. This problem is compounded by the rather small sizes of the available single crystals making conventional neutron diffraction methods rather difficult. Theoretically, on the other hand, it is possible to correlate the differences between the ordered states to the underlying electronic structures using band structure and $\chi_0(\mathbf{q})$ calculations.

Susceptibility and Magnetization

The temperature dependence of the low-field susceptibilities ($\chi(T)$) with the applied field parallel ($\chi_\parallel$) and perpendicular ($\chi_\perp$) to the $\hat{\mathbf{c}}$ axis in both the materials were found to be nearly isotropic above T_N in the paramagnetic phases. The effective magnetic moments of Gd and Eu, extracted from Curie-Weiss fits to high temperatures suscepti-

bility, are 7.69 μ_B and 8.0 μ_B, respectively, in agreement with theoretical expectations. This indicates that Gd is trivalent in this material, while Eu is divalent. From cusps in the susceptibility two transitions were identified which are indicated in Fig. 5.1(a) and (c). In $GdNi_2Ge_2$ the paramagnetic-to-AF phase transition occurs at 27.1 K (T_N) while a second transition occurs at a lower temperature of 16.8 K (T_t). In the case of $EuNi_2Ge_2$, T_N and T_t are 30.8 K and 13.4 K, respectively. Note that T_N for $EuNi_2Ge_2$ is surprisingly higher ($\sim$13.7%) than that of $GdNi_2Ge_2$ which is in direct contrast to the expectation of a lower T_N in $EuNi_2Ge_2$ due to weaker $4f$-$5d$ exchange interaction in atomic Eu compared to that in Gd [91]. The transition temperatures above are at variance with the results of earlier works [37] on polycrystalline samples where only the Néel transitions were observed. This may be due to polycrystalline averaging which often makes the lower transitions less pronounced, as was found to occur in $GdNi_2B_2C$ [35]. Also, in the case of the Gd compound the reported [37] T_N of 22 K disagrees significantly with the present results. In the Gd compound, $\chi_\perp$ has an upturn and a maximum at T_t'=18.5 K, occuring between T_N and T_t. $\chi_\parallel$, however, does not show such behavior. In-plane resistivity measurements showed only the transitions at T_N and T_t [23].

In the Eu compound, below T_N, $\chi_\parallel$ continues to increase and $\chi_\perp$ decreases. The low temperature magnetization with field along the $\hat{\mathbf{c}}$ axis increases linearly. These behaviors are similar to those of a "canonical" simple AF material and suggest that the ordered moments in $EuNi_2Ge_2$ are in the basal plane. For $GdNi_2Ge_2$, on the other hand, similar behavior is observed only below T_t and above this transition the susceptibilities ($\chi_\parallel$ and $\chi_\perp$) are of the same magnitude. These observations are consistent with the development of an ordered component of the moments along the $\hat{\mathbf{c}}$ axis above T_t while below this transition, the moments are locked into the plane as in $EuNi_2Ge_2$. This is the first set of experimental observations of significant qualitative differences between the ordered states below T_N. The magnetization measurements with the field applied in the plane

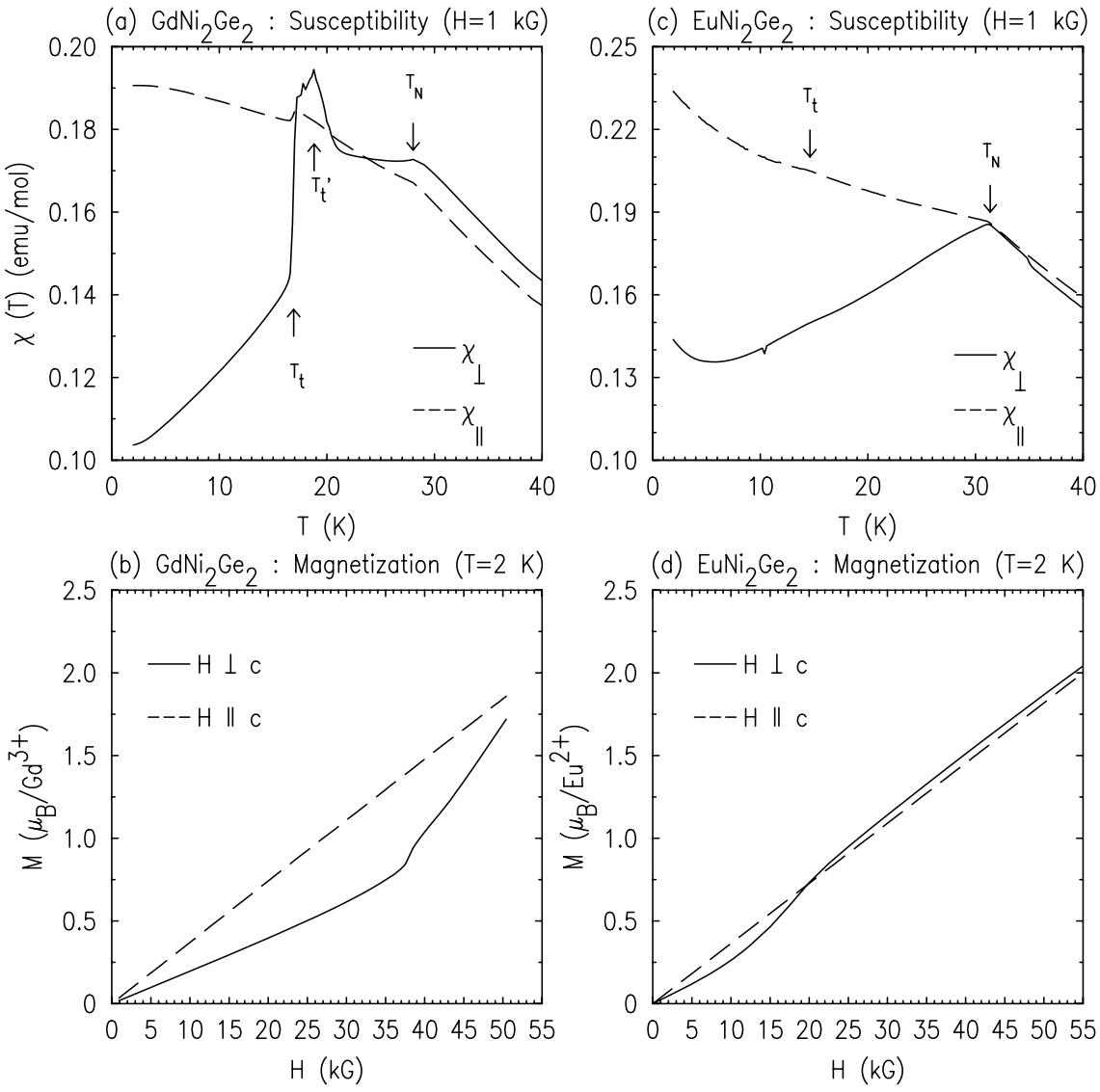

Figure 5.1 Temperature dependent magnetic susceptibility ((a), (c)) and the low temperature magnetization ((b), (d)) measurements of $EuNi_2Ge_2$ and $GdNi_2Ge_2$ compounds.

show one metamagnetic transition, defined at the breaks, in both the materials as shown in Fig. 5.1 (b) and (d).

Magnetic Ordering in $GdNi_2Ge_2$ and $EuNi_2Ge_2$ Compounds

In order to determine the microscopic magnetic structures of $GdNi_2Ge_2$ and $EuNi_2Ge_2$ XRES studies were performed. $GdNi_2Ge_2$ was studied on the C1 station beamline at the Cornell High Energy Synchrotron Source (CHESS). The incident beam was monochromatized using a double-bounce Si(111) monochromator with the second crystal performing sagittal focusing. No mirror was utilized. The approximate beam dimension in the vertical direction was 1 mm. No polarization analysis of the scattered beam was performed in these experiments. The XRES studies of $EuNi_2Ge_2$ were performed on the X22C beamline at the NSLS as described before. Closed cycle displex and Heliplex-4 cryostats (with base temperature of 13 K and 3.7 K, respectively) were used to cool the $GdNi_2Ge_2$ and the $EuNi_2Ge_2$ samples, respectively. Integrated intensities were measured using a liquid-nitrogen-cooled Ge solid state detector. The sample mosaic at (0 0 6) was approximately 0.05° for both samples.

The samples for the XRES studies were mounted with the $[h\ h\ l]$ zone in the scattering plane. This was chosen to look for modulations such as $(\frac{1}{2}\ \frac{1}{2}\ 0)$ and $(\frac{1}{2}\ \frac{1}{2}\ \frac{1}{2})$, as were observed in the Tb and Dy compounds described above. The primary beam energy was tuned to the respective L_{II} edges of Eu and Gd in order to use the resonant enhancement which is expected to be larger at the L_{II} edge than that at the L_{III} edge as was mentioned earlier.

Fermi Surface Nesting and Magnetic Ordering

In $GdNi_2Ge_2$, well above T_N determined from the susceptibility measurements, only charge peaks consistent with the body-centered tetragonal lattice ($h + k + l = 2n$ where

n is an integer) were observed. At 13 K, careful scans along $\hat{\mathbf{c}}^*$ revealed magnetic satellites corresponding to $\mathbf{q}_{Gd}$ = (0 0 0.805) (see Fig. 5.2). In Fig. 5.3 the energy scans of the $(0\ 0\ 6)^-$ magnetic superlattice peak through the Gd L_{II} and L_{III} edges are shown. In both the cases strong resonant enhancements take place above 2-3 eV above the absorption edges, defined at the inflection point of the respective fluorescence curves (see Fig. 5.3), consistent with its magnetic origin. This indicates the dipolar (*E1*) nature of the transitions involved in the resonances. Although it is difficult to determine the true resonant enhancement, one can estimate it by comparing the peak intensity at the resonance to that at 20 eV (the widths of the resonances are $\sim$ 3 eV) below the resonance. This allowed for an estimation of the enhancement factor which is $\sim$80 at the L_{II}-edge and $\sim$20 at the L_{III}-edge, respectively. All subsequent measurements were carried out at the L_{II}-edge.

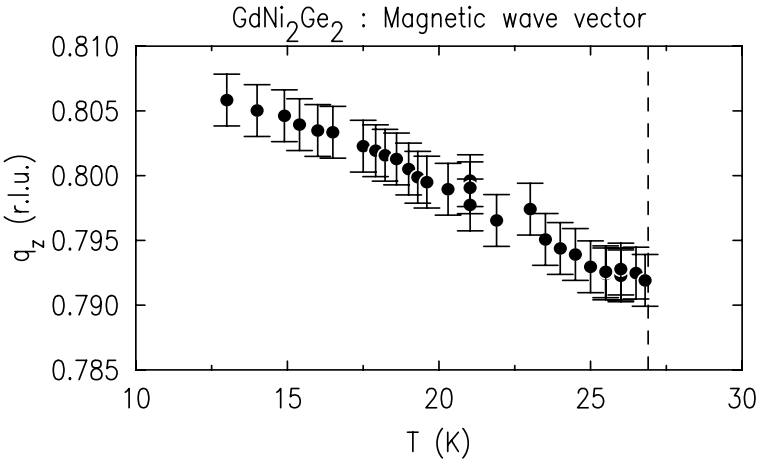

Figure 5.2 The temperature dependence of the magnetic modulation vector, $\mathbf{q}_{Gd}$ = (0 0 q_z), observed at $(0\ 0\ 6)^-$. The dashed line locates T_N as determined from the integrated intensity measurements (see below).

The temperature dependence of $\mathbf{q}_{Gd}$ showed continuous variation with increasing temperature, reaching a value of (0 0 0.793) just below T_N, indicating the incommensurate nature of the ordered state (see Fig. 5.2). Within the experimental uncertainties no

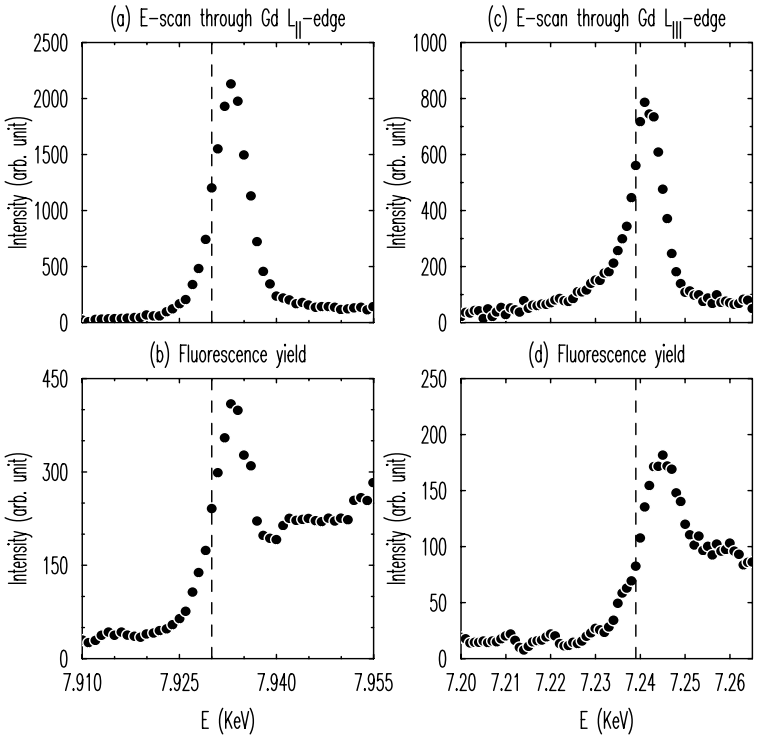

Figure 5.3 Energy scans of $(0\ 0\ 6)^-$ magnetic satellite through the Gd (a) L_{II} and (c) L_{III} edges. The fluorescence yields for both the edges are shown in the bottom panels, (b) and (d), as energy references. The dashed lines show the position of the respective absorption edges.

discontinuity or locking-in to some commensurate value below T_N, particularly in the region where in-plane susceptibility shows an upturn and a maximum, was found. In addition, the longitudinal width of the magnetic peaks, which is inversely proportional to the magnetic correlation length, was found to be practically temperature independent.

In order to trace the origin of $\mathbf{q}_{Gd}$ to Fermi surface nesting $\chi_0(\mathbf{q})$ was calculated. The band structure was calculated using the same method used for $LuNi_2Ge_2$, treating the $4f$ electrons as part of the core. This is consistent with the observed effective moments (see above) as well as x-ray photoemission measurements which found the $4f$ level to be $\sim$600 mRyd below the Fermi level (E_f) in $GdNi_2Ge_2$ [92]. The experimental lattice constants at room temperature [22] were used in these calculations. A finer mesh,

compared to that used for $LuNi_2Ge_2$, with 24-24-12 divisions along the three primitive reciprocal lattice vectors, respectively, was used in the SCF calculations. The band structure for $GdNi_2Ge_2$ as shown in Fig. 5.4 was found to be qualitatively similar to that of $LuNi_2Ge_2$. As before, $\chi_0(\mathbf{q})$ for $\mathbf{q}$=(0 0 q_z) was calculated at 0 K using the analytical linear tetrahedron method [89].

The $\chi_0(\mathbf{q})$ calculations for $GdNi_2Ge_2$ were carried out including the two bands, referred to as A and B earlier, which cross E_f, since they were found to be the dominant contributors in the case of $LuNi_2Ge_2$. Figure 5.5(a) shows the calculated interband (A$\leftrightarrow$B) $\chi_0^{\mathrm{AB}}(\mathbf{q})$ (filled circles) for $GdNi_2Ge_2$. There is a sharp peak at 0.79, very close to the ordering vector, with an enhancement of 53% relative to $\chi_0^{\mathrm{AB}}(\mathbf{q}\rightarrow 0)$, which is a measure of strength of the peak. The maximum is determined by the dominant interband (A$\leftrightarrow$B) contribution to $\chi_0(\mathbf{q})$ as shown in Fig. 5.6. It is interesting to recall that such interband nesting also played the critical role of determining the modulation vector of the spin density wave in Cr [87, 93]. The nesting vector, $\mathbf{q}_{nest}$ = (0 0 0.79), is indicated in Fig. 5.7 by the arrows. The $\chi_0(\mathbf{q})$ calculations shown here were performed with the Fermi energy shifted upward by 7 mRyd (to E_f'). This changed the peak position in $\chi_0(\mathbf{q})$ from 0.86 (as was observed for $LuNi_2Ge_2$) to 0.79. Such a shift is not unreasonable for band calculations using the ASA, when four bands with different orbital character cross E_f. Also, it should be pointed out that in the ASA the nonshperical components of the potential are neglected. So, the accuracy of the one-electron energies obtained with the ASA is $\sim$1% of the appropriate bandwidth. This corresponds to approximately 10 mRyd, 15 mRyd, and 5 mRyd for transition metal s, p, and d bands, respectively [88].

In order to show that this peak is robust the $\chi_0(\mathbf{q})$ calculations were repeated, including two more bands, one below and one above band pair A and B. According to these calculations the peak at 0.79 is the *global* maximum. This is illustrated in Fig. 5.6 which displays the interband and intraband contributions to the total $\chi_0(\mathbf{q})$ separately.

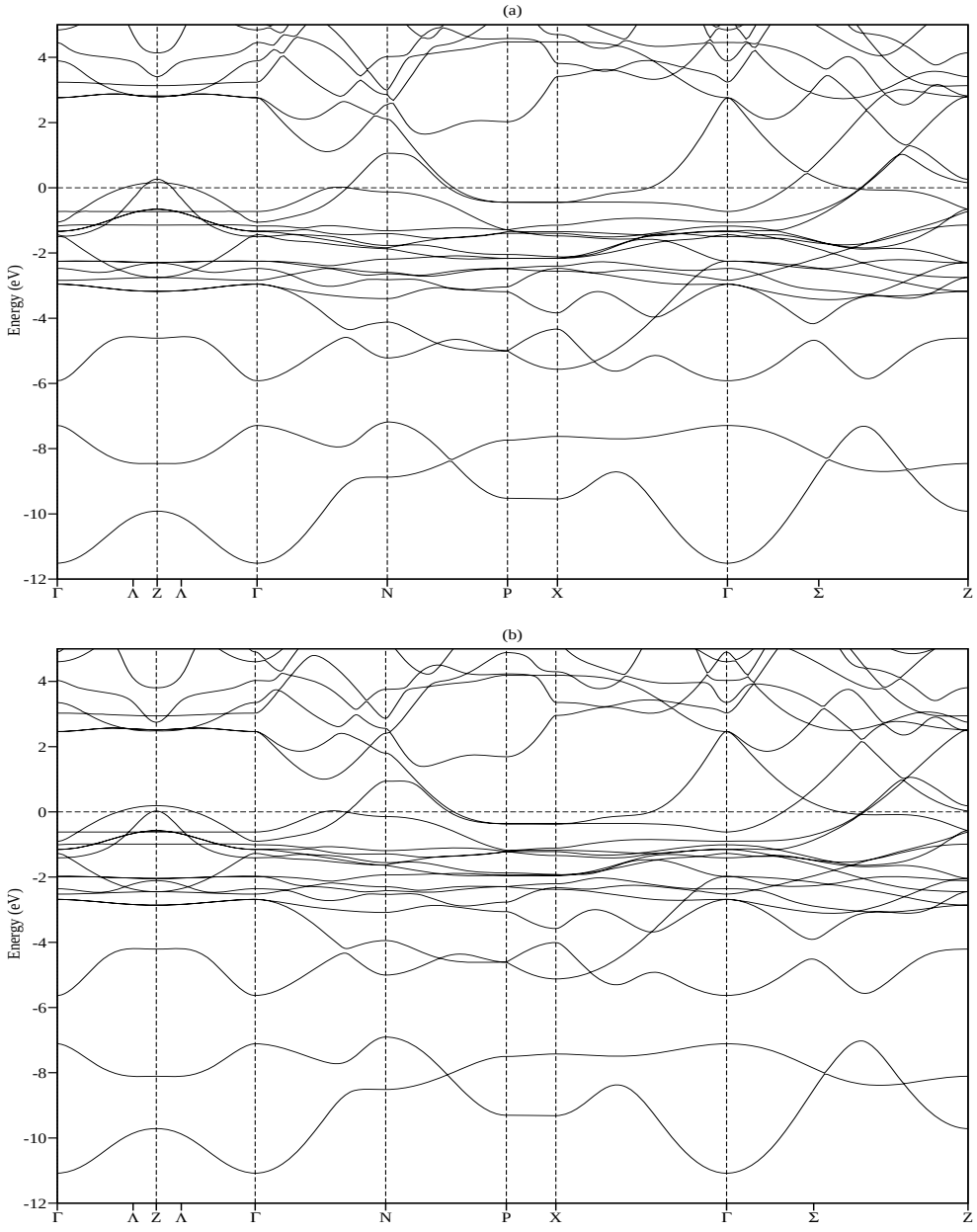

Figure 5.4 The electronic band structures of (a) $GdNi_2Ge_2$ and (b) $GdNi_2Ge_2$ with $EuNi_2Ge_2$ lattice parameters, respectively

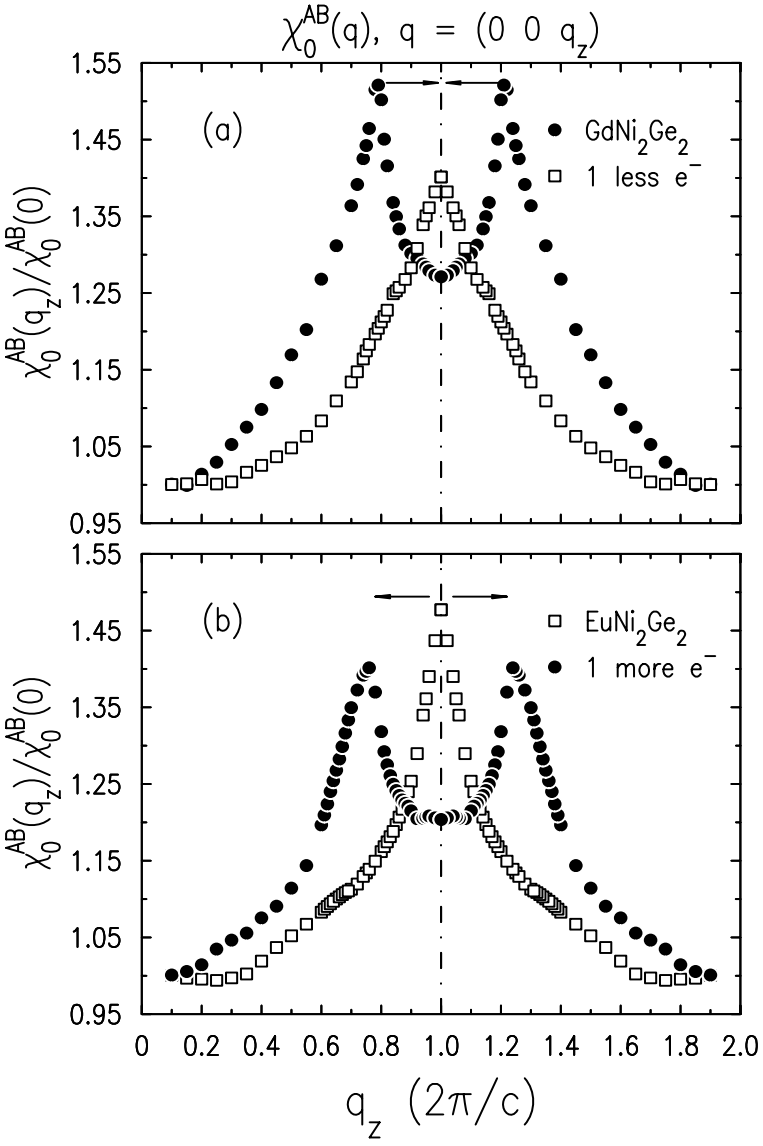

Figure 5.5 Interband generalized electronic susceptibility, $\chi_0^{\rm AB}(\mathbf{q})$. See text for details.

All the interband contributions except those of A and B add up to a **q**-independent large "background." By far the largest individual strongly **q**-dependent contribution comes from the interband A↔B transitions (second panel from the top in Fig. 5.6), which determines the global maximum of the total susceptibility to be at 0.79, as shown in the top panel. The total intraband susceptibility $\chi_0^{\text{intra}}(\mathbf{q} \to 0)$ reached 99.8% of $\frac{1}{2}N(E_f')$ where $N(E_f')$ is the density-of-states (DOS) at E_f' (Fig. 5.8). This is a measure of the precision of the tetrahedron integration scheme, a considerable improvement from the case of elemental rare earths, where agreement was in the range of 80-90% [94], using a scheme with poor numerical accuracy.

Due to the sensitivity of the nesting features to Fermi surface topology, a small shift of the calculated E_f directly affects $\mathbf{q}_{nest}$. In the elemental rare earths E_f depends on the $5d$ occupancy, which changes with the ionic core volume across the series. This d-band occupancy is responsible for the sequence of crystal structures observed across the rare earth series [95]. This suggests that small variations of E_f across the $R\text{Ni}_2\text{Ge}_2$ series may also be responsible for the range of q_z observed. Indeed, essentially the entire range of observed q_z exists within ±2.5 mRyd of E_f' and it may be concluded that magnetic ordering in $R\text{Ni}_2\text{Ge}_2$ with *trivalent* R elements is also driven by Fermi surface nesting. It should, however, be mentioned that exchange matrix elements [94, 96, 97, 84] ignored in present calculations and finite temperature [98] can also affect both position and the magnitude of the maximum in $\chi_0(\mathbf{q})$.

Although the calculations, so far, are consistent with the experimental findings, to directly observe a correlation between nesting and magnetic ordering the band filling must be changed. Computationally this can be accomplished simply via lowering E_f' by 22 mRyd, corresponding to the removal of exactly 'one' electron from GdNi_2Ge_2 according to its DOS (see Fig. 5.8) in order to simulate EuNi_2Ge_2, and calculating $\chi_0(\mathbf{q})$. The theoretical results can then be tested by XRES investigations on EuNi_2Ge_2 which is an experimental manifestation of this computational construct. Figure 5.5(a)

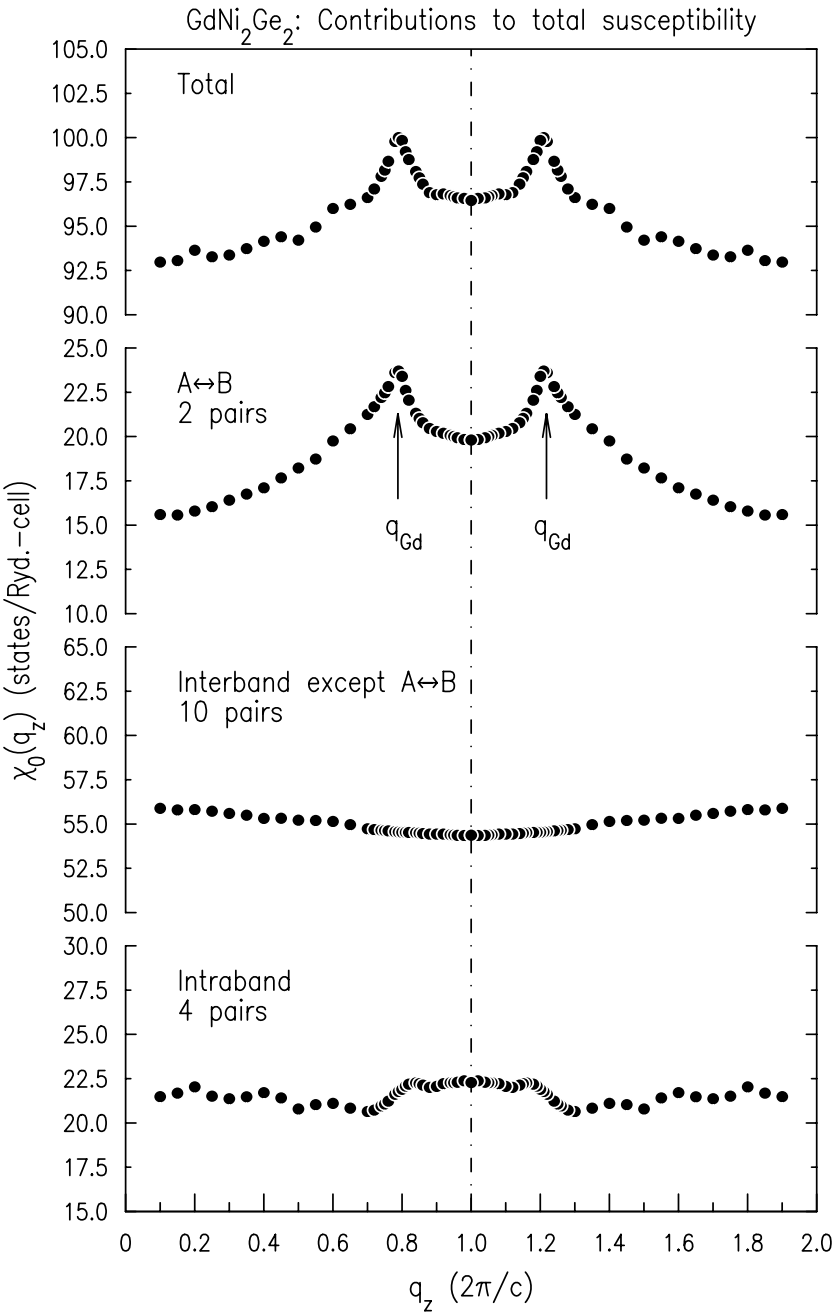

Figure 5.6 Total (top panel), interband (A↔B, $\chi_0^{\rm AB}(\mathbf{q})$), interband (remaining pairs) and intraband ($\chi_0^{\rm Intra}(\mathbf{q})$, bottom panel) generalized electronic susceptibility for $GdNi_2Ge_2$, respectively. Notice that the dominant $\mathbf{q}$-dependent contribution comes from $\chi_0^{\rm AB}(\mathbf{q})$ which determines the global maximum of the total $\chi_0(\mathbf{q})$.

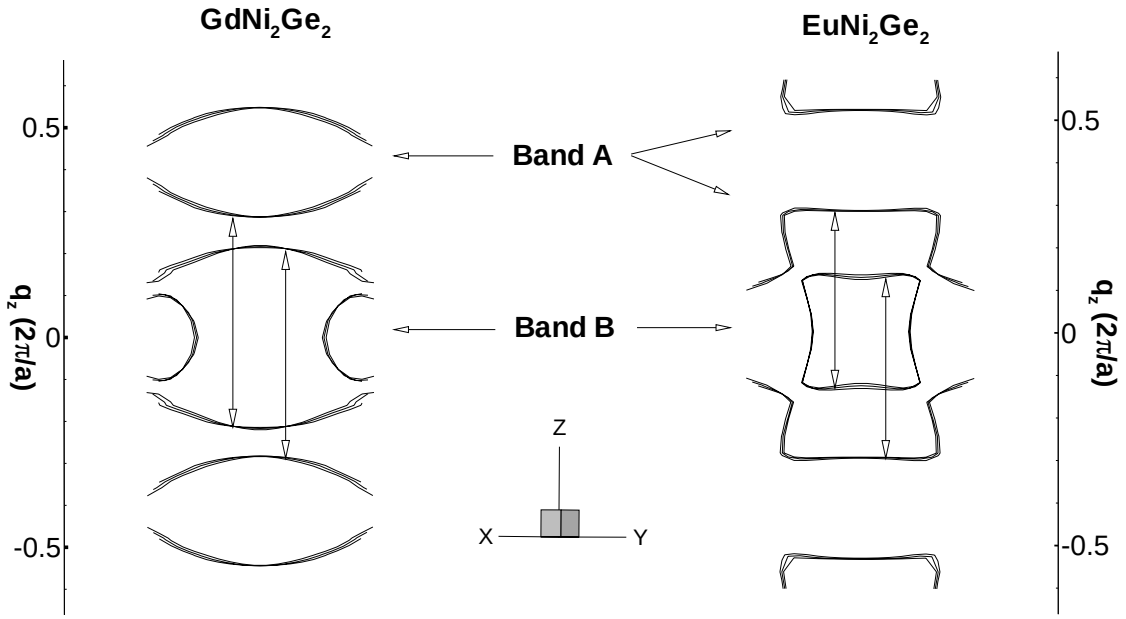

Figure 5.7 Interband (A↔B) nesting in $GdNi_2Ge_2$ and $EuNi_2Ge_2$. A and B form a nested pair of "saddles" over a considerable region. Contour plots on three parallel planes $\perp[1\ 1\ 0]$ of a portion of such regions with $\mathbf{q}_{nest}$ indicated by the arrows. Due to four-fold symmetry there are four such nested regions. $\mathbf{q}_{nest}$ for $GdNi_2Ge_2$ needs to be reduced to the first BZ. Note that the unit used for q_z is $\frac{2\pi}{a}$.

(open squares) presents $\chi_0(\mathbf{q})$ calculations with the lower band filling which show a strong sharp peak at the zone boundary, (0 0 1), predicting a *commensurate* simple AF structure in $EuNi_2Ge_2$. XRES measurements to verify this prediction were carried out at the Eu L_{II} edge. Indeed, at 4.3 K, scans along the $\hat{\mathbf{c}}^*$ axis found a superlattice peak at $\mathbf{q}_{Eu} = (0\ 0\ 1)$ which showed $E1$ resonant behavior, remained locked in position up to T_N, and disappeared above T_N. No other modulations in the $[h\ h\ l]$ zone were found.

Encouraged by this result $\chi_0(\mathbf{q})$ calculations for $EuNi_2Ge_2$ were performed to confirm the origin of this modulation to be nesting. The electronic bands calculated using the same method described above are shown in Fig. 5.9. Notice that although there are qualitative similarities of these bands to those of $GdNi_2Ge_2$ the Fermi level is located

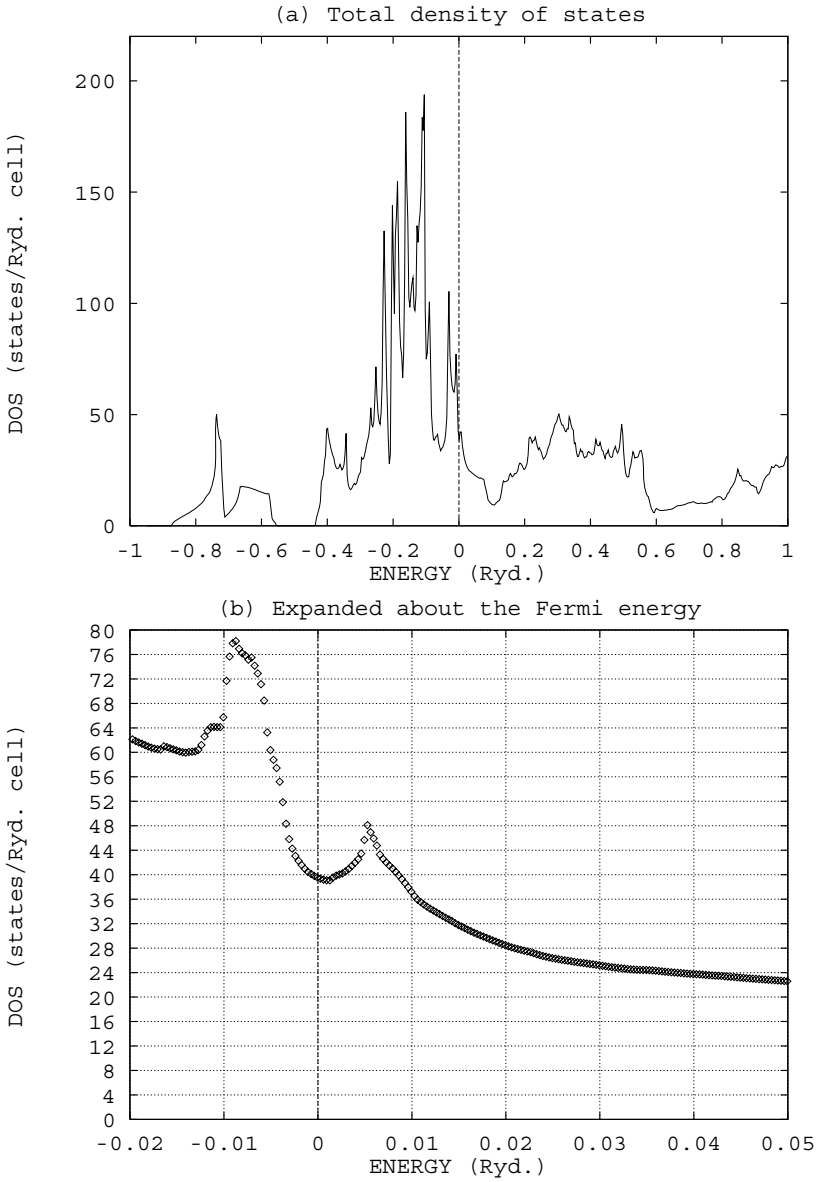

Figure 5.8 Density of states (DOS) for $GdNi_2Ge_2$. Energy is plotted relative to the Fermi level (obtained from the LMTO calculations), E_f, at zero. $\chi_0(\mathbf{q})$ calculations were performed with E_f shifted upward by 7 mRyd to E_f'. (a) The total DOS and (b) blown-up region centered on E_f to facilitate the calculation of energy corresponding to electron removal.

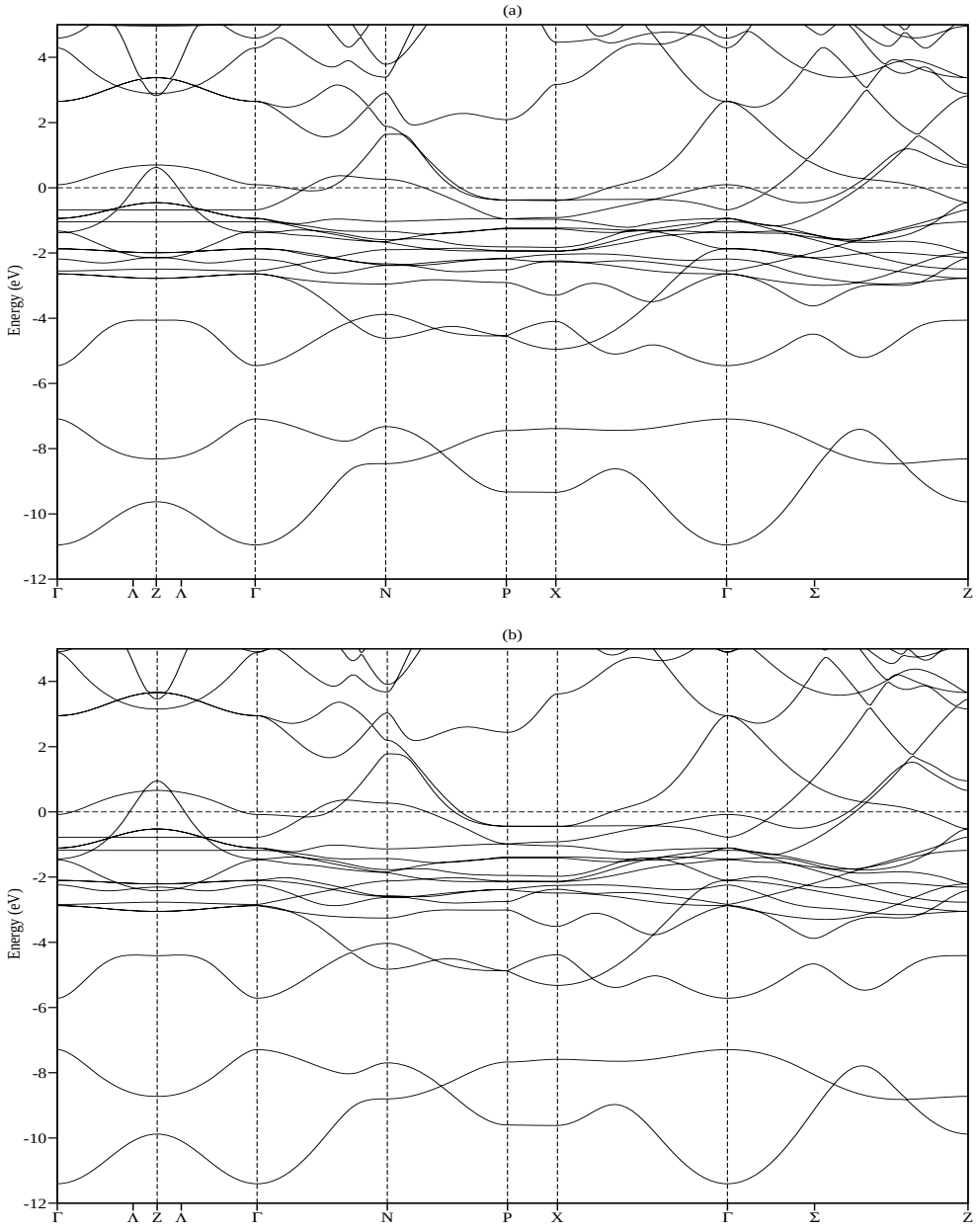

Figure 5.9 Electronic band structures of (a) $EuNi_2Ge_2$ and (b) $EuNi_2Ge_2$ with $GdNi_2Ge_2$ lattice parameters, respectively.

at a lower energy due to lower band filling. The results of $\chi_0(\mathbf{q})$ calculations, using bands A and B, are shown in Fig. 5.5(b). There is indeed a sharp peak at q_z=1 which is also the *global* maximum. As in the Gd case, the $\chi_0(\mathbf{q})$ shown is obtained with E_f shifted upward (to $E_f'' = E_f$+10 mRyd). The peak in $\chi_0(\mathbf{q})$ due to interband (A↔B) nesting occurs at the zone boundary for $E_f'' \pm 2$ mRyd, which is consistent with the commensurate nature of $\mathbf{q}_{Eu}$. Furthermore, this peak shifts to 0.78 on addition of 'one' electron (corresponding to E_f''+23 mRyd obtained from DOS of $EuNi_2Ge_2$, Fig. 5.10), in excellent agreement with that for $GdNi_2Ge_2$.

Up to this point the fact that the lattice constants of $EuNi_2Ge_2$ are ∼3% larger than those of $GdNi_2Ge_2$ [22] has been ignored. In order to assess the influence of this difference upon the nesting all the band and $\chi_0(\mathbf{q})$ calculations were repeated by swapping the lattice parameters between the two compounds. It is noted that placing Eu in the $GdNi_2Ge_2$ lattice is equivalent to applying pressure to it. It is known that $EuNi_2Ge_2$ undergoes a valence transition, where Eu becomes trivalent, at a pressure of 5 GPa [99] with corresponding lattice constants of ∼4 Å and $\lesssim$ 9.7 Å, respectively. At about 2.5 GPa, Eu enters into an intermediate valence state and the corresponding lattice constants are ∼4.08 Å and ∼9.94 Å, respectively. This indicates that the Eu $4f$ levels may be energetically close to E_f. However, the purpose of the present calculations is to isolate the effects on nesting due to differences in the lattice constants, holding the band filling fixed, and show that the nesting is robust with respect to such changes. So, the Eu $4f$ electrons are treated as part of the core. The electronic structures of $GdNi_2Ge_2$ with $EuNi_2Ge_2$ lattice parameters and vice versa are shown in Figs. 5.4(b) and 5.9(b), respectively. An inspection of these band structures shows that, in general, they are qualitatively similar to each other and to those of the 'pure' compounds with their own lattice parameters as shown in Figs. 5.4(a) and 5.9(a), respectively. $\chi_0(\mathbf{q})$ calculated using these bands is displayed in Fig. 5.11. In the case of $GdNi_2Ge_2$ (Fig. 5.11(a)) the peak is at 0.77 whereas the peak in $EuNi_2Ge_2$ (Fig. 5.11(b)) appears at the zone

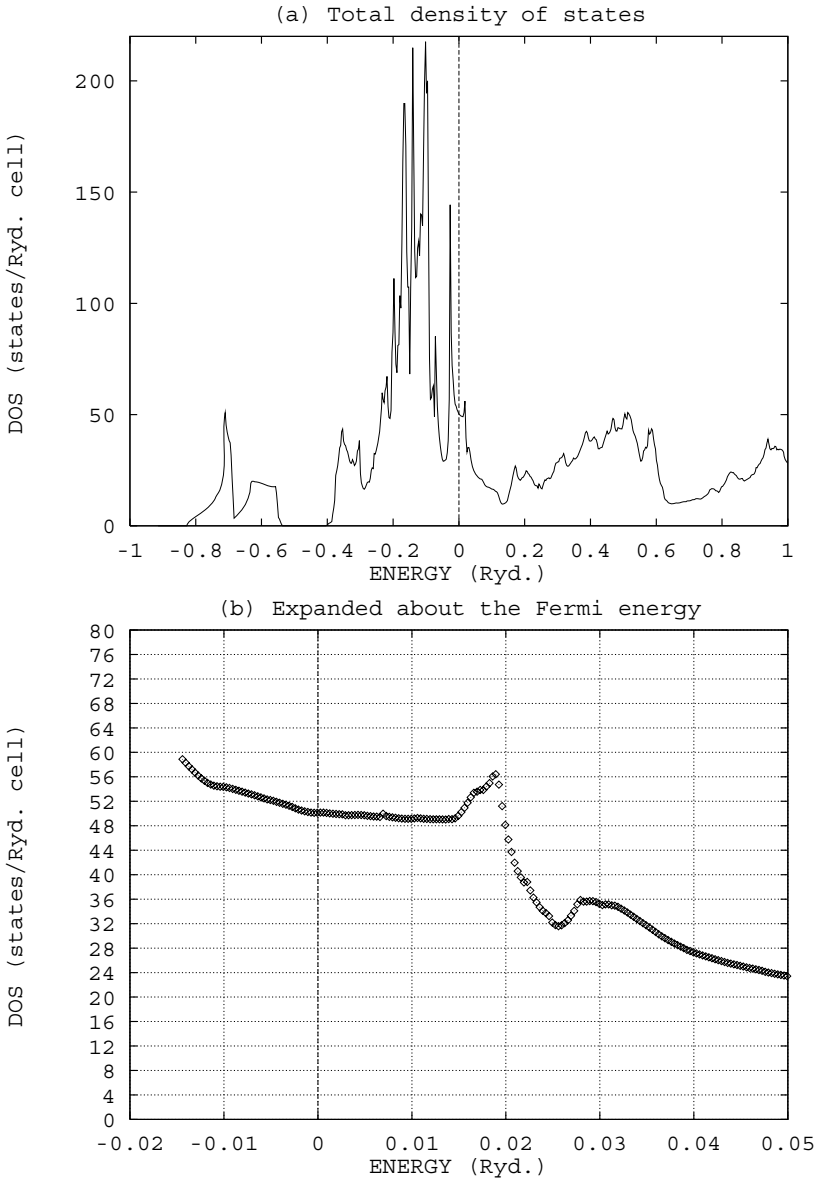

Figure 5.10 Density of states (DOS) for $EuNi_2Ge_2$. Energy is plotted relative to the Fermi level (obtained from the LMTO calculations), E_f, at zero. $\chi_0(\mathbf{q})$ calculations were performed with E_f shifted upward by 10 mRyd to E_f''. (a) The total DOS and (b) blown-up region centered on E_f to facilitate the calculation of energy needed to add electrons.

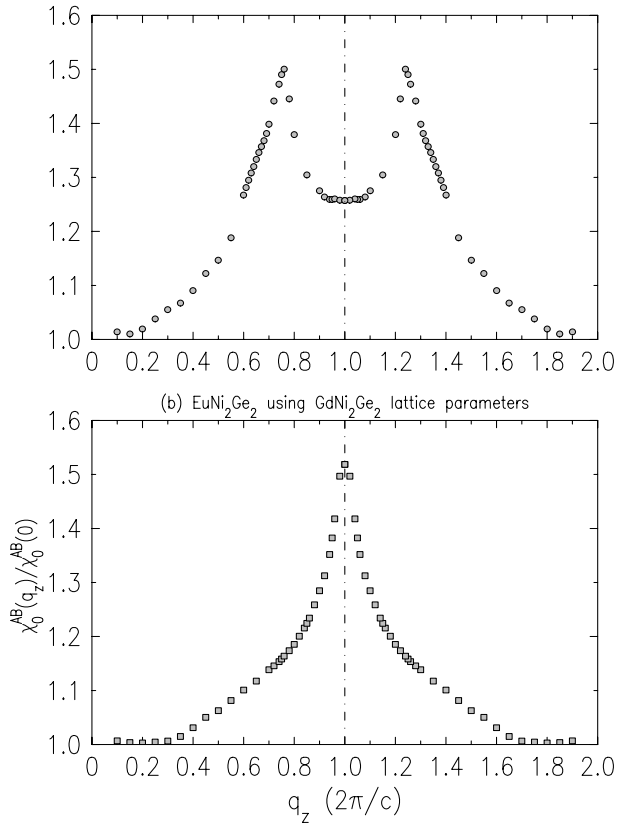

Figure 5.11 Generalized susceptibility with the lattice parameters swapped in order to assess the effects of different lattice constants in $GdNi_2Ge_2$ and $EuNi_2Ge_2$ on nesting.

boundary. These results are in very good agreement with previous findings and show that band filling is clearly the relevant perturbation that determines the maximum to be so different in these two materials. These $\chi_0(\mathbf{q})$ calculations were performed by raising E_f by, 7 and 10 mRyd, as were used for the 'pure' Gd and Eu compounds, respectively. These peaks are also determined by interband (A$\leftrightarrow$B) nesting as was the case with the pure compounds.

Based on the above analysis it can be noted that it may be possible to transform the incommensurate structure observed in $GdNi_2Ge_2$ into the commensurate AF phase found in $EuNi_2Ge_2$ by lowering the band filling. $\chi_0(\mathbf{q})$ calculations were first carried out for $GdNi_2Ge_2$ on removal of electrons by simply lowering E_f' by amounts determined

from the DOS (see Fig. 5.8). Some of the results of these calculations are shown in Fig. 5.12(a). Similarly, electrons were added to $EuNi_2Ge_2$ by raising E_f'' and some of the corresponding $\chi_0(\mathbf{q})$ calculations are shown in Fig. 5.12(b). In the case of $GdNi_2Ge_2$ the peak at 0.79 diminishes in magnitude as it approaches the zone boundary and locks in there as a sharp peak for the case of 'one' less electron. The reverse motion takes place in the case of $EuNi_2Ge_2$. The peak at q_z=1 splits and recedes away from the zone boundary. The magnitude of this peak is also diminished as it moves farther away, reaching 0.78 for the case of 'one' more electron, simulating $GdNi_2Ge_2$. Figure 5.13 shows the ordering vector obtained from the peak in $\chi_0(\mathbf{q})$ calculated by removing electrons from $GdNi_2Ge_2$ as well as by adding electrons to $EuNi_2Ge_2$, as described above. Interestingly, calculated q_z values lie close to the linear interpolation between the experimentally observed modulations of the end members. Future experiments with XRES on $Gd_{1-x}Eu_xNi_2Ge_2$ pseudoternary alloys are needed to explore these predictions and to determine at which finite Gd content a locking to (0 0 1) will occur.

Finally, it has been noted at the beginning of this chapter that $EuNi_2Ge_2$ has a higher T_N compared to that of $GdNi_2Ge_2$. This is surprising, since atomic calculations showed [91] the $4f$-$5d$ exchange integral in Eu to be only 73% of that of Gd. This apparently anomalous behavior may have its origin in the complicated electronic structure of these complex structures that was alluded to earlier. In general, T_N, scales with the product $\langle I \rangle^2 \chi_0(\mathbf{q})$. Since the Néel transition is driven by interband (A$\leftrightarrow$B) nesting, one can estimate the interband (A$\leftrightarrow$B) exchange matrix element, $\langle I_{\rm AB} \rangle$, by considering the product $\mid C_{5d}^{\rm A}(\mathbf{k}) \mid \cdot \mid C_{5d}^{\rm B}(\mathbf{k}+\mathbf{q}_{nest}) \mid$ where C_{5d} is the amount of $5d$ character of a band electron. It is found that on the average, $\frac{\langle I_{\rm AB}({\rm EuNi_2Ge_2})\rangle^2}{\langle I_{\rm AB}({\rm GdNi_2Ge_2})\rangle^2} \sim 1.3$. Also, $\chi_0^{\rm AB}(\mathbf{q}_{Eu})$ and $\chi_0^{\rm AB}(\mathbf{q}_{Gd})$ are 29.35 and 23.69 (states/(Ryd-cell)), respectively. Therefore, it can be argued that T_N in $EuNi_2Ge_2$ is higher due to larger values of these two quantities.

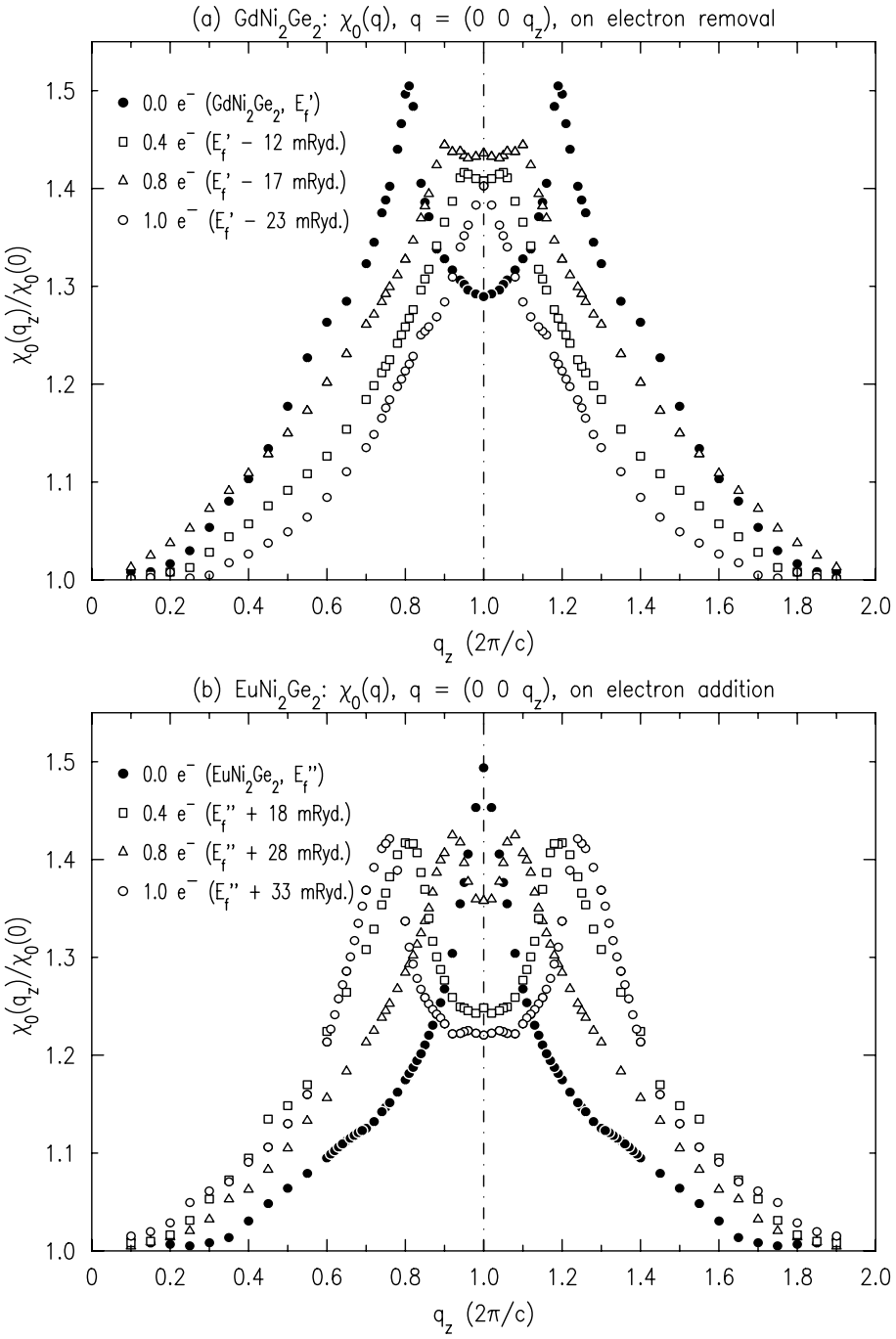

Figure 5.12 Effects of band filling on generalized susceptibility. See text for details.

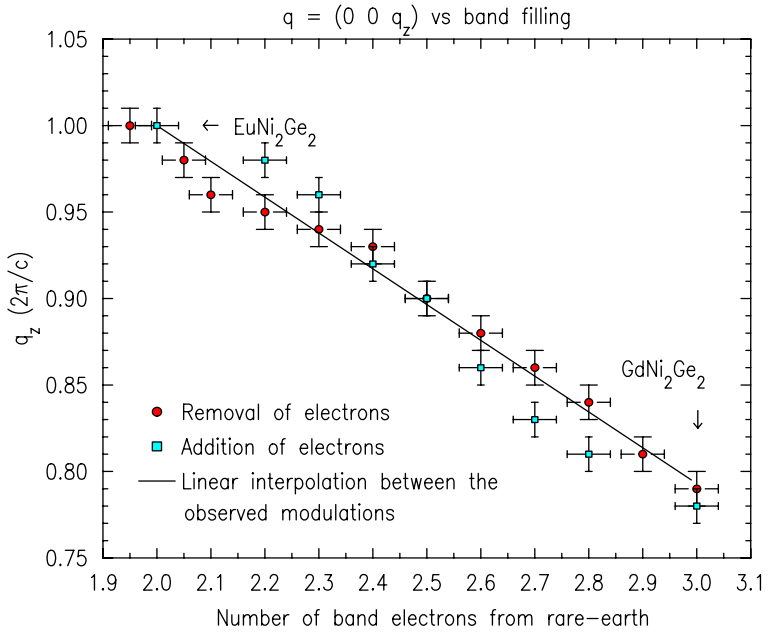

Figure 5.13 Predicted modulation vectors obtained from the peak position of $\chi_0(\mathbf{q})$ as a function of band filling.

Determination of Moment Directions using XRES

It has been established above that both the incommensurate ordering wave vector, (0 0 0.793), in $GdNi_2Ge_2$ and the commensurate modulation, (0 0 1), in $EuNi_2Ge_2$ are determined by strong Fermi surface nesting. However, the details of the magnetic structures remained unspecified. As was mentioned earlier, XRES techniques are ideal to study these compounds since they are neutron opaque. This section is concerned with unraveling the details of these ordered states, which is a primary experimental focus of this dissertation.

In order to determine the moment direction below T_t, the integrated intensities of a series of magnetic satellites in both materials were measured. The results of such measurements along with the model calculations are shown in Fig. 5.14(a) and (b). This figure also illustrates the differences in the **Q**-dependence of the intensities that arise from different normalization schemes. For $EuNi_2Ge_2$ the data have been normalized by

monitor, whereas for $GdNi_2Ge_2$, fluorescence yields have been used. In both cases the model with the ordered moments in the basal plane describes the trend very well, whereas the model with moments along the $\hat{\mathbf{c}}$ axis produces a $\mathbf{Q}$-dependence that is manifestly in disagreement with the data. It is noted that due to experimental uncertainties the ordered moment direction can only be determined within $\sim 10^\circ$ of the basal plane. This result is consistent with the hypothesis of the easy plane of magnetization derived from the anisotropic $\chi(T)$ measurements presented at the beginning of this chapter. However, the fact that the ordered moments are locked to the basal plane is in disagreement with earlier Mössbauer measurements of the hyperfine fields which concluded that the moments are at 44° from the $\hat{\mathbf{c}}$ axis[37].

In order to understand the ordered structure above T_t but below T_N the integrated intensities of the magnetic satellites were also measured as a function of temperature. In the case of $EuNi_2Ge_2$ the integrated intensity decreases monotonically as temperature increases and reaches zero at T_N, which is approximated to be 31 ± 0.3 K (Fig. 5.14(c)). On the other hand, the integrated intensity for $GdNi_2Ge_2$ starts to decrease monotonically and then deviates from this behavior above T_t with a pronounced break at T_t' and goes to zero at T_N of 26.9 ± 0.2 K (Fig. 5.14(d)). The deviation above T_t from a nearly linear decrease with increasing temperature, as was the case in $EuNi_2Ge_2$, is significant and can be interpreted as due to the development above T_t of an ordered-moment component along the $\hat{\mathbf{c}}$ axis in $GdNi_2Ge_2$. This can be seen by considering the XRES cross-section for the $E1$ resonance which is proportional to $\sum |\hat{k}' \cdot \hat{n}_i|^2$, where the summation is over all the domains with moment direction $\hat{n}_i$ and $\hat{k}'$ is the direction of the scattered beam. Therefore, the cross-section is clearly invariant if the moments simply reorient in the tetragonal basal planes, due to the four-fold symmetry of these planes whereas an ordered component along the $\hat{\mathbf{c}}$ axis would give additional scattering, increasing the intensity. In the case of $EuNi_2Ge_2$ above T_t, however, the ordered moments remain locked to but reorient themselves in the basal plane. Thus, no break in

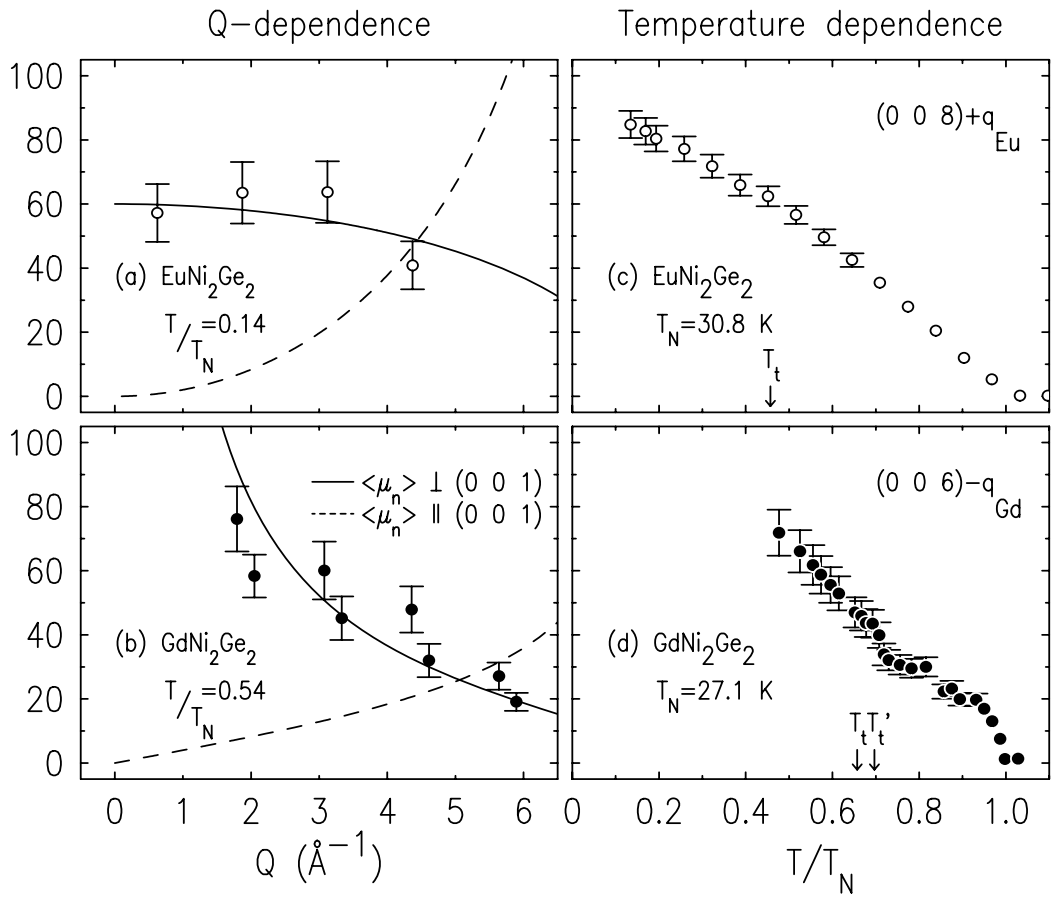

Figure 5.14 The **Q**-dependence of the integrated intensities of the magnetic satellites for (a) $EuNi_2Ge_2$ and (b) $GdNi_2Ge_2$. The solid line is for a model with the ordered moments in the tetragonal basal plane whereas the dashed line is for a model with moments along the $\hat{\mathbf{c}}$ axis. Data in (a) was normalized by the monitor and that in (b) was normalized by the fluorescence yields. The integrated intensity of a magnetic Bragg peak for (c) $EuNi_2Ge_2$ and for (d) $GdNi_2Ge_2$ as a function of temperature.

intensity above T_t is expected and subsequently the intensity decreases monotonically as observed (Fig. 5.14(c)). A subtle transition involving spin reorientations has been found in $GdNi_2B_2C$ system, where non-resonant magnetic scattering, in conjunction with the XRES, was utilized to determine the structure [67]. In the present case, unfortunately, the non-resonant scattering above the background was small, making its use impractical.

Summary

In this chapter it has been established that the wave vector at the onset of the Néel transition for the $R Ni_2Ge_2$ family of compounds is determined by strong Fermi surface nesting with $\mathbf{q}_{nest}$ that determines the initial ordering wave vector as observed across the series. This is the most important theoretical result of this work. Furthermore, it was argued that the unexpected higher ordering temperature in the Eu member of the series is due to changes in the orbital character of the conduction electron states near the nesting region of the Fermi surface.

Next, the effects of band filling on ordered state have been presented. $\chi_0(\mathbf{q})$ calculations predicted a continuous transition from the incommensurate structure as observed in $GdNi_2Ge_2$ to the commensurate structure of $EuNi_2Ge_2$ via band filling. Experimentally, such transformations could manifest in the pseudoternary alloys, $Gd_{1-x}Eu_xNi_2Ge_2$, which can be conveniently and accurately studied by XRES.

Finally, the magnetic structures of $EuNi_2Ge_2$ and $GdNi_2Ge_2$ have been determined by XRES. The magnetic structures of $EuNi_2Ge_2$ are simple AF with the moments locked to the basal plane in both the phases. These structures are composed of ferromagnetic basal planes antiferromagnetically coupled along the $\hat{\mathbf{c}}$ axis with a simple sequence of '+-+-' where a '+' indicates the moment direction in the plane, presumably a high symmetry one such as [1 0 0] or [1 1 0]. At T_t, a spin reorientation in the basal plane takes place. The direction within the plane, however, could not be determined due to the presence

of four equivalent domains associated with the four directions in the basal plane. In the case of $GdNi_2Ge_2$ the ordered structures are incommensurate in both the phases. Although the ordered components are locked to the basal plane below T_t, the direction of ordered moments is at an angle, β, away from $\hat{\mathbf{c}}$ due to the development of an additional component along this axis. This structure bears similarity with that in $DyNi_2Ge_2$ above T_t. β in $GdNi_2Ge_2$ is, however, not known. As in $EuNi_2Ge_2$, the direction of the in-plane ordered component could not be specified, leaving the possibility of a conical antiferromagnet open. Future experiments such as those suggested for $DyNi_2Ge_2$ may be useful for further studies of these structures.

6 METAMAGNETISM IN $TbNi_2Ge_2$

In the previous chapters magnetically ordered ground states of the Eu, Gd, Tb and Dy nickel germanides have been studied in detail in the absence of any applied magnetic fields, and the primary factor in determining the ordering wave vector was shown to be Fermi surface nesting. The study of the Eu and Gd pair of compounds showed how the nature of magnetic ordering is systematically altered due to band filling that dramatically influences the RKKY interactions and nesting. In the case of anisotropic systems, such as the Tb and Dy compounds, the configuration of the ground state is determined by the compromise between the long-range RKKY exchange and the single-ion CEF anisotropy, *i.e.* $\mathcal{H}_{\rm RKKY}$ and $\mathcal{H}_{\rm CEF}$, respectively. In this chapter the effects of an external magnetic field, *i.e* $\mathcal{H}_{\rm Zee}$, on magnetic structure at low temperature are studied. As is well-known, at sufficiently high fields the saturated paramagnetic state can be reached. However, at intermediate fields a material may or may not go through a series of metamagnetic transitions which can involve very intricately ordered phases, depending on the direction of the applied field [5, 100, 77]. Field-induced structures like these were termed 'metamagnetic' by Kramers when they were first observed, since the conventional theory of ferromagnetism or Néel antiferromagnetism afforded no explanation for such behavior [101]. As was already mentioned before, perhaps the most interesting member of this series from the point of view of metamagnetism is $TbNi_2Ge_2$, which is the focus of this chapter.

When a field is applied in the basal plane of $TbNi_2Ge_2$, the magnetization does not exhibit any transition for H<55 kG. However, as the field applied along the $\hat{\mathbf{c}}$ axis

increases from zero, a sequence of well-defined steps in the magnetization appears (see Fig. 6.1) for 2.0 K. Five distinct transitions below 55 kG are observed at 14 kG, 18.1 kG, 29 kG, 35 kG, and 45.8 kG, respectively. The sequence of magnetization values in the metamagnetic phases is approximately $\frac{1}{8}$, $\frac{1}{5}$, $\frac{3}{10}$, $\frac{1}{2}$ and $\frac{3}{5}$ of the saturation value of 9.0 μ_B. The transition into the saturated paramagnetic phase occurs at 59 kG with 9.0 μ_B per Tb^{3+} which persists up to the maximum attainable field of 180 kG [23]. Also, M($\mathbf{H} \parallel \mathbf{c}$) is hysteretic and on field ramping down from the maximum value there are two more states [23], giving nine well-defined phases. Thus, as was mentioned earlier, the clarity of these transitions and the number of phases make this material an archetypal system to study axial metamagnetism. The $H-T$ phase diagram for $TbNi_2Ge_2$ is shown in Fig. 6.2. An inspection of this figure reveals the richness of the phase diagram with clearly defined phase boundaries. This phase diagram suggests the existence of several critical points where two or more phases coexist. As mentioned earlier, a primary focus of this work is on the zero field and the "zero" temperature (1.4 K) boundary of this complex phase diagram. The zero field structures have been studied in detail and presented in Chap. 3. This chapter is concerned with the study of the low temperature metamagnetic phases.

Among some of the salient features of M($\mathbf{H}$) is the rather small range of existence of some phases such as I and III compared to those of the other phases. These two phases are very sensitive to temperature and are the first ones to disappear at $\sim$5 K [23]. Secondly, compared to the nearly zero slope in the EM phase and phase V, the magnetization has a larger nonzero slope in the intermediate phases, that in phase IV being the largest. In addition, the slopes, as well as the widths, of all the transition regions are different from each other. Such differences in the slopes of the metamagnetic phases have recently been reported in the isostructural $TbRu_2Ge_2$ compounds [102, 103]. In this system, a fraction of the Tb ions are found in a *nonmagnetic* state while the remaining ones retain the full saturation value. This is an example of "mixed phase,"

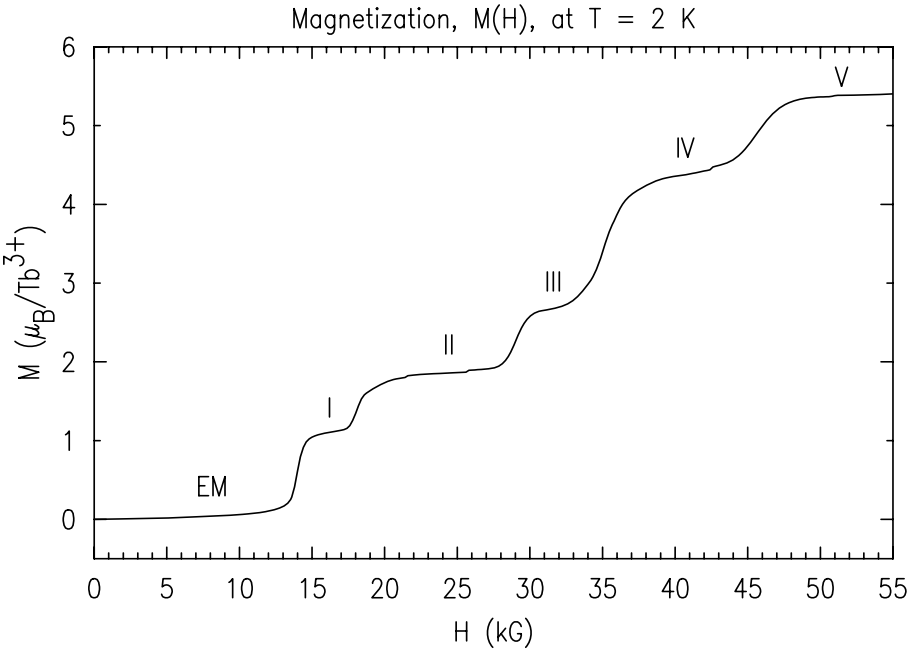

Figure 6.1 Low temperature magnetization of $TbNi_2Ge_2$ as a function of field along the $\hat{\mathbf{c}}$ axis.

for ions of two different magnetic states are present. According to Refs. [102, 103] the mechanism for the existence of such nonmagnetic ions is the crossing of the ground state singlet (or state with weak moment) by a higher CEF level with large moment. The number of the nonmagnetic ions in a particular phase determines the slope of M($\mathbf{H}$) for that phase, since their magnetization is sensitive to magnetic field. It was suggested that the slope of M($\mathbf{H}$) in a metamagnetic region can be used to infer the nature, 'mixed' or 'pure,' of that particular phase as well as the number of nonmagnetic ions present therein [102, 103]. In the case of $TbNi_2Ge_2$ one then might expect to see mixed phases in several of the I-IV metamagnetic structures. However, the validity of the suggestion that the number of nonmagnetic ions can be obtained from the slope of M($\mathbf{H}$) in the metamagnetic phase depends on the constancy of the magnetic periodicity which is true for $TbRu_2Ge_2$ [102, 103]. This is not the case for $TbNi_2Ge_2$, as will be shown later in this chapter.

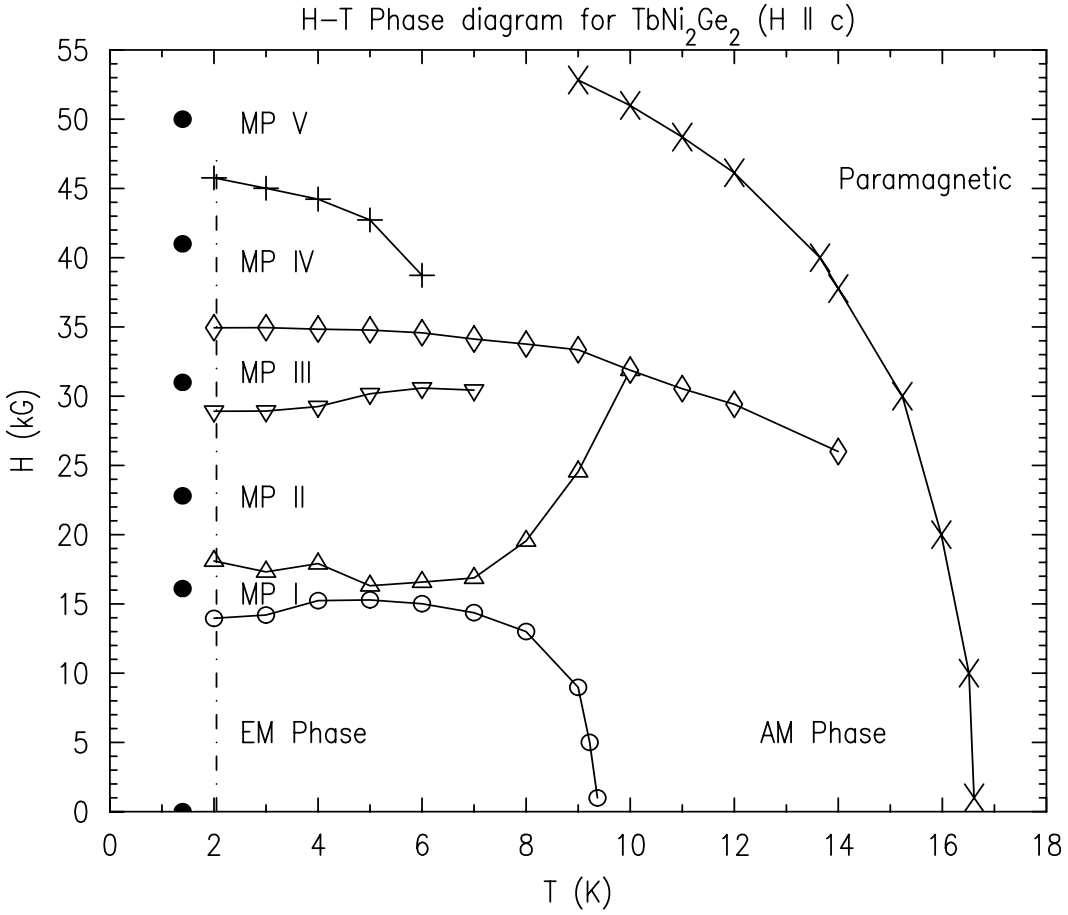

Figure 6.2 $H - T$ phase diagram for $TbNi_2Ge_2$ with the applied field along the $\hat{\mathbf{c}}$ axis [23]. This phase diagram was obtained on increasing the magnetic field. The solid circles indicate field and temperature values for all the phases at which detailed neutron diffraction studies were performed. Detailed field-depenence of certain magnetic peaks was measured along the vertical dotted-dashed line at 2.1 K. Solid lines are drawn as a guide to the eye.

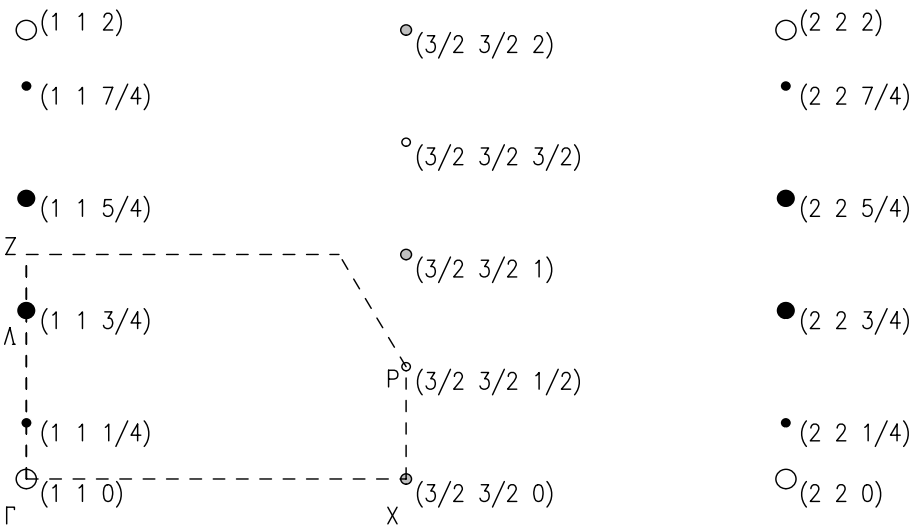

Figure 6.3 A section of the $[h\ h\ l]$ zone of reciprocal space of $TbNi_2Ge_2$ below T_t showing the relative positions of the nuclear and the superlattice peaks, respectively. The big (small) bullets are $\boldsymbol{\tau}_1$ ($\boldsymbol{\tau}_1'$) peaks. Small shaded (open) circles represent $\boldsymbol{\tau}_2$ ($\boldsymbol{\tau}_3$) satellites. Nuclear reflections are shown by big open circles. The relative sizes indicate approximately the relative strengths of these reflections without regard to form factor effects. The polygon outlined by dashed lines is the irreducible section of this zone.

Zero-Field EM Structure of $TbNi_2Ge_2$

In the absence of external fields below T_t the EM structure of $TbNi_2Ge_2$ is described by a set of three wave vectors, namely, $\boldsymbol{\tau}_1$=(0 0 $\frac{3}{4}$), along with its third harmonic $\boldsymbol{\tau}_1'$=(0 0 $\frac{1}{4}$), $\boldsymbol{\tau}_2$=($\frac{1}{2}$ $\frac{1}{2}$ 0) and $\boldsymbol{\tau}_3$=($\frac{1}{2}$ $\frac{1}{2}$ $\frac{1}{2}$), respectively. A section of the $[h\ h\ l]$ zone of reciprocal space displayed in Fig. 6.3 shows the relative positions of various superlattice peaks associated with these modulations. The presence of the third harmonic is due to the squared-up nature of this phase with saturated 9.0 μ_B at all Tb sites. The magnetic unit cell of this structure is reproduced in Fig. 6.4 for easier reference. The existence of the AF planes (#3 and #7) gives rise to the $\boldsymbol{\tau}_2$ and $\boldsymbol{\tau}_3$ modulations. The direction of the ordered moments is along the $\hat{\mathbf{c}}$ axis as shown in Fig. 6.4.

In order to understand what the metamagnetic transitions observed in M($\mathbf{H}$) may

entail microscopically, a simple scenario of such transitions can be created. Let a set of ionic moments (μ_{ion}) be fixed in magnitude ("rigid"), which can happen when the ions are subjected to a large molecular field so that their ground state is completely polarized. Let these ions be locked into the easy axis of magnetization (*e.g.* $\hat{\mathbf{c}}$ axis in the tetragonal or hexagonal systems) due to CEF anisotropy. Now, an ordered state of these ionic moments corresponds to a definite sequence such as $\uparrow\downarrow\uparrow\downarrow$ (where $\uparrow$ ($\downarrow$) indicates a moment parallel (antiparallel) to the $\hat{\mathbf{c}}$ axis) in the case of a simple AF ordering due to their mutual exchange interactions. When an external field applied along the $\hat{\mathbf{c}}$ axis becomes larger than some critical field corresponding to an exchange coupling between pairs of ions (such as those with nearest and next-nearest neighbors) a *spin-flip* ($\downarrow$ to $\uparrow$, SF) transition takes place. Thus, the magnetization proceeds in steps with a jump of $\left(\frac{2n}{N}\right)\mu_{ion}$ per ion where n is the number of ions flipped and N is the total number of ions. This process can continue until the induced ferromagnetic (F) state is obtained. Metamagnetic transitions via SF mechanism are observed in various systems such as $DyCo_2Si_2$ [104] where the individual Dy moments retain their full saturation value in all the phases.

Now consider the case of $TbNi_2Ge_2$. According to the SF picture, one might expect the AF planes (such as #3 and #7 in Fig. 6.4) in $TbNi_2Ge_2$ to become F in an external field along the $\hat{\mathbf{c}}$ axis since they are seemingly the most weakly coupled to the rest of the EM structure. Thus, the first two metamagnetic phase transitions may correspond to SFs at these two planes with concomitant disappearance of the $\boldsymbol{\tau}_3$ and $\boldsymbol{\tau}_2$ superlattice peaks, respectively. As the field is increased further, the F planes (such as #1, #4 and #6 in Fig. 6.4) antiparallel to the field will subsequently be flipped. However, this sequence of processes gives a maximum of five transitions whereas six are observed. Also, the magnetic periodicity along the $\hat{\mathbf{c}}$ axis is predicted to remain unaltered throughout. As shown below, neutron diffraction measurements found metamagnetism in $TbNi_2Ge_2$ to be much more complex than the simple picture just presented.

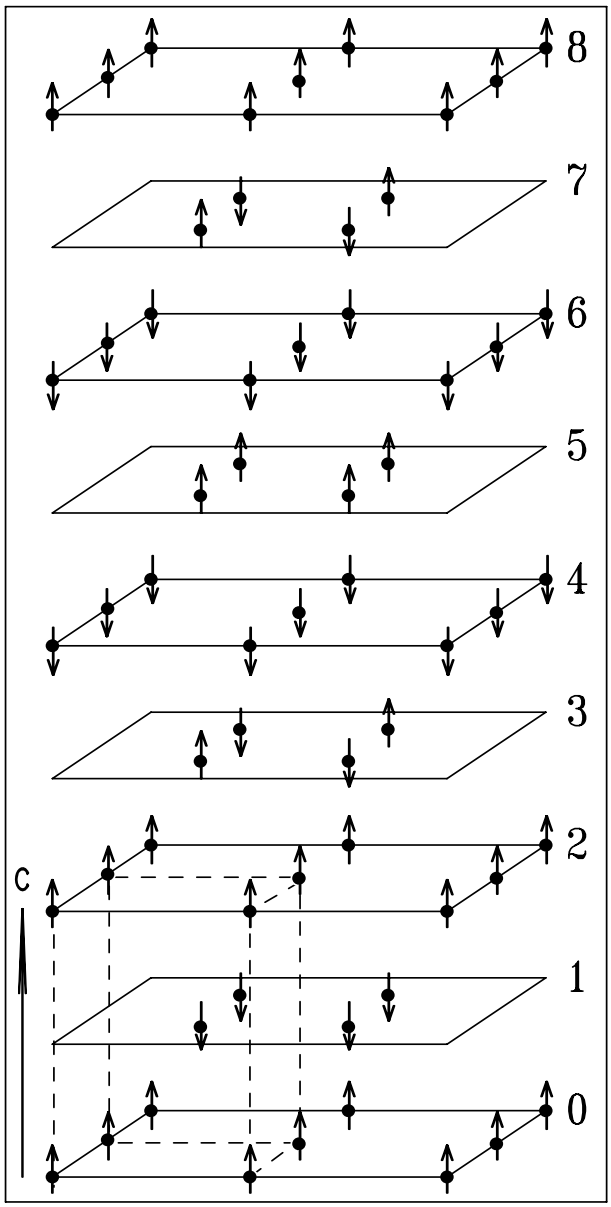

Figure 6.4 Zero-field EM structure of $TbNi_2Ge_2$, reproduced for easier reference. Dashed lines encompass chemical unit cell with two formula units. Ni and Ge atoms are not shown.

Metamagnetic Structures of $TbNi_2Ge_2$

Neutron diffraction measurements to study the metamagnetic phases were primarily carried out on the thermal-neutron normal-beam diffractometer (D15) at the Institute Laue-Langevin (ILL). Neutrons with wavelength of 1.17 Å were selected using a Cu (331) monochromator. Since the $\frac{\lambda}{2}$ contamination was only $\sim$0.1% no filters were used. A small (36 mg) single crystal with the $\hat{\mathbf{c}}$ axis perpendicular to the horizontal plane was carefully mounted inside a 6 T vertical magnet. Magnetic peaks corresponding to $\boldsymbol{\tau}_1$ modulation were observed by moving the detector above and below the equatorial plane, albeit with degraded **Q**-resolution. The width (HWHM) of Bragg peak l-scans was $\sim$0.035 r.l.u. Fortunately, the availability of a horizontal field magnet (an Oxford pumped He cryomagnet) at the Chalk River Laboratory allowed the $[h\ h\ l]$ zone to be aligned in the the equatorial plane which gave a HWHM of $\sim$0.01 r.l.u. for the l-scans. However, since the maximum attainable field was 28.5 kG only the first two metamagnetic phases were accessible. These measurements were performed on the C5 polarized-beam triple-axis spectrometer. Neutrons with wavelength 2.36 Å were used and a PG filter after the sample was placed.

Summary of Neutron Diffraction Measurements

Metamagnetic phases were observed at 16.1 kG, 22.8 kG, 31.0 kG, 41.0 kG and 51.0 kG, respectively (see Fig. 6.2). There are two scans that contain the essential information of all of the metamagnetic structures studied. These are ($\frac{3}{2}$ $\frac{3}{2}$ l) and (-1 1 l) scans, respectively, as can be seen by an inspection of Fig. 6.3. These scans for all the metamagnetic phases at 1.4 K are displayed in in Fig 6.5 and 6.6 The bottom panel in each shows the corresponding zero-field (EM phase) scans for comparison. The first surprising result of these measurements is that both $\boldsymbol{\tau}_2$ and $\boldsymbol{\tau}_3$ peaks persist in *all* the phases indicating the presence of the AF planes. In fact, these peaks remain unaffected,

within experimental accuracy, in metamagnetic phase I (compare Fig. 6.5(a) and (b)) contrary to the naive expectations presented above. This observation was reconfirmed during the Chalk River experiment with higher resolution. In addition, the position of the $\boldsymbol{\tau}_1$ satellite is shifted in the III-IV phases relative to that in the EM phase. Since the nuclear peaks remain fixed in position within experimental uncertainties, this implies a change in periodicity of the magnetic structures. Thus, the metamagnetic transitions in $TbNi_2Ge_2$ are much more complex. In general, the intensity of the (-1 1 0) nuclear peak grows in successive phases due to increasing ferromagnetic contributions as the field is ramped up. On the other hand, the $\boldsymbol{\tau}_1$ satellite grows weaker as antiferromagnetism is destroyed. Also, as stated above, the l-scans of the nuclear peaks remain fixed in position indicating that there is no distortion of the c lattice parameter within experimental accuracy. Below, the experimental observations in each metamagnetic phase (MP) are summarized.

MP I (Fig. 6.5(b) and 6.6(b)) As already mentioned $\boldsymbol{\tau}_2$ and $\boldsymbol{\tau}_3$ peaks remain unaffected in this phase. The disappearance of $\boldsymbol{\tau}_1'$ suggests a moment modulation as is the case in the zero field structure above T_t. Interestingly, a new peak $\boldsymbol{\tau}_4 = (0\ 0\ 1)$ appears. Also, very weak combination harmonics, $\boldsymbol{\tau}_1+\boldsymbol{\tau}_2$, are found to emerge.

MP II (Fig. 6.5(c) and 6.6(c)) In this phase both $\boldsymbol{\tau}_2$ and $\boldsymbol{\tau}_3$ are significantly affected. Their intensities are reduced and the widths are increased. This is more dramatic for the $\boldsymbol{\tau}_3$ satellites. This broadening beyond the instrumental resolution indicates unresolved peaks close to these satellites. Using better resolution at the Chalk River Laboratory these peaks have been resolved and the corresponding scan is shown in Fig. 6.7. The $\boldsymbol{\tau}_2$ peak is flanked on both sides by weak $\boldsymbol{\tau}_1+\boldsymbol{\tau}_2$ second-order combination harmonics, whereas stronger combination third harmonics, $2\boldsymbol{\tau}_1+\boldsymbol{\tau}_2$, grow as wings beside the $\boldsymbol{\tau}_3$ satellites. In addition, $\boldsymbol{\tau}_1$ shifts to (0 0 $\sim$0.79), indicating a change in magnetic periodicity in the $\hat{\mathbf{c}}$ direction. Furthermore, the third harmonic $\boldsymbol{\tau}_1'$ reappears, which implies a re-squaring-up of the structure as is the case in the EM phase. Also, the $\boldsymbol{\tau}_4$ modulation

which was present in MP I is no longer observed.

MP III (Fig. 6.5(d) and 6.6(d)) This phase distinguishes itself from MP II with a twofold increase in the intensity of the combination harmonics, as evidenced by the growth of the unresolved peaks at $\boldsymbol{\tau}_3$ satellite positions and a decrease of the $\boldsymbol{\tau}_2$ satellite intensity. As in MP I, the third harmonic $\boldsymbol{\tau}_1'$ disappears, suggesting a possible moment modulation.

MP IV (Fig. 6.5(e) and 6.6(e)) One characteristic feature of this phase is that only the second-order combination harmonics, $\boldsymbol{\tau}_1+\boldsymbol{\tau}_2$, are present. These peaks are well resolved from $\boldsymbol{\tau}_2$ and $\boldsymbol{\tau}_3$ satellites due to the shift of $\boldsymbol{\tau}_1$ back towards its EM phase value of $(0\ 0\ \frac{3}{4})$ (see Fig. 6.8). Wheras the intensities of $\boldsymbol{\tau}_1+\boldsymbol{\tau}_2$ and $\boldsymbol{\tau}_3$ decrease that of $\boldsymbol{\tau}_2$ grows compared to its magnitude in MP III. In addition, a barely discernible $\boldsymbol{\tau}_1'$ peak reappears in this phase.

MP V[1] (Fig. 6.5(f) and 6.6(f)) In this last MP before the transition to the saturated paramagnetic state a weak second harmonic of $\boldsymbol{\tau}_1$ appears for the first time. An interesting feature in this phase is that compared to those in MP IV the intensity of $\boldsymbol{\tau}_2$ decreases whereas that of $\boldsymbol{\tau}_3$ grows and becomes larger than that of $\boldsymbol{\tau}_2$. This may be due to contributions from the same features that give rise to $2\boldsymbol{\tau}_1$ satellites in this phase. As in MP IV, only $\boldsymbol{\tau}_1+\boldsymbol{\tau}_2$ satellites are present. However, $\boldsymbol{\tau}_1'$ has disappeared.

In order to understand better the nature of the metamagnetic structures, in particular the change in magnetic periodicity, a detailed magnetic field dependence of the $\boldsymbol{\tau}_1$ satellite was measured (along the vertical dotted-dashed line in Fig. 6.2). Due to severe peak overlaps, $\boldsymbol{\tau}_2$, $\boldsymbol{\tau}_3$ and the combination harmonics could not be measured accurately. In order to measure the periodicity as accurately as possible the **Q**-resolution was improved by placing narrower slits right before the detector. The HWHM of Bragg peak

[1]It is noted that at this field there were considerable temperature fluctuations up to 3 K caused by pumping on the magnet. So, the measurements in this phase may be less reliable. Nevertheless, the results are summarized here for completeness.

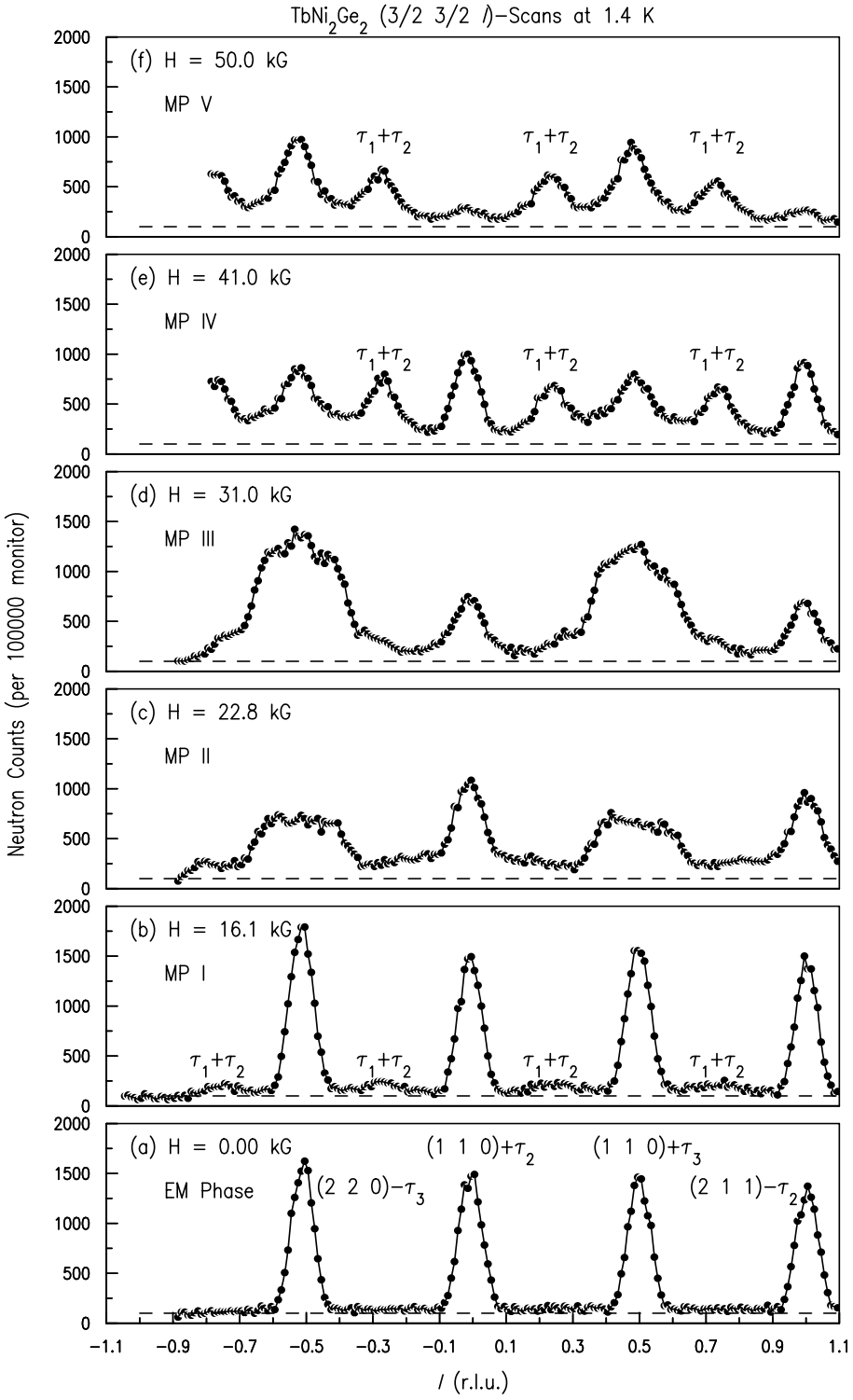

Figure 6.5 $(\frac{3}{2}\ \frac{3}{2}\ l)$-scans in all the metamagnetic phases. Data were taken on D15 beamline at ILL. See text for details.

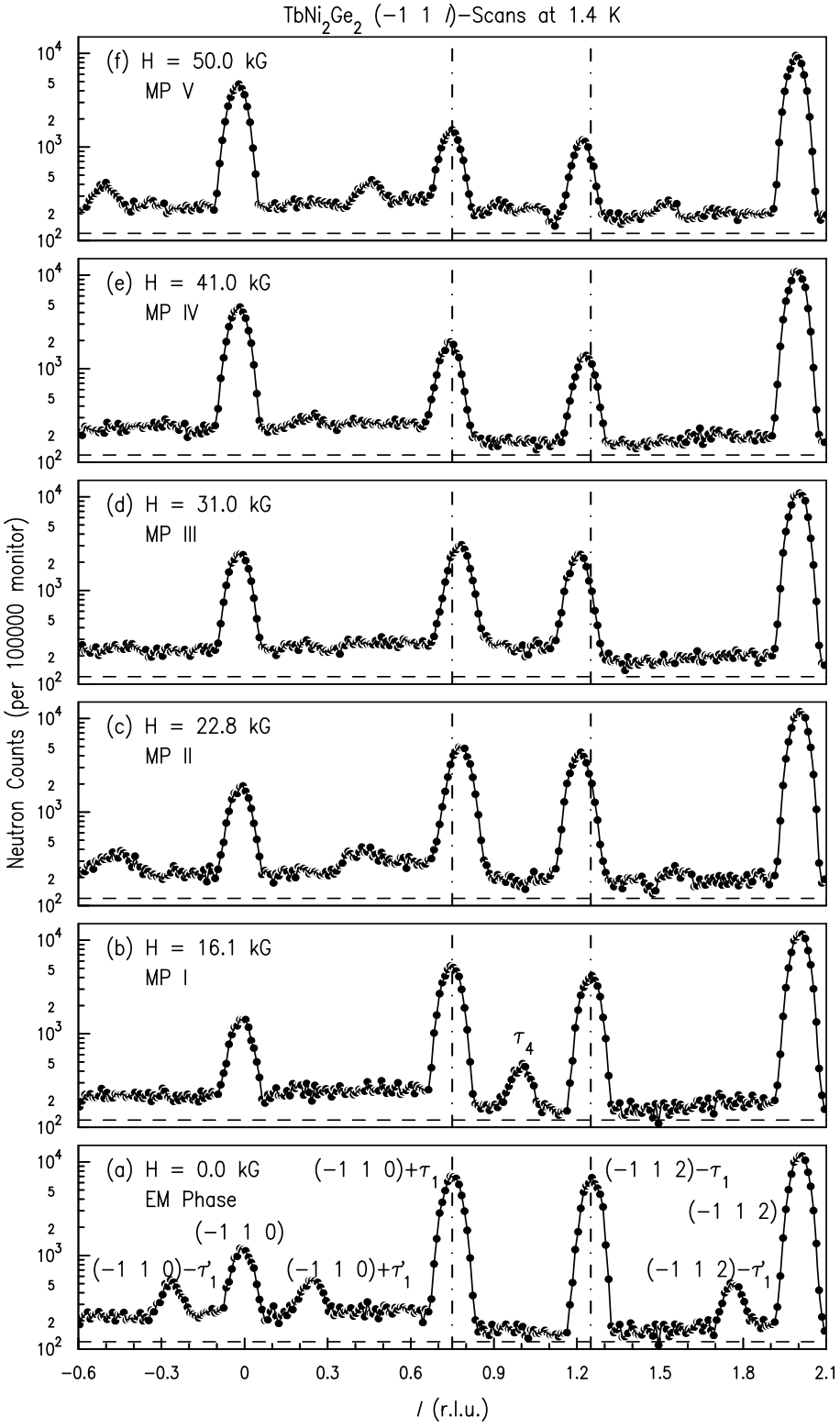

Figure 6.6 (-1 1 l)-scans in all the metamagnetic phases. Data were taken on D15 beamline at ILL. See text for details.

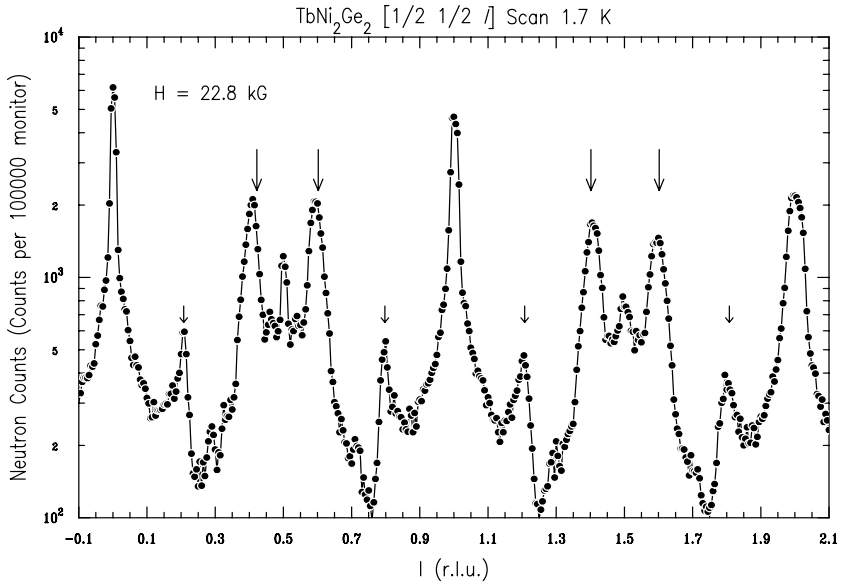

Figure 6.7 $(\frac{1}{2}\ \frac{1}{2}\ l)$-scan with a better **Q**-resolution at Chalk River Laboratory. The large (small) arrows indicate the $2\boldsymbol{\tau}_1+\boldsymbol{\tau}_2$ ($\boldsymbol{\tau}_1+\boldsymbol{\tau}_2$) satellites.

l-scans reduced to $\sim$0.023 r.l.u.[2] Figure 6.8 shows the results of such measurements. The position of $\boldsymbol{\tau}_1$ in MP I is essentially (0 0 $\frac{3}{4}$) as in the EM phase. As MP II is approached, $\boldsymbol{\tau}_1$ jumps to (0 0 $\sim$0.79) and stays unchanged within experimental accuracy in this phase. At the onset of MP III, it starts to change continuously and reaches (0 0 $\frac{3}{4}$) in the middle of MP IV. Within the error bars $\boldsymbol{\tau}_1$ remains fixed at this position all the way into MP V. The changes in the periodicity prevent any *a priori* prediction of the number of nonmagnetic ions present in a metamagnetic phase based upon M(**H**), as was mentioned above. The bottom panel in Fig. 6.8 shows the width of the $\boldsymbol{\tau}_1$ satellite as a function of field. The dashed line indicates the instrumental resolution, taken to be the nuclear peak width. The width in MP I is the same as that in the EM phase. On the other hand, it is significantly larger in all the other phases.

It is interesting to note that the excursion of $\boldsymbol{\tau}_1$=(0 0 τ_z) is constrained within the range of (0 0 $\frac{3}{4}$) to (0 0 $\sim$0.79), similar to the case found for the ordering vector across the series in zero field. This suggests a critical role played by the ubiquitous conduction

[2]This resolution was not sufficient to resolve the overlapping peaks shown in Fig. 6.5.

electrons in the metamagnetic phases as well. It has been established earlier that strong Fermi surface nesting determines τ_z for all the members of $R\mathrm{Ni_2Ge_2}$ series. It was also shown that the exact value of τ_z depends on the position of E_f relative to nesting and the entire range of 0.75-0.81 for the nesting vector was found within a small energy window of ± 2.5 mRyd centered on E_f for $\mathrm{GdNi_2Ge_2}$. One may then speculate that perhaps even in the magnetically ordered phases the nesting features survive. Furthermore, in the metamagnetic phases the bands that cross E_f shift relative to each other in such a way that the nesting vector changes, determining the value of τ_z as observed.

The integrated intensity (black circles) of the $\boldsymbol{\tau}_1$ satellite is shown in Fig. 6.9, along with the ferromagnetic component (open circles) which was extracted from the (-1 1 0) nuclear peak by subtracting the corresponding zero-field intensity. This was normalized to the magnetization measurements (solid line) at 25 kG by multiplying by a scale factor, and the agreement between the two is quite good. The discrepancy at high fields is due to increased scattering extinction. As the figure shows the intensity of the magnetic peak changes in steps except in MP I. In this phase the intensity continuously decreases reaching a minimum at $\sim$ 16.1 kG and starts to rise as the transition into MP II is traversed. This may be due to amplitude modulation which has been suggested by the disappearance of the third harmonic, $\boldsymbol{\tau}_1'$, in MP I. This phase has been studied in detail which is presented below.

Metamagnetic Phase I (2.1 K, H=16.1 kG)

In order to completely determine the magnetic structures the integrated intensities are needed. Due to severe peak overlaps no reliable measurements of intensities in MP II through MP V could be done. However, it was possible to do such measurements in MP I. In order to put the intensities on an absolute scale so that the ordered moment values can be obtained, Bragg peak intensities of the known EM phase were compared to the measured ones, giving the experimental scale factor. Some 30 nuclear peaks were also

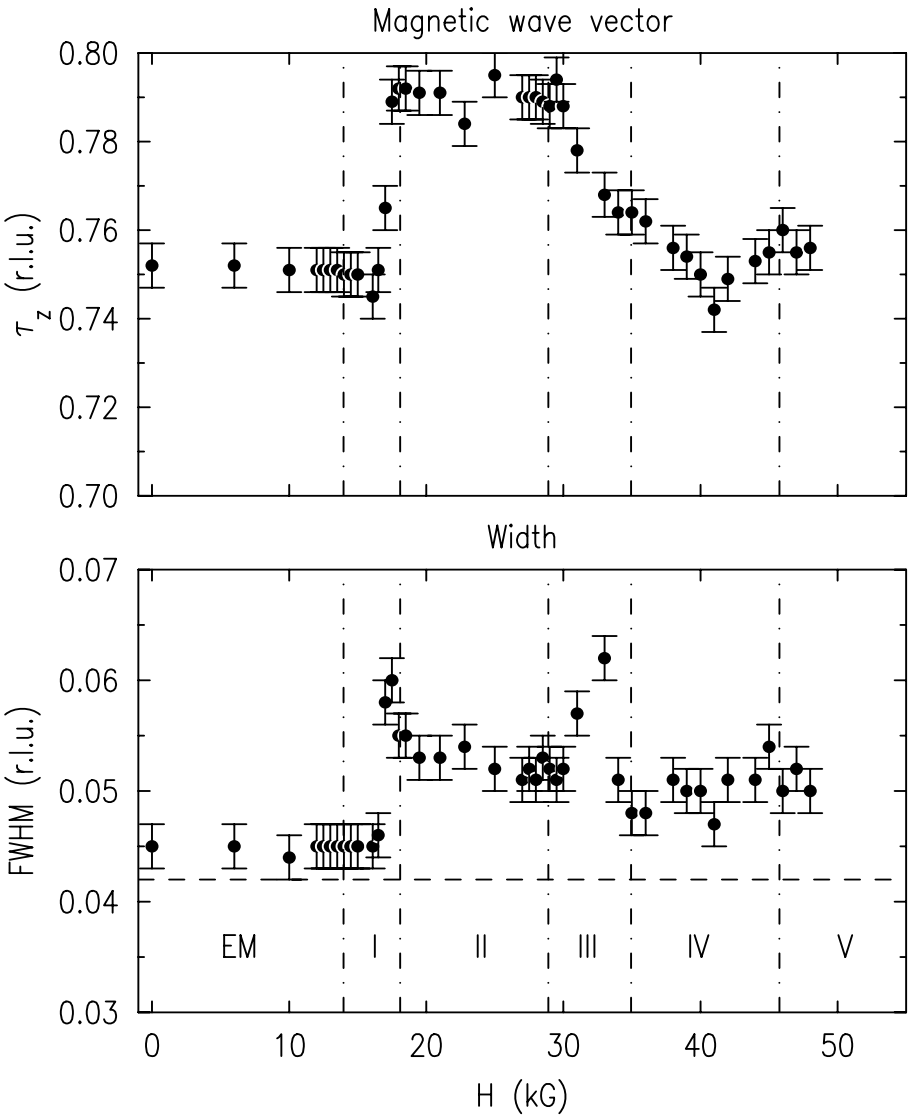

Figure 6.8 Field dependence of the $\boldsymbol{\tau}_1$=(0 0 τ_z) modulation and of its width. Dotted-dashed vertical lines locate the critical fields (see text) as obtained from the maximum derivative of the magnetization curve shown in Fig. 6.1.

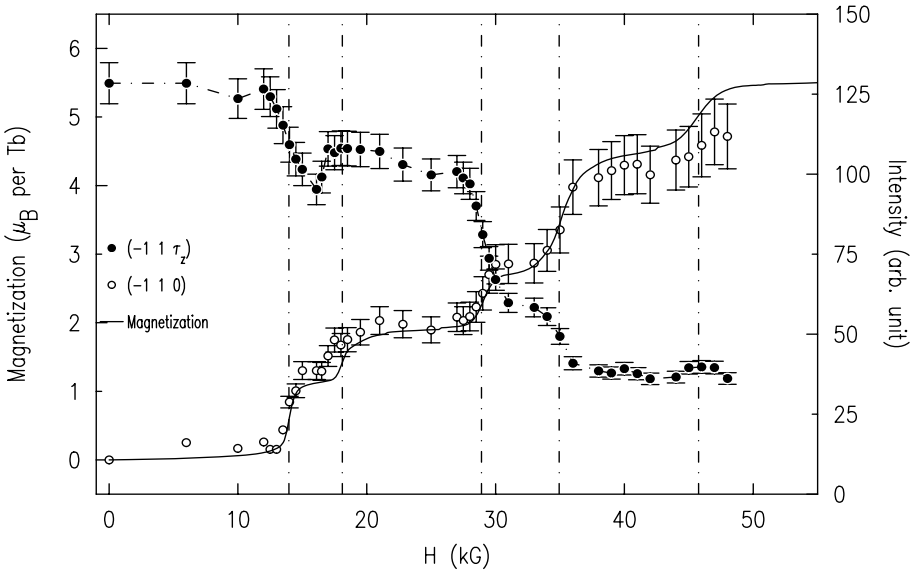

Figure 6.9 Ferromagnetic component and the intensity (scale is on the right) of a $\boldsymbol{\tau}_1$ satellite as a function of field. Note the dip in intensity at 16.1 kG. Solid line shows the bulk magnetization data.

refined to correct for extinction effects. The model structure that has closest agreement with observations is shown in Fig. 6.10. In this model the Tb moments on planes #4 and #6 have a reduced magnitude of 4.6±0.5 μ_B giving a net magnetization of 1.1 μ_B per Tb^{3+} ion, in good agreement with $\frac{9}{8}$ μ_B found in the magnetization measurement. Because of this moment reduction, the triplet consisting of planes #4-6 no longer compensates the lower triplet formed by planes #0-2. This gives rise to the $\boldsymbol{\tau}_4$ peak and also accounts for the disappearance of $\boldsymbol{\tau}_1'$. Since no detectable changes were observed with the $\boldsymbol{\tau}_2$ and $\boldsymbol{\tau}_3$ peaks the AF planes remain unaltered. However, this model does not give the very weak $\boldsymbol{\tau}_1+\boldsymbol{\tau}_2$ combination second harmonics observed since the AF planes are out of phase at this $\mathbf{Q}$. Since these planes do not change in MP I, $\boldsymbol{\tau}_1$ must have changed slightly so that the contributions from the AF planes at $\boldsymbol{\tau}_1+\boldsymbol{\tau}_2$ no longer completely cancel each other. Such a small change of $\boldsymbol{\tau}_1$ is not surprising, since it was found by XRES in the zero-field AM phase above T_t, where $\boldsymbol{\tau}_1 = (0\ 0\ {\sim}0.758)$. MP I is an interesting example of an AM structure induced by an external field. This kind of

field induced behavior is also found in the isostructural $TbNi_2Si_2$ compound where the first metamagnetic phase is AM [26]. In the rest of this chapter a computational study of the cause of such moment modulation is undertaken.

Metamagnetism with "soft" moment

In order to understand qualitatively peculiarities of metamagnetic phases in systems with ionic moments that can vary in magnitude ("soft"), a rather simple model of an R ion with angular momentum $J = 2$ located at a site with point symmetry D_{4h}, as is the case for the R elements in the RNi_2Ge_2 compounds, can be constructed. The primary interests are to explore the ionic response to a *local* magnetic field and to look for an explanation of moment reduction. The value of J above is chosen because it is a non-Kramers system as Tb ($^7F_6$) that can be solved *exactly*. The simpler case of a single-ion $J = 1$ has been treated in Ref. [65]. A mean field treatment of spin ordering in a system of $S = 1$ ions with large uniaxial anisotropy in a magnetic field can be found in Ref [105]. However, in the case of $J = 1$ it is not possible to have a Γ_3 or Γ_4 representation of the D_{4h} point group. In the isostructural $TbNi_2Si_2$ [76], Γ_4 and Γ_3 form a closely spaced 'pseudo-doublet' ground state and play an important role in its metamagnetic behavior. Therefore, in the construction of a "toy model" to represent Tb in $TbNi_2Ge_2$ one needs to be able to examine the effects of Γ_3 and Γ_4 levels as they can be expected to be significant in this case from the isostructural relationship to $TbNi_2Si_2$. Such representations can be formed for an ion with $J = 2$ as shown below. It is pointed out that although no rare earth elements have $J = 2$ in their ground state some excited states with $J = 2$, such as $^7F_2$, do exist for both trivalent Tb and Eu [16]. As will be clear below, such a simple system is quite rich in its magnetic behavior and provides physically plausible explanations of some of the observations discussed above.

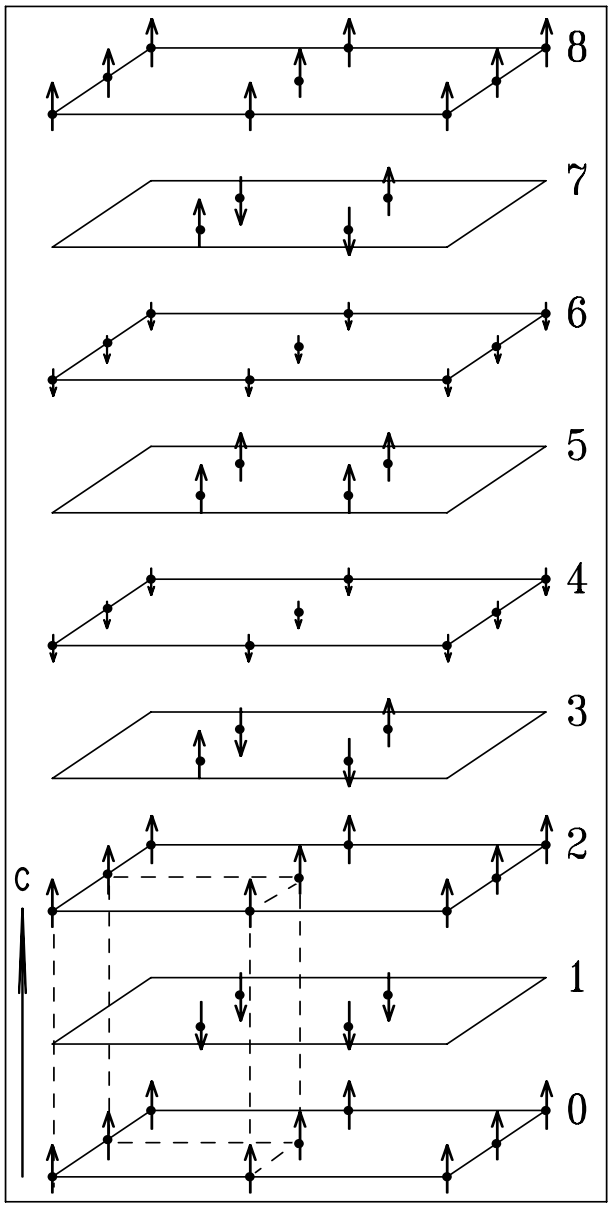

Figure 6.10 A model magnetic unit cell of MP I. It is very similar to the EM, structure shown in Fig. 6.4, with the exception of reduced moments on plane #4 and #6. The solid circles represent Tb atoms. Ni and Ge atoms are not shown.

Single-ion ($J = 2$) Behavior

The Hamiltonian of a single such ion within a constant J-multiplet can be taken to consist of two terms as shown below

$$\begin{aligned}\mathcal{H} &= \mathcal{H}_{\text{CEF}} + \mathcal{H}_{\text{Zee}} \\ &= (B_2^0 O_2^0 + B_4^0 O_4^0 + B_4^4 O_4^4 + B_6^0 O_6^0 + B_6^4 O_6^4) + g_J \mu_B \mathbf{J} \cdot \mathbf{H}_{\text{local}},\end{aligned} \tag{6.1}$$

where the first term is the CEF part and the second one accounts for the Zeeman interaction with a *local* magnetic field. The B_l^m's are the CEF parameters characteristic of a material and the O_l^m's are Stevens' operators [8]. In an applied field along the $\hat{\mathbf{c}}$ axis the Hamiltonian simplifies to

$$\mathcal{H} = \mathcal{H}_{\text{CEF}} + g_J \mu_B J_z H_z. \tag{6.2}$$

Let the eigenstates of $\mathcal{H}$ and $\mathcal{H}_{\text{CEF}}$ be Ψ_i and ϕ_j, respectively, such that

$$\mathcal{H}|\Psi_i\rangle = E_i|\Psi_i\rangle, \tag{6.3}$$

$$\mathcal{H}_{\text{CEF}}|\phi_j\rangle = \epsilon_j|\phi_j\rangle. \tag{6.4}$$

First consider the CEF eigenstates, ϕ_j, for $J = 2$ in D_{4h} symmetry. According to group theoretical branching rules [106] the $\mathrm{D}_{J=2}$ manifold decomposes as follows

$$D_{J=2} = \Gamma_1 \oplus \Gamma_3 \oplus \Gamma_4 \oplus \Gamma_5 \ ,$$

where Γ_5 is the two dimensional irreducible representation of the D_{4h} point group and the remaining representations are singlets. The eigenvalues and eigenfunctions belonging to these representations can be obtained by diagonalizing $\mathcal{H}_{\text{CEF}}$ which is written in the matrix form as

$$\mathcal{H}_{\text{CEF}} = \begin{pmatrix} d & a & 0 & 0 & 0 \\ a & d & 0 & 0 & 0 \\ 0 & 0 & c & 0 & 0 \\ 0 & 0 & 0 & b & 0 \\ 0 & 0 & 0 & 0 & b \end{pmatrix}.$$

The rows (columns) are labeled from the top (left) by 2, -2, 0, -1 and 1, respectively. The entries for the matrix elements [8, 9] are functions of the CEF parameters as shown below.

$$a = 6B_2^0 + 12B_4^0. \tag{6.5}$$

$$b = -3B_2^0 - 48B_4^0. \tag{6.6}$$

$$c = -6B_2^0 + 72B_4^0. \tag{6.7}$$

$$d = 12B_4^4. \tag{6.8}$$

Notice that the matrix elements are independent of the sixth order CEF parameters, as expected since a charge distribution with $J = 2$ can not possess multipoles higher than fourth order which can couple to these higher order terms. Also, it should be pointed out that although the higher order CEF terms such as B_4^0 and B_4^4 are smaller than the second order term, B_2^0, their prefactors are significantly larger. This is a general feature due to the large matrix elements of these terms. Thus, even though the higher order terms are one or two orders of magnitude smaller, they may not be neglected and can play an important role in systems with higher angular momentum such as Tb, since the matrix elements grow with J. Although the behavior of a single ion is being studied here, it should be commented that Stevens operators are strongly temperature dependent and grow as $\left(\frac{|\langle \mathbf{J} \rangle|}{J}\right)^{\frac{l(l+1)}{2}}$ with increasing magnetic ordering. As a result, the influence of the higher order operators on the metamagnetic phases can be significant.

The Hamiltonian matrix above is already block diagonal and only the 2×2 sub-matrix needs to be diagonalized. The normalized CEF eigenfunctions and eigenvalues are :

$$\begin{aligned}
\Gamma_1: &\quad |\phi_0\rangle = |0\rangle &&\quad \epsilon_0 = c \\
\Gamma_5: &\quad |\phi_1\rangle = |1\rangle &&\quad \epsilon_1 = b \\
\Gamma_5: &\quad |\phi_2\rangle = |\bar{1}\rangle &&\quad \epsilon_2 = b \\
\Gamma_3: &\quad |\phi_3\rangle = \tfrac{1}{\sqrt{2}}(|2\rangle + |\bar{2}\rangle) &&\quad \epsilon_3 = a + d \\
\Gamma_4: &\quad |\phi_4\rangle = \tfrac{1}{\sqrt{2}}(|2\rangle - |\bar{2}\rangle) &&\quad \epsilon_4 = a - d
\end{aligned}$$

Now the Zeeman term will split the doublet and admix the Γ_3 and Γ_4 singlets which are separated by $\Delta = 2d$. As before, only the 2×2 matrix needs to be diagonalized in order to get the eigenfunctions and eigenvalues [107]. It is evident that the totally symmetric representation, Γ_1, will remain unaffected by the field. The normalized eigenstates and the eigenvalues of $\mathcal{H}$ are thus

$$\begin{aligned}
|\Psi_0\rangle &= |\phi_0\rangle && E_0 = c \\
|\Psi_1\rangle &= |\phi_1\rangle && E_1 = b + g_{_J}\mu_{_B}H_z \\
|\Psi_2\rangle &= |\phi_2\rangle && E_2 = b - g_{_J}\mu_{_B}H_z \\
|\Psi_3\rangle &= \cos(\tfrac{\alpha}{2})|\phi_3\rangle + \sin(\tfrac{\alpha}{2})|\phi_4\rangle && E_3 = a + \sqrt{d^2 + (2g_{_J}\mu_{_B}H_z)^2} \\
|\Psi_4\rangle &= \sin(\tfrac{\alpha}{2})|\phi_3\rangle - \cos(\tfrac{\alpha}{2})|\phi_4\rangle && E_4 = a - \sqrt{d^2 + (2g_{_J}\mu_{_B}H_z)^2},
\end{aligned}$$

where

$$\tan(\alpha) = -\frac{4g_{_J}\mu_{_B}H_{_z}}{2d}. \tag{6.9}$$

Note that the energy of the singlet is independent of the field, whereas the energies of $|\Psi_2\rangle$ and $|\Psi_4\rangle$ decrease with increasing field and those of $|\Psi_1\rangle$ and $|\Psi_3\rangle$ increase (see Fig. 6.11(c) and (d)). From these eigenfunctions and eigenvalues the magnetization as a function of field and temperature can be calculated. The induced moment of a single

ion is given by the thermal average according to[3]

$$M(H_z,T) = -g_J\mu_B \frac{\sum_i \langle\Psi_i|J_z|\Psi_i\rangle e^{-\frac{E_i}{k_BT}}}{\sum_i e^{-\frac{E_i}{k_BT}}}. \tag{6.10}$$

Using the above expression the magnetization for two different sets of CEF parameters, as listed in Fig. 6.11(a) and (b), was calculated. These sets were chosen to illustrate the different behaviors of planar ($B_2^0 > 0$) and uniaxial ($B_2^0 < 0$) systems. The magnitude of this parameter is approximately the value estimated from the paramagnetic Curie temperatures of $TbNi_2Ge_2$ [23]. B_4^4 was selected to make Δ comparable to that (6$\sim$7 K) found in $TbNi_2Si_2$ [76]. For ^7F_J multiplets of Tb^{+3} the Landé factor $g_J = \frac{3}{2}$. The top panels ((a) and (b)) in Fig. 6.11 show the field dependence of the energies of the eigenstates, $|\Psi_i\rangle$. The bottom windows ((c) and (d)) display the magnetization of a single-ion as a function of field at various temperatures. When the Γ_1 singlet is the CEF ground state the saturation magnetization is reached in a step-like fashion. As the local field at the ion site reaches certain critical value[4] corresponding to a CEF level crossing (see Fig. 6.11(a)), the magnetization jumps (Fig. 6.11(c)). The magnitude of the jump is determined by the difference in the moments of the corresponding eigenstates. Similar level crossing at a higher critical field gives rise to the second jump in the magnetization. Fig. 6.11(c) also shows the sensitivity of these metamagnetic transitions to temperature. As can be seen, the lower the temperature, the sharper are the transitions.

If, on the other hand, the CEF ground state is a Γ_3 or Γ_4 singlet the magnetization is very different. As shown in Fig. 6.11(b) the energy of such a state decreases faster than that of one of the states issued from the doublet. Thus, no higher levels cross the ground state. The magnetization (Fig. 6.11(d)) saturates as the field 'purifies' or 'polarizes' the singlet and exhibits Brillouin-type behavior. It should be noted, however, at a

[3]This expression of the magnetization can be obtained from its definition, $M = -\left(\frac{d\mathcal{F}}{dH}\right)_{H\to 0}$, where the Helmholtz free energy, $\mathcal{F} = -k_B T ln\left(\mathrm{Tr}\{e^{-\beta\mathcal{H}}\}\right)$.

[4]The expressions for the critical fields are, $H_{C1} = \frac{3B_2^0 - 120B_4^0}{g_J\mu_B}$ and $H_{C2} = \frac{6\sqrt{(B_2^0 - 5B_4^0)^2 - (B_4^4)^2}}{g_J\mu_B}$, respectively.

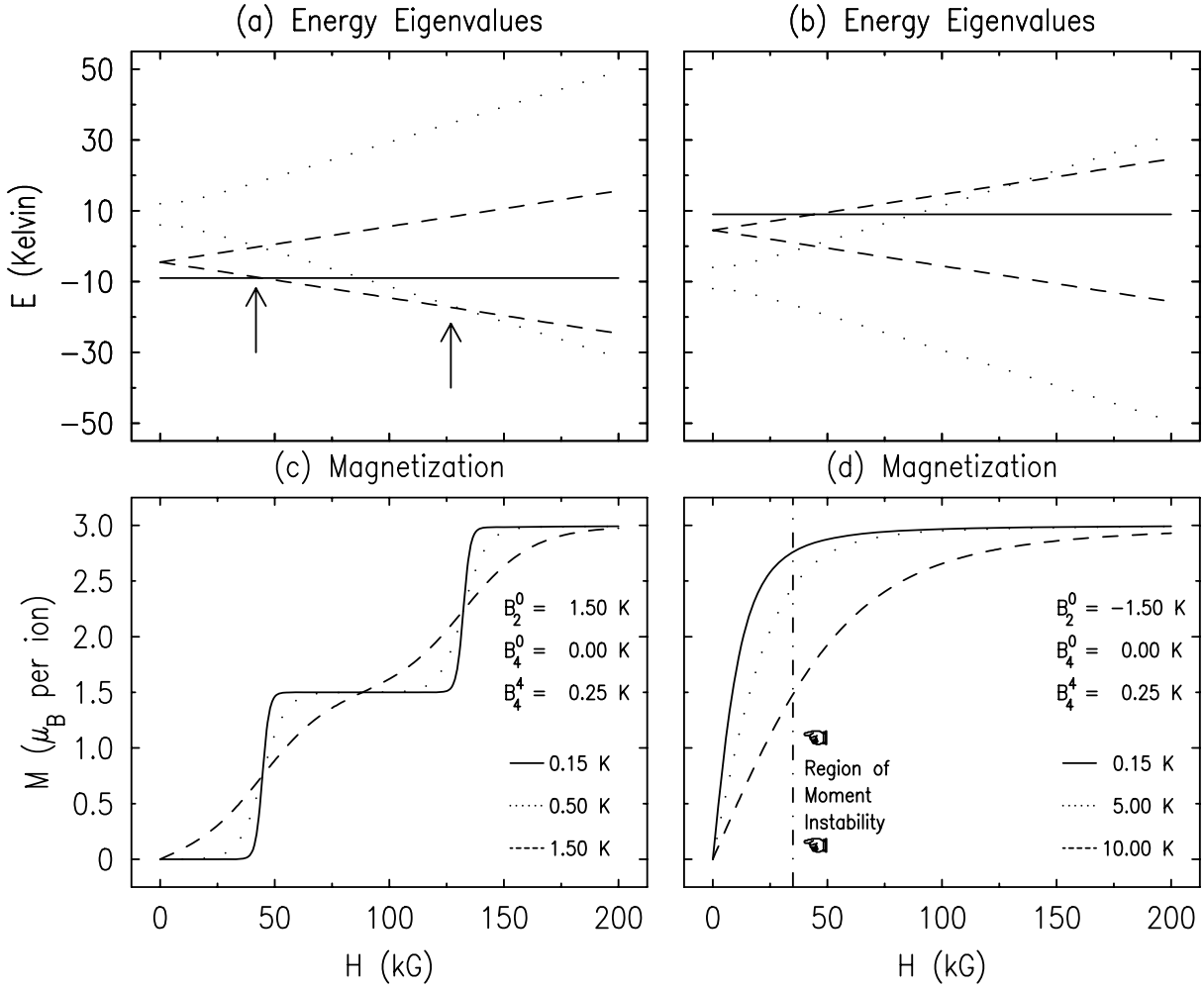

Figure 6.11 The energy eigenvalues (in units of K; (a) and (b)) and the low temperature magnetization ((c) and (d)) of a single-ion. The CEF parameters are shown in the bottom panels above the legends. When the CEF ground state is Γ_1 the higher levels cross the ground state as marked by arrows in (a). Note the corresponding jumps in the magnetization in (c). There are no such level crossings of the ground state when it is Γ_4 (see (b)). However, in this case there is a region of *moment instability* which is located to the left of the dotted-dashed vertical line in (d). See text for details.

temperature $T \sim \frac{\Delta}{40}$ the magnitude of the ionic moment is $\lesssim$90% of the saturation value up to a field as high as 30 kG $\sim \Delta$. In this region the magnitude of the moment depends sensitively on the strength of the field. Thus, this range of field may be considered a region of *moment instability*.

The temperature dependence of the susceptibility, $\chi(T)$, for a given field also shows characteristic differences for the two cases. Fig. 6.12 shows $\chi(T)$ for four different field values. Depending on the magnitude of the applied field $\chi(T)$ shows very different behavior. When the CEF ground state is Γ_4 (Fig. 6.12(a)), for low field value where linear behavior of magnetization is observed, $\chi(T)$ changes very slowly at first and then starts to fall off much faster when thermal population of the higher CEF levels with low moment starts to become appreciable at $T \gtrsim \frac{\Delta}{3}$. The exact dependence of $\chi(T)$ is determined by the location of H in the region of moment instability. For H beyond this region, the moment remains saturated and $\chi(T)$ is almost T-independent. In the case of Γ_1 ground state (Fig. 6.12(b)), $\chi(T)$ shows a maximum at a finite T when H<H_{C1} and rapidly vanishes as $T \to 0$ K. The maximum is due to thermal population of CEF levels above the ground state with larger magnetic moment. For H_{C2}>H>H_{C1}, $\chi(T)$ has a finite value at $T = 0$ due to CEF level crossing and has a maximum at a finite T because of thermal population of a next CEF level with even higher moment. This maximum shifts toward $T = 0$ as H gets closer to H_{C2}. Finally, for H right above H_{C2}, the moment is saturated at low T and $\chi(T)$ drops off as T is raised.

Moment Instability and Metamagnetism

In order to show the relevance of the computations presented above to metamagnetism in real systems such as $TbNi_2Ge_2$ ones needs to take the single-ion model one step further. Consider an array of planes[5] of such ions and form 'hypothetical' ordered magnetic states such as those shown in the bottom panels of Fig. 6.13. The arrows

[5]Assuming all the moments in a given plane to be the same.

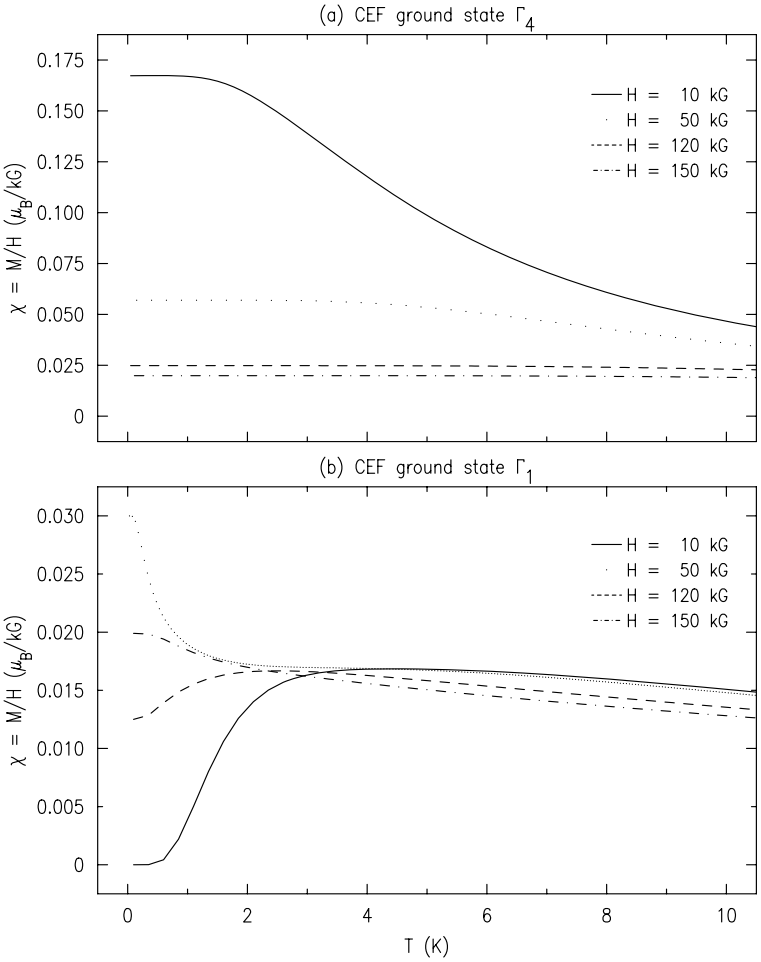

Figure 6.12 Single-ion magnetization as a function of temperature at four different fields as indicated. The top panel, (a), is for the case when Γ_4 is the CEF ground state and the bottom panel, (b), is for Γ_1 ground state. Only the low temperture portion, where significant T-dependence is observed, has been shown for each case. In the higher temperature region $\chi(T)$ values merge into each other.

represent the ionic moments pointing along the $\hat{\mathbf{c}}$ axis. Whereas the length of an arrow indicates the magnitude of the moment, the absence of an arrow implies that the ionic moment is zero. Such ordered structures may arise due to their mutual exchange interactions mediated by the conduction electrons. In the mean field approximation the ordered state can be viewed as due to some periodic mean field, PMF, (as shown by the square-wave-like solid lines in the figures) whose magnitude and direction at an ionic site determine its magnetic state. The key point is that an individual ion is subjected to a *local* magnetic field generated by all the other ions. When this field is sufficiently strong the ionic moment saturates; otherwise, its magnitude is lower. Now in the case of a Γ_1 ground state when the local field is smaller than one of the critical fields, the ionic moment is correspondingly reduced due to CEF level crossing. However, since $B_2^0 > 0$, such a system is planar and not applicable to a uniaxial system such as $TbNi_2Ge_2$. In the model calculation with $B_2^0 < 0$ the ground state is a Γ_4 singlet and the question arises as to whether a reduction of moment can take place in such a case. An inspection of the magnetization curve (see Fig. 6.11(d)) and the field dependence of the CEF eigenvalues (see Fig. 6.11(b)) shows that if the PFM responsible for magnetic order is comparable to or less than Δ at certain sites then the magnetic moments at those sites can be *smaller* than the saturation value. This may provide one possible explanation for the moment reduction observed in MP I of $TbNi_2Ge_2$. It is interesting to note that the magnitude of the reduced moments is not unique and should vary within the phase. Such variation seems to be consistent with the continuous change of the integrated intensity of the $\boldsymbol{\tau}_1$ satellite within MP I (Fig. 6.9) and the nonzero slope of M($\mathbf{H}$) (Fig. 6.1).

Now consider the response of the ordered arrays of ions (as shown in Fig. 6.13(A) and (B), in the absence of an external field) with Γ_4 CEF ground state to an applied field along the $\hat{\mathbf{c}}$ axis. In general, in an external field the ionic moments will rearrange themselves so as to attain the minimum free energy. Such computational task in order to obtain the lowest-energy state not only involves minimization of the total energy of the

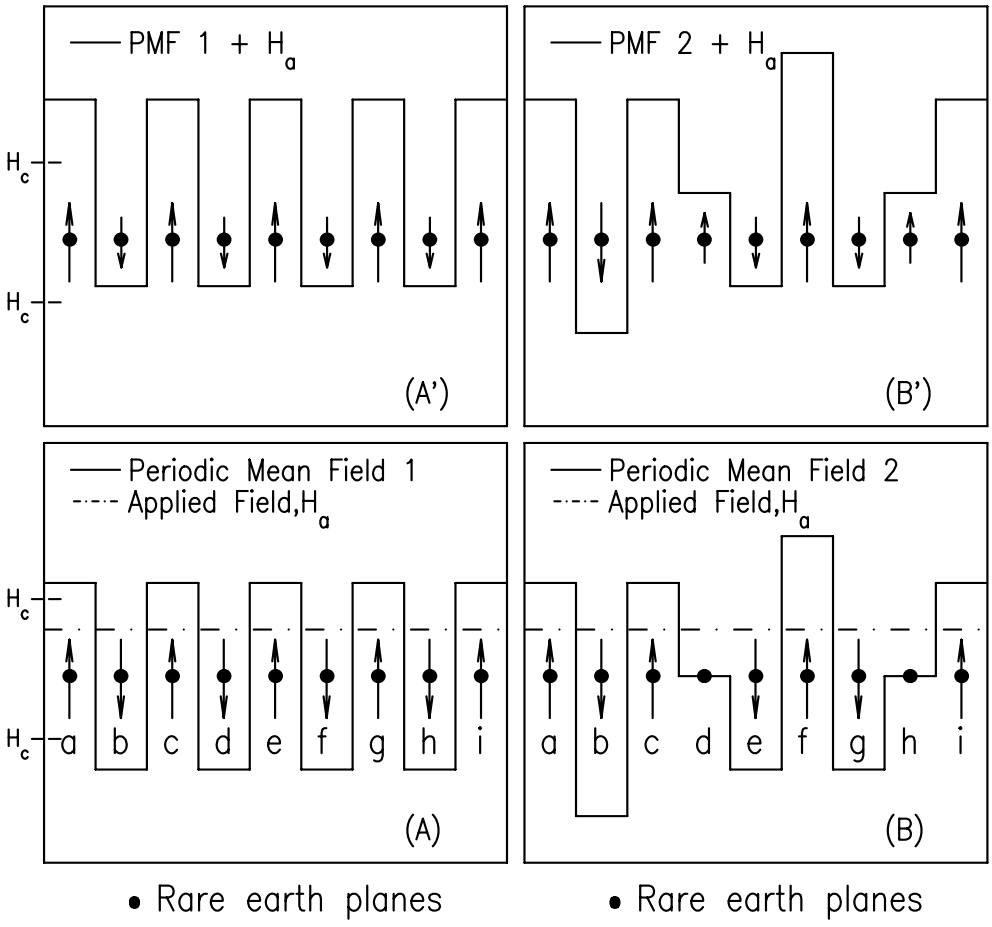

Figure 6.13 'Hypothetical' ordered magnetic states due to some periodic mean field, (A) and (B), in the absence of an external field. Application of a field increases the local magnetic field uniformly in the RSA as shown by the solid lines in (A′) and (B′). Corresponing changes in the magnetic structures are also displayed. The minimum field necessary to saturate the single-ion moment is indicated by H_c.

local-moment system but also a full self-consistent band calculation for the conduction electrons. This is a formidable task and for the purpose of this work the crude *rigid shift approximation* (RSA) is made which states that the net effect of the external field is simply to superpose a uniform field on the PMF mentioned above.

In order to illustrate this, consider the dotted-dashed line in Fig. 6.13(A) and (B) which indicates some magnitude of an applied field. The solid line in (A′) and (B′) is the sum of this field and the PMF shown in (A) and (B), respectively. In the case of PMF 1, moments such as a and c remain fully saturated since the local fields are larger than the critical field (H_c) necessary saturation, whereas ionic moments at b and d are substantially reduced. These ions are subjected to field lower than H_c and their moments are consequently diminished. In the case of a more complicated structure (PMF 2, (B)) ionic moments may vanish at certain sites (such as b, e and g in (B)) and grow from a nonmagnetic state at others (such as d and h). Thus, a magnetically ordered state containing both nonmagnetic (or weakly magnetic) and magnetic ionic states are possible. Such "mixed" phase behavior has recently been reported for the isostructural $TbRu_2Ge_2$ compound [102]. In this compound such mixed phase behavior occurs due to CEF level crossing of the ground state singlet, whereas in the present case there is no level crossing. The reduction of the moment is due to moment instability which arises from the singlet nature of the ground state and the comparable strengths of the local field and the CEF splitting of the low-lying states.

Within the RSA the total magnetization of the ensemble of these ions has been calculated, as shown in Fig. 6.14. The top panel is for PMF 1 and the bottom one is for PMF 2. Due to the presence of the nonmagnetic ionic state in PMF 2 the magnetization rises sharply as these ionic moments grow toward saturation. In the case of PMF 1 no changes in the magnetization (Fig. 6.14(a)) take place until the applied field reduces the local field below H_c at sites like b in Fig. 6.13(A) and (A′). These ionic moments aligned with -$\hat{\mathbf{c}}$ become zero and then grow along $\hat{\mathbf{c}}$ as the transition proceeds. Similarly, a situa-

tion due to gradual changes of moments takes place in the case of PMF 2. Interestingly, however, the slope of the terraces and those at the transitions are all different (see the bottom panel in Fig. 6.14). Quantitatively, the slope is determined by $\left(\frac{1}{N}\right)\sum_{i=1}^{n}\left|\frac{dM_i}{dH}\right|$ where n is the number of unstable ions and there are N ions in total. So, the slope not only depends on the number of ions with weak moments but also on how unstable these moments are. In the intermediate phase there are three unstable moments giving rise to larger slope. Such a phase is going to be quite sensitive to temperature as can be seen from Fig. 6.11(d) and will disappear at $T \sim \Delta$ as shown by the dashed line in Fig. 6.14(b).

Although the study of the single-ion with $J = 2$ presented above revealed some peculiar magnetic properties, it cannot be stated with certainty that such behaviors are responsible for metamagnetism in $TbNi_2Ge_2$. However, the model calculations do suggest how the qualitative features found in M($\mathbf{H}$) (see Fig. 6.1), as discussed at the beginning of this chapter, and the moment reduction might arise from the single-ion moment instability within RSA. This is a direct consequence of the *comparable* magnitudes of the CEF splitting and exchange interactions. Thus, the critical ingredients needed for a quantitative theoretical work are the CEF parameters and the exchange coupling constants, both of which have to be determined experimentally.

Summary

In summary, the neutron diffraction results on the metamagnetic phases of $TbNi_2Ge_2$ have been discussed. A surprising result is the presence of AF planes in all the phases. As the measurements show, these phases are very complex and a simple spin-flip mechanism is inadequate to explain the transitions. A model structure of the first metamagnetic phase was presented. This is a mixed phase containing Tb ions with reduced moments at certain planes whereas the remaining ions have fully saturated moments. Model

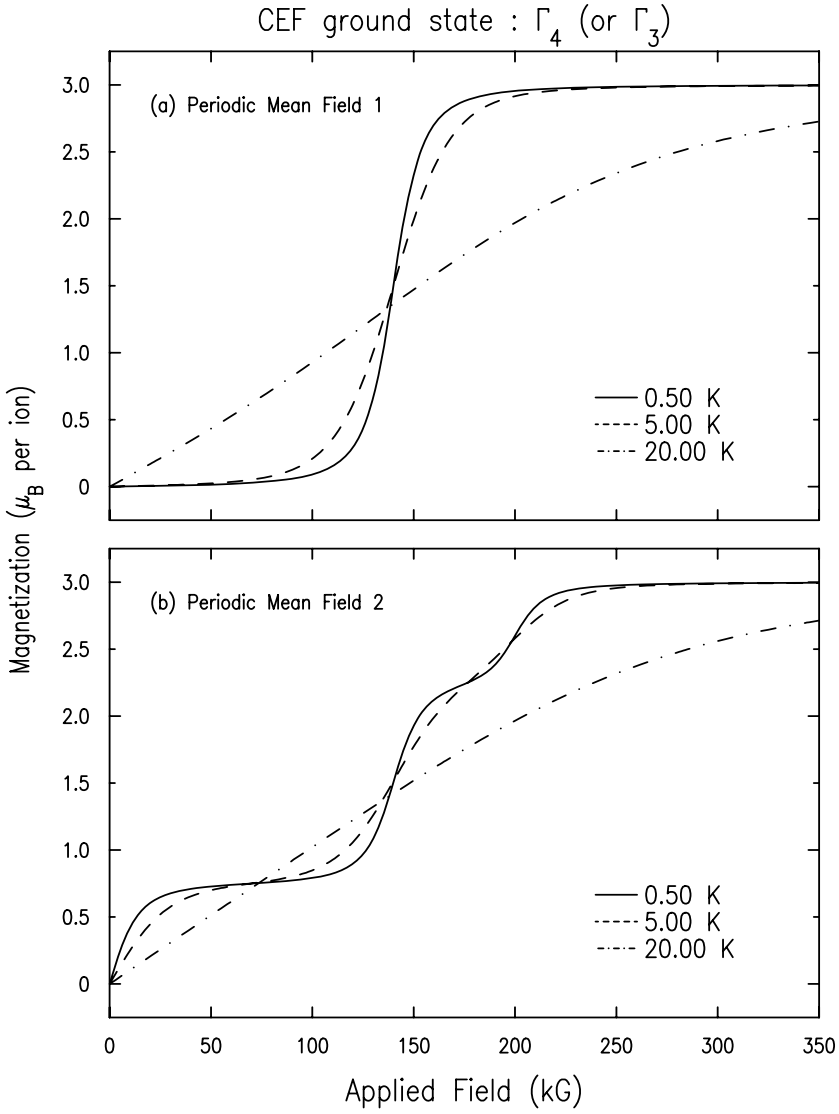

Figure 6.14 'Metamagnetic' behavior at three different temperatures of a set of ions with Γ_4 CEF ground state for two different PMFs as shown in Fig. 6.13(A) and (B).

calculations for a single ion with $J = 2$ show that due to the singlet nature of the CEF ground state magnetic moments at particular sites may be small where the local magnetic fields are lower than the minimum field necessary for saturation. However, the model requires the exchange interactions to be comparable to the CEF splitting of the low lying states.

It should be commented that due to severe peak overlaps in the higher-field phases accurate integrated intensity measurements were not possible and the exact nature of these phases are not known. The major hindrance to such measurements lies in the fact that the primary magnetic wave vector $\boldsymbol{\tau}_1$ is along the $\hat{\mathbf{c}}$ axis, the direction of the external field required to observe metamagnetism. This means that a cryogenic magnet with magnetic field in the horizontal scattering plane and maximum field larger than 5 T is needed so that the sample can be mounted with the $\hat{\mathbf{c}}$ axis in the scattering plane which will considerably improve the $\mathbf{Q}$-resolution necessary. Unfortunately, neither of the two available magnets used for this work met both the criteria. One way to resolve the overlapping peaks is to use neutrons with longer wavelength. Finally, XRES mesurements of the metamagnetic phases may also be possible in the future as the appropriate sample environment becomes available. Precise XRES measurements of $\boldsymbol{\tau}_1$ will be very useful for a better understanding of these phases, as was shown to be the case in the zero-field structures. It is the hope of this dissertation that the results obtained via the current set of experiments will be the basis of and a useful guide for such future investigations with neutrons and XRES.

7 CONCLUSIONS

In summary, the interplay of long-range magnetic order and single-ion anisotropy in rare earth nickel germanides, $R\mathrm{Ni}_2\mathrm{Ge}_2$, has been studied using a combination of x-ray resonant exchange scattering (XRES) and neutron diffraction techniques. In this process the utility of the XRES technique in the study of magnetism has also been demonstrated. In particular, its inherent high **Q**-resolution to determine precisely the modulation vectors, elemental selectivity to study magnetic sublattices independently and the convenience to study compounds containing highly neutron-absorptive materials were found invaluable in the present work.

This thesis was primarily focused on the Pr, Nd, Sm and Eu through Tm members with magnetically ordered ground state. A paramagnetic-to-antiferromagnetic (AF) transition is observed in all these compounds at T_N. Three classes of incommensurate magnetic structures are found at the onset of ordering (at T_N). An AM longitudinal spin wave (LSW) with moments along the $\hat{\mathbf{c}}$ axis is observed in the uniaxial $\mathrm{TbNi}_2\mathrm{Ge}_2$ and $\mathrm{NdNi}_2\mathrm{Ge}_2$ [36]. The planar system $\mathrm{TmNi}_2\mathrm{Ge}_2$ [24], and also $\mathrm{EuNi}_2\mathrm{Ge}_2$, order with the moments in the basal plane. In the case of the Tm compound, the structure may be a flat spiral. On the other hand, weakly anisotropic systems, such as the Dy and Er [40] members, as well as isotropic $\mathrm{GdNi}_2\mathrm{Ge}_2$, prefer an intermediate structure with ordered moments canted away from the $\hat{\mathbf{c}}$ axis. In these latter compounds, a conical AF structure may also be stabilized.

Although the exact ordered configuration of the localized $4f$-moments of a given material is the result of a compromise between the competing CEF ($\mathcal{H}_{\mathrm{CEF}}$) and RKKY

($\mathcal{H}_{\rm RKKY}$) interactions, the long-range nature is determined by the latter. It has been established that strong Fermi surface nesting which dramatically enhances such interaction, is responsible for the magnetic wave vector at the Néel transition in $R\mathrm{Ni_2Ge_2}$ compounds. This is the most important theoretical result obtained in this work. Although this dissertation is concerned with a particular family of compounds, this result is likely to be applicable to other isostructural rare earth intermetallic systems as well because of the generality of $\mathcal{H}_{\rm RKKY}$. Indeed, a literarture search reveals the persistence of a single incommensurate wave vector of the form (0 0 q_z) across some isostructural series of compounds, such as $R\mathrm{Co_2}X_2$, and $R\mathrm{Rh_2}X_2$ (X = Si or Ge) [3].

In addition, experimental and computational investigations of the Gd and Eu compounds were carried out in order to understand the effects of band filling on ordered states. $\chi_0(\mathbf{q})$ calculations predicted a continuous transition from the *incommensurate* structure observed in the Gd compound to the *commensurate* structure of its Eu neighbor as a function of band filling. This transformation may manifest in the pseudoternary alloy $\mathrm{Gd}_{1-x}\mathrm{Eu}_x\mathrm{Ni_2Ge_2}$. Future XRES studies of these compounds to verify this prediction and to determine at what Gd concentration lock-in to the commensurate structure, (0 0 1), will occur are suggested.

Based upon current understanding of long-range order (LRO) and anisotropy in these compounds, it is expected that below T_N, $\mathrm{PrNi_2Ge_2}$ will order in a LSW whereas in $\mathrm{SmNi_2Ge_2}$ the moments will be locked to the plane as in the case of a flat spiral. Also, a flat spiral reported [38] for $\mathrm{HoNi_2Ge_2}$ appears to be consistent with the series-wide behavior. Diffraction measurements on single-crystal samples are left for the future to determine these structures.

Next, the ordered structures below T_t, of the Dy, Tb, Gd, and Eu compounds have been presented. In the Tb [44] and Dy [45] compounds, the structures below T_t are EM *commensurate*, described by a set of three propagation vectors, namely, $\boldsymbol{\tau}_1 = (0\ 0\ \frac{3}{4})$ along with its third harmonic $\boldsymbol{\tau}_1' = (0\ 0\ \frac{1}{4})$, $\boldsymbol{\tau}_2 = (\frac{1}{2}\ \frac{1}{2}\ 0)$ and $\boldsymbol{\tau}_3 = (\frac{1}{2}\ \frac{1}{2}\ \frac{1}{2})$. In

$TbNi_2Ge_2$, the ordered moments are along the $\hat{\mathbf{c}}$ axis while there is an ordered component in the basal plane in $DyNi_2Ge_2$. XRES studies on $EuNi_2Ge_2$ found a canonical simple AF ordering with temperature-independent propagation vector (0 0 1) and ordered moments in the basal plane. Similar XRES studies of $GdNi_2Ge_2$ revealed the magnetic structure to be *incommensurate* with modulation (0 0 0.806) at 13 K. As in $EuNi_2Ge_2$, the moments are also in the basal plane [43].

In order to study the effects of an external field on magnetic structure which is represented in the Hamiltonian as $\mathcal{H}_{\text{Zee}}$, neutron diffraction studies on the metamagnetic structures of $TbNi_2Ge_2$ have been performed. One surprising discovery is the presence of antiferromagnetically ordered planes in all the metamagnetic phases which are expected to become ferromagnetically ordered through *spin-flip* mechanism. Although the structures of the high-field phases have only been characterized, a model structure for the first metamagnetic phase has been presented. According to the model this is a "mixed" phase consisting of Tb ions with saturated as well as significantly reduced moments.

Finally, in order to understand the origin of such moment reduction induced by an external field a "toy model" of an ion with J=2 has been studied in detail. These studies show that due to the non-Kramers nature of such an ion, a Γ_4 singlet ground state with a low-lying Γ_3 singlet at an energy Δ above Γ_4 is possible. In this case a region of *moment instability* can exist for a limited range of *local* magnetic field. If the exchange interactions responsible for magnetic LRO is comparable to Δ, then in an applied field ions at certain sites may be pushed into the region of instability leading to their moment reduction. Whether such instability is at play in $TbNi_2Ge_2$ can not be stated with certainty. The knowledge of the CEF and exchange parameters is required for a theoretical understanding of metamagnetism in this system which will have to await future investigations.

APPENDIX A SHORT RANGE ORDER IN $TbNi_2Ge_2$

In this appendix the observation of *short range order* above T_N in $TbNi_2Ge_2$ is presented. Paramagnetic diffuse scattering of neutrons is equivalent to diffuse scattering of x-rays from amorphous materials. Whereas x-ray diffuse scattering reveals short range charge density correlations its neutron analog provides valuable information about *short-range* magnetic order in condensed matter.

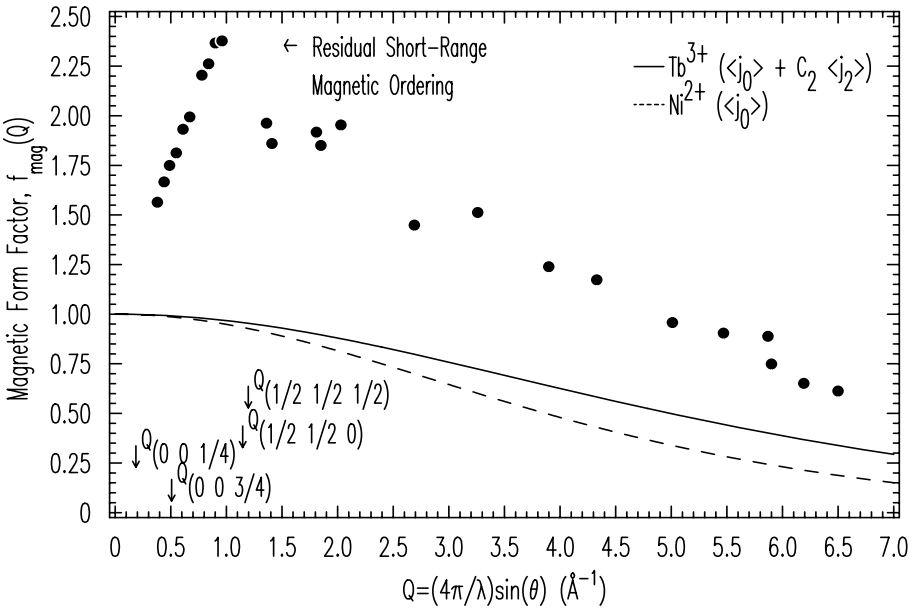

Figure A.1 Paramagnetic diffuse scattering from $TbNi_2Ge_2$. Solid and dashed lines are calculated form factors of Tb^{+3} and Ni^{+2} ions.

Neutron diffraction measurements of polycrystalline $TbNi_2Ge_2$ samples found noticeable magnetic diffuse scattering above T_N. However, since paramagnetic diffuse scattering is completely incoherent, in order to put this scattering on an absolute scale

with the coherent nuclear scattering one needs to account for other sources of incoherent scattering. These sources are : (1) thermal diffuse (phonon) scattering, (2) isotopic incoherence, (3) nuclear spin incoherence, (4) multiple Bragg scattering and (5) incoherent scattering from residual moisture in the sample due to high spin incoherent cross-section of hydrogen nuclei. Except for thermal diffuse scattering all the other sources of incoherent scattering are present even at the lowest temperature. As for thermal scattering, it is assumed to be negligible for the temperature range of measurements. Thus, one can eliminate all these contributions simply by subtracting angular regions of common width away from Bragg peaks at 4 K from those at 20 K and can extract the magnetic diffuse scattering at 20 K. In this process contributions of constant background, which is assumed to be temperature independent are also subtracted off. Using the scale factor determined from the nuclear reflections (see Appendix B), magnetic diffuse scattering can be placed on absolute scale with the nuclear peaks and the form factor can be extracted according to the cross-section formula for paramagnetic scattering [54]:

$$\left(\frac{d\sigma}{d\Omega}\right)_{para} = \frac{2}{3} N_{ion} \left(\frac{g_n e^2}{2m_e c^2}\right) J(J+1) \left|f(\mathbf{Q})\right|^2 \tag{A.1}$$

Fig. A.1 shows the form factor extracted from the observed diffuse scattering. For comparison, calculated form factors (in the dipole approximation) of Tb^{+3} and Ni^{2+} ions are also shown. The extracted form factor significantly deviates from the theoretical results and exhibits a maximum at $\sim$1 $Å^{-1}$. The presence of such a peak indicates that at 20 K Tb moments are not *completely randomly* oriented; there is some residual short range order of the Tb moments above T_N.

APPENDIX B $TbNi_2Ge_2$: POWDER NEUTRON DIFFRACTION ($T > T_N$)

Table B.1 Calculated and observed intensities of nuclear Bragg reflections of $TbNi_2Ge_2$ at $T = 20$ K. I_{Obs} and I_{Cal} correspond to observed and calculated intensity of Bragg peak(s), respectively. The intensities in the case of overlapping peaks are given in the row for the strongest peak in the group. The scaling factor obtained from these calculations is used for putting magnetic peaks on an absolute scale with the nuclear peaks.

No.	(h k l)	Q(Å^{-1})	I_{Obs}	I_{Cal}
1	(0 0 2)	1.2844	223 ± 7	222 ± 11
2	(1 0 1)	1.6826	47 ± 3	57 ± 4
3	(1 0 3)	2.476	581 ± 29	488 ± 35
4	(1 1 2)	2.547	1090 ± 33	1059 ± 50
	(0 0 4)			
5	(2 0 0)	3.1105	895 ± 27	901 ± 45
6	(2 0 2)	3.3652	930 ± 28	863 ± 35
7	(1 2 1)	3.5364	283 ± 9	289 ± 14
	(1 0 5)			
8	(0 0 6)	3.8531	32 ± 2	30 ± 3
9	(1 2 3)	3.9756	502 ± 25	438 ± 22
10	(2 0 4)	4.0341	75 ± 4	79 ± 4
11	(2 2 0)	4.3989	1061 ± 33	946 ± 38
	(1 1 6)			
12	(2 2 2)	4.5826	90 ± 5	94 ± 5
13	(3 0 1)			
	(1 2 5)	4.7333	370 ± 11	372 ± 12
	(1 0 7)			
14	(2 0 6)	4.9520	57 ± 4	87 ± 5

Table B.1 (Continued)

No.	(h k l)	Q(Å^{-1})	I_{Obs}	I_{Cal}
15	(3 0 3)			
	(1 3 2)	5.0831	958 ± 29	957 ± 33
	(2 2 4)			
16	(0 0 8)	5.1375	204 ± 7	229 ± 6
17	(1 3 4)	5.5485	789 ± 24	828 ± 33
18	(2 3 1)			
	(3 0 5)	5.6639	218 ± 7	202 ± 6
	(1 2 7)			
19	(2 2 6)	5.8478	60 ± 3	88 ± 5
20	(2 3 3)	5.9292	400 ± 20	347 ± 18
21	(1 0 9)			
	(2 0 8)	6.0058	1118 ± 33	997 ± 40
22	(4 0 0)	6.2210	1421 ± 43	1454 ± 58
	(1 3 6)			
23	(4 0 2)	6.3522	117 ± 5	118 ± 6
24	(0 0 10)	6.4219	29 ± 2	32 ± 3
25	(1 4 1)			
	(2 3 5)	6.4618	494 ± 25	590 ± 30
	(3 0 7)			
Nuclear	R-Bragg = 7%			

The agreement index, R-Bragg, is calculated according to: $R\text{-Bragg} = \frac{(\sum |I_{Obs} - I_{Cal}|)}{\sum I_{Obs}}$.

APPENDIX C $TbNi_2Ge_2$: POWDER NEUTRON DIFFRACTION ($T_t < T < T_N$)

Table C.1 Observed and calculated intensities of magnetic Bragg reflections of $TbNi_2Ge_2$ at $T = 12$ K. Superscript '+/-' in the second column stands for a τ_1 satellite. The intensities in the case of overlapping peaks are given in the row for the strongest peak in the group.

No.	(h k l)	Q(Å^{-1})	I_{Obs}	I_{Cal}	$I_{(00\frac{3}{4})}$
1	$(1\ 0\ 1)^-$	1.5630	454 ± 14	415 ± 17	414 ± 17
2	$(1\ 0\ 1)^+$	1.9218	183 ± 6	171 ± 7	172 ± 7
3	$(1\ 0\ 3)^-$	2.1194	124 ± 4	112 ± 5	110 ± 5
4	$(1\ 1\ 0)^+$	2.2527	181 ± 6	168 ± 6	169 ± 6
5	$(1\ 1\ 2)^-$	2.3396	200 ± 6	143 ± 6	142 ± 6
6	$(1\ 1\ 2)^+$	2.8239	64 ± 2	60 ± 3	60 ± 3
7	$(1\ 0\ 3)^+$	2.8711	32 ± 2	28 ± 3	28 ± 3
8	$(1\ 1\ 4)^-$	3.0286	41 ± 2	43 ± 3	43 ± 3
9	$(2\ 0\ 2)^-$	3.2111	77 ± 3	65 ± 3	64 ± 3
10	$(1\ 2\ 1)^-$	3.4811	120 ±4	108 ± 5	108 ± 5
11	$(1\ 2\ 1)^+$	3.6563	99 ± 3	85 ± 4	
12	$(1\ 2\ 3)^+$	4.2330	43 ± 2	40 ± 3	
13	$(3\ 0\ 1)^-$	4.6683	23 ± 2	22 ± 2	
14	$(3\ 0\ 1)^+$	4.8004	21 ± 2	19 ± 2	
15	$(1\ 3\ 2)^-$	4.9824	36 ± 2	35 ± 3	
16	$(1\ 0\ 7)^+$				
	$(1\ 3\ 2)^+$	5.2273	24 ± 2	28 ± 3	
17	$(2\ 3\ 1)^+$	5.7200	21 ± 2	23 ± 2	
18	$(2\ 3\ 3)^-$	5.7900	43 ± 2	39 ± 3	
	$(1\ 3\ 4)^+$				
19	$(2\ 3\ 3)^+$	6.1048	11 ± 2	19 ± 3	
Magnetic	R-Bragg = 9.3%	Overall	R-Bragg = 7.3%		

APPENDIX D $TbNi_2Ge_2$: POWDER NEUTRON DIFFRACTION ($T < T_t$)

Table D.1 Observed and calculated intensities of magnetic Bragg reflections of $TbNi_2Ge_2$ at $T = 4$ K. Indices in the second and the third columns refer to the magnetic and chemical unit cell, respectively. The intensities in the case of overlapping peaks are given in the row for the strongest peak in the group.

No.	$(h\ k\ l)_m$	$(h\ k\ l)_c \pm \boldsymbol{\tau}_{mag}$	Q(Å^{-1})	I_{Obs}	I_{Cal}
1	(1 1 0)	(0 0 0)+$\boldsymbol{\tau}_2$			
	(1 1 2)	(0 0 0)+$\boldsymbol{\tau}_3$	1.1456	293 ± 9	303 ± 12
2	(1 1 6)	(0 0 2)−$\boldsymbol{\tau}_3$	1.4620	68 ± 3	69 ± 4
3	(2 0 1)	(1 0 1)−$\boldsymbol{\tau}_1$	1.5635	619 ± 18	602 ± 24
4	(2 0 5)	(1 0 1)+$\boldsymbol{\tau}_1$	1.9188	298 ± 12	270 ± 12
5	(2 0 9)	(1 0 3)−$\boldsymbol{\tau}_1$	2.1229	172 ± 7	159 ± 6
6	(2 2 3)	(1 1 0)+$\boldsymbol{\tau}_1$	2.2516	239 ± 8	245 ± 10
7	(2 2 5)	(1 1 2)−$\boldsymbol{\tau}_1$	2.3414	277 ± 9	210 ± 9
	(2 0 11)	(1 0 3)−$\boldsymbol{\tau}_1'$			
8	(2 2 9)	(1 1 2)+$\boldsymbol{\tau}_1'$			
	(3 1 3)	(1 0 1)+$\boldsymbol{\tau}_3$	2.6410	65 ± 3	55 ± 3
9	(1 1 16)	(0 0 4)+$\boldsymbol{\tau}_2$			
	(5 1 8)	(2 0 2)+$\boldsymbol{\tau}_2$			
	(2 2 11)	(1 1 2)+$\boldsymbol{\tau}_1$	2.8207	177 ± 5	172 ± 7
	(2 0 15)	(1 0 3)+$\boldsymbol{\tau}_1$			
10	(2 2 13)	(1 1 4)−$\boldsymbol{\tau}_1$	3.0321	57 ± 2	62 ± 3
11	(4 0 5)	(2 0 2)−$\boldsymbol{\tau}_1$	3.2124	87 ± 3	95 ± 4
12	(2 4 1)	(1 2 1)−$\boldsymbol{\tau}_1$	3.4813	150 ± 5	164 ± 7
13	(2 4 7)	(1 2 1)+$\boldsymbol{\tau}_1$	3.6547	121 ± 4	134 ± 5
	(3 3 5)	(1 1 2)+$\boldsymbol{\tau}_3$			

Table D.1 (Continued)

No.	$(h\ k\ l)_m$	$(h\ k\ l)_c \pm \boldsymbol{\tau}_{mag}$	Q(Å^{-1})	I_{Obs}	I_{Cal}
14	(5 1 8)	(2 0 2)+$\boldsymbol{\tau}_2$	4.1679	21 ± 2	19 ± 2
	(3 3 16)	(1 1 4)+$\boldsymbol{\tau}_2$			
15	(2 4 15)	(1 2 3)+$\boldsymbol{\tau}_1$	4.2301	75 ± 3	59 ± 3
16	(4 4 5)	(2 2 2)−$\boldsymbol{\tau}_1$	4.4715	31 ± 2	36 ± 2
17	(6 0 1)	(3 0 1)−$\boldsymbol{\tau}_1$	4.6685	31 ± 2	32 ± 2
18	(6 0 7)	(3 0 1)+$\boldsymbol{\tau}_1$	4.7992	30 ± 2	39 ± 2
	(3 5 5)	(2 3 3)−$\boldsymbol{\tau}_3$			
19	(4 4 13)	(2 2 4)−$\boldsymbol{\tau}_1$			
	(6 0 9)	(3 0 3)−$\boldsymbol{\tau}_1$	4.8843	48 ± 2	59 ± 3
20	(2 6 5)	(1 3 2)−$\boldsymbol{\tau}_1$	4.9832	58 ± 2	51 ± 3
21	(2 6 9)	(1 3 2)+$\boldsymbol{\tau}_1$	5.2256	40 ± 2	41 ± 2
22	(6 0 15)	(3 0 3)+$\boldsymbol{\tau}_1$	5.2506	16 ± 1	18 ± 2
23	(1 5 11)	(1 3 6)−$\boldsymbol{\tau}_3$			
	(2 4 25)	(1 2 7)−$\boldsymbol{\tau}_1$	5.3107	18 ± 1	23 ± 2
24	(4 0 27)	(2 0 6)+$\boldsymbol{\tau}_1$			
	(2 6 13)	(1 3 4)−$\boldsymbol{\tau}_1$	5.3426	41 ± 2	57 ± 3
	(4 4 19)	(2 2 4)+$\boldsymbol{\tau}_1$			
25	(6 0 17)	(3 0 5)−$\boldsymbol{\tau}_1$	5.4054	15 ± 1	17 ± 2
	(1 1 30)	(1 0 7)+$\boldsymbol{\tau}_3$			
26	(4 6 7)	(2 3 1)+$\boldsymbol{\tau}_1$	5.7190	43 ± 22	44 ± 2
	(1 7 10)	(1 4 3)−$\boldsymbol{\tau}_3$			
27	(2 6 19)	(1 3 4)+$\boldsymbol{\tau}_1$			
	(2 6 9)	(2 3 3)−$\boldsymbol{\tau}_1$	5.7907	60 ± 3	58 ± 3
28	(2 6 15)	(2 3 3)+$\boldsymbol{\tau}_1$	6.1028	30 ± 2	28 ± 2
Magnetic	R-Bragg = 8.7%	Overall	R-Bragg = 6.8%		

APPENDIX E XRES STUDIES OF $PrNi_2Ge_2$ AND $SmNi_2Ge_2$

The XRES studies were carried out on the X22C beamline at the NSLS as described previously. The primary goal of these measruements was to look for the magnetic modulation vector along the ΓZ line. A platelet of $PrNi_2Ge_2$ crystal was cut and polished perpendicular to the $\hat{\mathbf{c}}$ axis. The incident photon energy was tuned to the Pr L_{II} edge (6.44 keV) where the largest resonant enhancement is expected. Reciprocal lattice scans along the [0 0 1] direction, taken at a temperature above $T_N = 20.4$ K determined from the susceptibility data [23], revealed reflections consistent with the body-centered tetragonal structure. At the base temperature of 3.7 K, superlattice peaks corresponding to $\boldsymbol{\tau}_1 = (0\ 0\ 0.813)$ were observed.

An energy scan of the $(0\ 0\ 4)^+$ superlattice peak was taken through the absorption edge to observe the resonant enhancement consistent with the magnetic origin of the peak. As was found in the Tb, Gd, and Eu compounds, the dipole resonance occurs (see Fig. E.1(a)) above the absorption edge, defined at the inflection point of the fluorescence yields (Fig. E.1(c)). For comparison the energy scan of a charge Bragg peak is displayed in Fig. E.1(b).

The temperature dependence of the magnetic peak was also measured in order to look for changes at the second transition ($T_t = 7.7$ K) [23] and to determine the ordering vector below T_N. Fig. E.2 summarizes the results of these measurements. The magnetic wave vector, corrected for thermal variation of the axial lattice parameter, increases slowly with decreasing temperature. Within the accuracy of the measurements there were no drastic changes in the longitudinal width (see Fig. E.2(b)) as in $TbNi_2Ge_2$. The

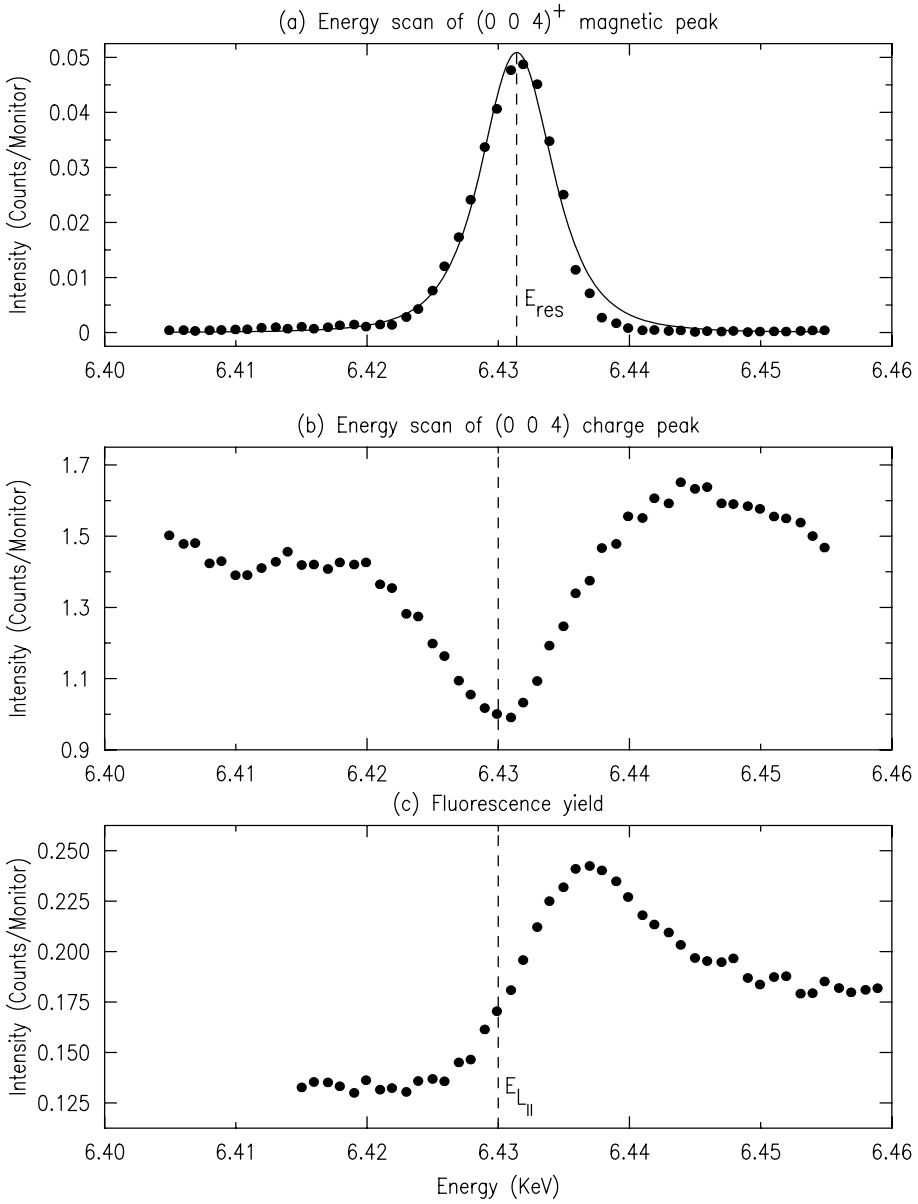

Figure E.1 Energy scans through the Pr L_{II} absorption edge. (a) $(0\ 0\ 4)^+$ magnetic peak, (b) (0 0 4) charge peak and (c) fluorescence yields.

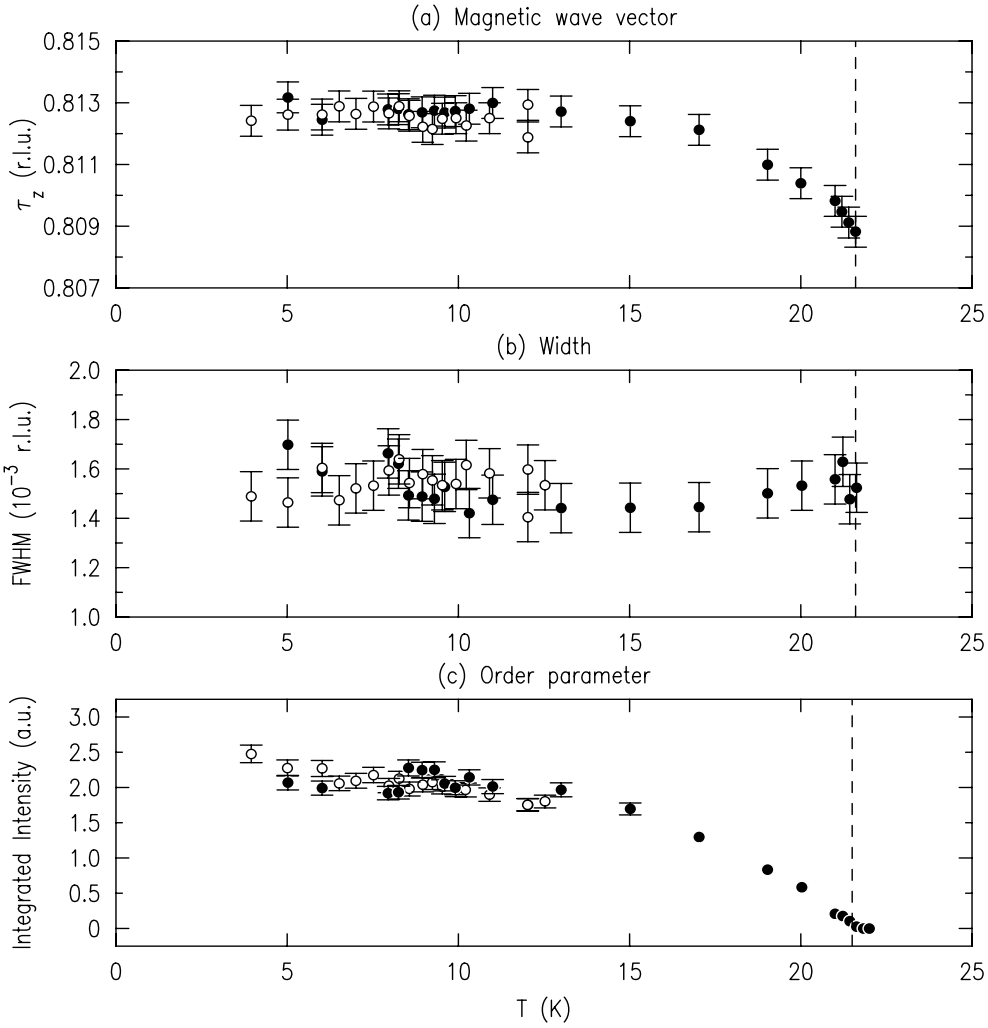

Figure E.2 The magnetic wave vector, $\boldsymbol{\tau}_1$, the width of the Bragg reflection and the order parameter of $PrNi_2Ge_2$ compound. The peak position to calculate $\boldsymbol{\tau}_1$, width and the intensity were extracted by fitting a Lorentzian-squared line profile. The Néel temperature is indicated by the dashed line. The open circles are from a second set of measurements to check the reproducibility. Data were collected on raising the temperature.

intensity decreases gradualy to the background level at T_N as shown in Fig. E.2(c). No significant changes of the wave vector, the width or the intensity of the magnetic peak were observed in the vicinity of T_t.

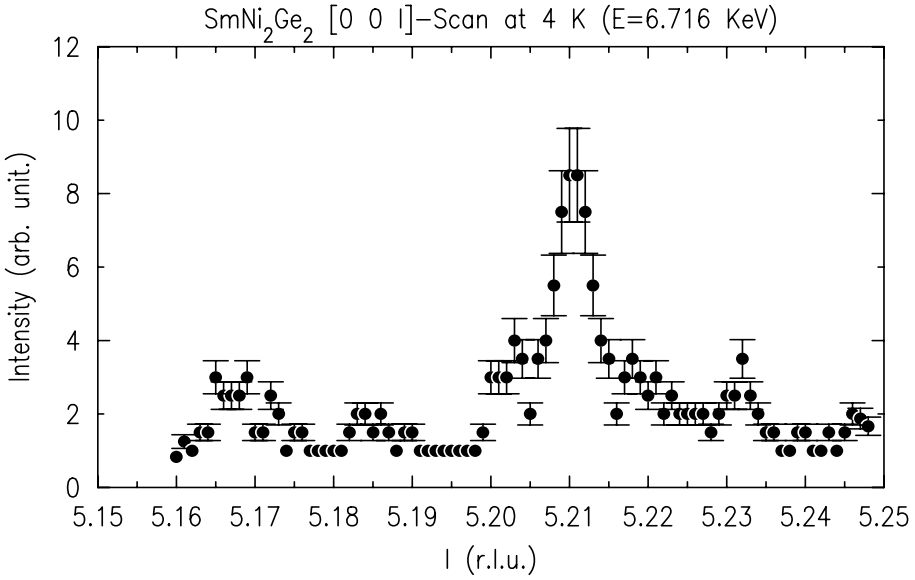

Figure E.3 [0 0 l] scan for $SmNi_2Ge_2$ showing the magnetic satellite peak at (0 0 6)-(0 0 ∼0.791).

At the end of the XRES measurements on $PrNi_2Ge_2$ preliminary XRES studies of $SmNi_2Ge_2$ were also carried out. The incident photon energy was changed to the Sm L_{III} edge (6.716 keV) which is close to the Pr L_{II} edge. These measurements were performed at ∼4 K well below T_N. A weak superlattice peak at (0 0 ∼0.791) was observed as shown in Fig. E.3. Availability of limited time did not allow any further studies on this sample.

BIBLIOGRAPHY

[1] A. Szytuła and J. Leciejewicz. *Handbook of the crystal structures and magnetic properties of rare earth intermetallics.* CRC Press, Boca Raton, FL, U.S.A., 1994.

[2] A. Szytuła and J. Leciejewicz. Magnetic properties of ternary intermetallic compounds of the RT_2X_2 type. In K. A. Gschneidner, editor, *Handbook on the physics and chemistry rare earths*, volume 12, pages 133–211. Elsevier Science, Amsterdam, The Netherlands, 1989.

[3] D. Gignoux and D. Schmitt. Magnetism of compounds of rare earths with nonmagnetic metals. In K. H. J. Buschow, editor, *Handbook of magnetic materials*, volume 10, chapter 2, page 369. Elsevier Science Publishers B.V., Amsterdam, The Netherlands, 1997.

[4] S. H. Liu. Electronic structure of the rare earth metals. In Jr. K. A. Gschneidner and Le Roy Eyring, editors, *Handbook on the physics and chemistry of rare earths*, volume I, chapter 3. North-Holland Publishing Company, NY, 1978.

[5] J. Jensen and A. R. Mackintosh. *Rare earth magnetism.* Oxford University Press, NY, 1991.

[6] J. Y. Rhee, Z. Wang, and B. N. Harmon. Generalized susceptibility and magnetic ordering in rare-earth nickel boride carbides. *Phys. Rev. B (Brief Reports)*, 1995.

[7] D. R. Noakes and G. K. Shenoy. The effect of a crystalline electric field on the magnetic transition temperatures of rare earth rhodium borides. *Phys. Lett.*, 91A, 1982.

[8] K. W. H. Stevens. Matrix elements of operator equivalents connected with the magnetic properties of rare earth ions. *Proc. Phys. Soc. Lon.*, A65, 1952.

[9] M. T. Hutchings. Point-charge calculations of energy levels of magnetic ions in crystalline electric fields. In F. Seitz and D. Turnbull, editors, *Solid State Physics*, volume 16. Academic Press, New York, 1964.

[10] C. Zener. Classical theory of the temperature dependence of magnetic anisotropy energy. *Phys. Rev.*, 96, 1954.

[11] E. R. Callen and H. B. Callen. Anisotropic magnetization. *J. Phys. Chem. Solids*, 16, 1960.

[12] E. Callen and H. B. Callen. Magnetostriction, forced magnetostriction, and anomalous thermal expansion in ferromagnets. *Phys. Rev.*, 139, 1965.

[13] P.-A. Lindgård and O. Danielsen. Theory of magnetic properties of heavy rare earth metals: Temperature dependence of magnetization, anisotropy, and resonance energy. *Phys. Rev. B*, 11, 1975.

[14] H. J. Zeiger and G. W. Pratt. *Magnetic interactions in solids.* Oxford University Press, Oxford, UK, 1973.

[15] M. Tinkham. *Group theory and quantum mechanics.* McGraw-Hill, Inc. New York, 1964.

[16] G. H. Dieke. *Spectra and energy levels of rare earth ions in crystals.* Interscience Publishers, 1968.

[17] B. Barbara, D. Gignoux, and C. Vettier. *Lectures on modern magnetism.* Science Press Beijing, China, 1988.

[18] C. Song, Z. Islam, L. Lottermoser, A. I. Goldman, P. C. Canfield, and C. Detlefs. Magnetoelastic tetragonal-to-orthorhombic distortion of $TbNi_2B_2C$. *Submitted to Phys. Rev. B (Brief Reports)*, 1999.

[19] C. Detlefs, A.H.M.Z. Islam, T. Gu, A. I. Goldman, C. Stassis, and P. C. Canfield. Magneticelastic tetragonal-to-orthorhombic distortion in $ErNi_2B_2C$. *Phys. Rev. B*, 56, 1997.

[20] P. Morin and D. Schmitt. Quadrupolar interactions and magneto-elastic effects in rare earth intermetallic ompounds. In E. P. Wohlfarth and K. H. J. Buschow, editors, *Handbook on ferromagnetic materials*, volume 5, chapter 1. North-Holland, Amsterdam, 1990.

[21] J. Jensen, J. G. Houmann, and H. Bjerrum Møller. Spin waves in terbium. I. Two-ion magnetic anisotropy. *Phys. Rev. B*, 12, 1975.

[22] W. Rieger and E. Partheé. Ternäre Erdalkali- und Seltene Erdmetall-Silicide und -Germanide mit $ThCr_2Si_2$-Struktur. *Monatsch. Chem.*, 100, 1969.

[23] S. L. Bud'ko, Z. Islam, T. A. Wiener, I. R. Fisher, P. C. Canfield, and A. H. Lacerda. Anisotropy and metamagnetism in the $R Ni_2Ge_2$ (R=Y,La-Nd,Sm-Lu) series. *Submitted to J. Magn. Magn. Mater.*, 1999.

[24] J. K. Yakinthos. Crystal and magnetic structures of $TmFe_2Si_2$ and $TmNi_2Ge_2$ compounds. Influence of the d-metal charge on the anisotropy direction of the RT_2X_2 (R = rare earth, T = 3d or 4d metal and X = Si, Ge compounds. *J. Magn. Magn. Mater.*, 99, 1991.

[25] T. Shigeoka, H. Fuji, M. Nishi, Y. Uwatoko, T. Takabatake, I. Oguro, K. Motoya, N. Iwata, and Y. Ito. Metamagnetism in $TbNi_2Si_2$ single crystal. *J. Phys. Soc. Jap.*, 61, 1992.

[26] J. A. Blanco, D. Gignoux, D. Schmitt, and C. Vettier. Field induced magnetic structures in $TbNi_2Si_2$. *J. Magn. Magn. Mat.*, 1991.

[27] A. Garnier, D. Gignoux, D. Schmitt, and T. Shigeoka. Magnetic properties of tetragonal $DyNi_2Si_2$. *J. Magn. Magn. Mat.*, 145, 1995.

[28] Y. Hashimoto, T. Shigeoka, N. Iwata, H. Yoshizawa, Y. Oohara, and M. Nishi. Field-induced magnetic phase transitions in $DyNi_2Si_2$. *J. Magn. Magn. Mat.*, 140-144, 1995.

[29] M. Ito, H. Deguchi, K. Takeda, and Y. Hashimoto. Magnetic phase diagram of $DyNi_2Si_2$ with two-dimensionally modulated spin structures. *J. Phys. Soc. Jap.*, 62, 1993.

[30] D. Gignoux and D. Schmitt. Rare earth intermetallics. *J. Magn. Magn. Mat.*, 100, 1991.

[31] R. J. Elliot. Phenomenological discussion of magnetic ordering in the heavy rare earth metals. *Phys. Rev.*, 124, 1961.

[32] B. Bleaney. Crystal field effects and the co-operative state I. A primitive theory. *Proc. Roy. Soc. Lon. A*, 276, 1963.

[33] G. T. Trammel. Magnetic ordering properties of rare earth ions in strong cubic crystal field. *Phys. Rev.*, 131, 1963.

[34] J. A. Blanco, D. Gignoux, and D. Schmitt. Specific heat and metamagnetic process in a modulated compound: $PrNi_2Si_2$. *Phys. Rev. B (Rapid Comm.)*, 45, 1992.

[35] P. C. Canfield, B. K. Cho, and K. Dennis. Magnetic properties of single crystal $GdNi_2B_2C$. *Physica B*, 215, 1995.

[36] A. Szytuła, A. Oleś, Y. Allain, and G. André. Magnetic structure of $NdNi_2Ge_2$. *J. Magn. Magn. Mater.*, 75, 1988.

[37] I. Felner and I. Nowik. Magnetism and hyperfine interactions in EuM_2Ge_2 and GdM_2Ge_2 (M = Mn, Fe, Co, Ni, Cu). *J. Phys. Chem. Solids*, 39, 1978.

[38] H. Pinto, M. Melamud, M. Kuznietz, and H. Shaked. Magnetic structures in the ternary RM_2X_2 compounds (R = Gd to Tm; M = Fe, Co, Ni, or Cu; X = Si or Ge). *Phys. Rev. B*, 31, 1985.

[39] F. Bourée-Vigneron. Magnetic structures: neutron diffraction studies. *Phys. Scr.*, 44, 1993.

[40] G. André, P. Bonville, F. Bourée, A. Bombik, M. Kolenda, A. Oleś, A. Pacyna, W. Sikora, and A. Szytuła. Magnetic structures of RNi_2Ge_2 (R = Dy, Ho and Er) and $YbNi_2Si_2$. *J. Alloys and Compounds*, 224, 1995.

[41] Zahirul Islam, C. Song, A. I. Goldman, S. L. Bud'ko P. C. Canfield, D. Wermeille, and D. Gibbs. X-ray resonant exchange scattering (XRES) studies of $PrNi_2Ge_2$. Technical report, National Synchrotron Light Source, Brookhaven National Laboratory, 1998. Annual Report.

[42] Zahirul Islam, C. Song, A. I. Goldman, S. L. Bud'ko P. C. Canfield, D. Wermeille, and D. Gibbs. X-ray resonant exchange scattering (XRES) studies of $SmNi_2Ge_2$ at 4 K. Unpublished.

[43] Zahirul Islam, C. Detlefs, C. Song, A. I. Goldman, V. Antropov, B. N. Harmon, S. L. Bud'ko, P. C. Canfield, D. Wermeille, K. Finkelstein, and J. P. Hill. Mangetic

ordering in RNi$_2$Ge$_2$ and the effects of band filling on magnetic structures. To be submitted.

[44] Zahirul Islam, C. Detlefs, A. I. Goldman, S. L. Bud'ko P. C. Canfield, J. P. Hill, D. Gibbs, T. Vogt, and A. Zheludev. Neutron diffraction and x-ray resonant exchange scattering studies of the magnetic structures of TbNi$_2$Ge$_2$. *Phys. Rev. B*, 58, 1998.

[45] Zahirul Islam, C. Detlefs, A. I. Goldman, S. L. Bud'ko P. C. Canfield, and A. Zheludev. The magnetic structures of DyNi$_2$Ge$_2$. *Solid State Comm.*, 108, 1998.

[46] J. Rossat-Mignod. Magnetic structures. In K. Sköld and D. L. Price, editors, *Methods of experimental physics*, volume 23, chapter 19. Academic Press Inc., 1987.

[47] Z. Fisk and Remeika. Growth of single crystals from molten metallic fluxes. In Jr. K. A. Gschneidner and L. Eyring, editors, *Handbook on the physics and chemistry of rare earths*, volume 12, chapter 81. Elsevier Science Publishers B.V., 1989.

[48] P. C. Canfield and Z. Fisk. Growth of single crystals from metallic fluxes. *Philos. Mag. B*, 56, 1992.

[49] I. R. Fisher, Z. Islam, A. F. Panchula, K. O. Cheon, M. J. Kramer, and P. C. Canfield A. I. Goldman. Growth of large-grain R-Mg-Zn quasicrystals from the the ternary melt (R = Y, Er, Ho, Dy and Tb). *Phil. Mag. B*, 77, 1998.

[50] I. R. Fisher, M. J. Kramer, Z. Islam, A. R. Ross, A. Kracher, T. Wiener, M. J. Sailer, A. I. Goldman, and P. C. Canfield. On the growth of decagonal Al-Ni-Co quasicrystals from the ternary melt. *Phil. Mag. B*, 79, 1999.

[51] K. D. Myers. *Anisotropic magnetization and transport properties of $RAgSb_2$ (R=Y,La-Nd,Sm,Gd-Tm).* Ph.D. thesis, Iowa State University, 1999.

[52] G. Shirane. A note on the magnetic intensities of powder neutron diffraction. *Acta. Crystallogr.*, 12, 1959.

[53] G. E. Bacon. *Neutron diffraction.* Oxford University Press, Oxford, 1962.

[54] W. Marshall and S. W. Lovesey. *Theory of thermal neutron scattering.* Oxford University Press, Oxford, 1971.

[55] G. L. Squires. *Thermal neutron scattering.* Cambridge University Press, Cambridge, 1978.

[56] A. J. C. Wilson, editor. *International table for crystallography*, volume C, chapter 4.4. Kluwer Academic, Dodrecht, 1995.

[57] P. M. Platzman and N. Tzoar. Magnetic scattering of x-rays from electrons in molecules and solids. *Phys. Rev. B*, 2, 1970.

[58] F. De Bergevin and M. Brunel. Observations magnetic superlattice peaks by x-ray diffraction on an antiferromagnetic NiO crystal. *Phys. Lett.*, 39A, 1972.

[59] M. Blume. Magnetic scattering of x-rays. *J. Appl. Phys.*, 57, 1985.

[60] K. Namikawa, M. Ando, T. Nakajima, and H. Kawata. X-ray resonant magnetic scattering. *J. Phys. Soc. Jpn.*, 54, 1985.

[61] D. Gibbs, D. E. Moncton, J. Bohr K. L. D'Amico, and B. H. Grier. Magnetic x-ray scattering studies of holmium using synchrotron radiation. *Phys. Rev. Lett.*, 55, 1985.

[62] D. Gibbs, D. R. Harshman, E. D. Isaacs, D. B. McWhan, D. Mills, and C. Vettier. Polarization and resonance properties of magnetic x-ray scattering in holmium. *Phys. Rev. Lett.*, 61, 1988.

[63] J. P. Hannon, G. T. Trammel, M. Blume, and D. Gibbs. X-ray resonant exchange scattering. *Phys. Rev. Lett.*, 61, 1988.

[64] J. P. Hill and D. F. McMorrow. X-ray resonant exchange scattering: polarization dependence and correlation functions. *Acta. Crystallgr. A*, 52, 1996.

[65] C. Detlefs. *X-ray resonant exchange scattering of rare-earth nickel borocarbide.* Ph.D. thesis, Iowa State University, 1997.

[66] C. Detlefs A. H. M. Z. Islam, A. I. Goldman, C. Stassis, P. C. Canfield, J. P. Hill, and D. Gibbs. Determination of magnetic-moment directions using x-ray resonant exchange scattering. *Phys. Rev. B (Rapid Comm.)*, 53, 1997.

[67] C. Detlefs, A. I. Goldman, C. Stassis, P. C. Canfield, B. K. Cho, J. P. Hill, and D. Gibbs. Magnetic structure of $GdNi_2B_2C$ by resonant and non-resonant x-ray scattering. *Phys. Rev. B*, 53, 1996.

[68] R. W. James. *The optical principles of the diffraction of x-rays.* G. Bell and Sons Ltd., London, 1948.

[69] M. Blume and D. Gibbs. Polarization dependence of magnetic x-ray scattering. *Phys. Rev. B*, 37, 1988.

[70] A. J. Freeman. Energy band structure, indirect exchange interactions and magnetic ordering. In R. J. Elliot, editor, *Magnetic properties of rare earth metals.* Plenum Press, London, 1972.

[71] G. Czjzek, V. Oestreich, H. Schmidt, K. Łątka, and K. Tomala. A study of compounds GdT_2Si_2 by Mössbauer spectroscopy and by bulk magnetizaiton measurements. *J. Magn. Magn. Mat.*, 79, 1989.

[72] P. M. Gehring, L. Rebelsky, D. Gibbs, and G. Shirane. Magnetic x-ray-scattering study of Tb. *Phys. Rev. B*, 45, 1992.

[73] D. Gibbs, G. Grübel, D. R. Harshman, E. D. Isaacs, D. B. McWhan, D. Mills, and C. Vettier. Polarization and resonance studies of x-ray magnetic scattering in holmium. *Phys. Rev. B*, 43, 1991.

[74] T. A. Kaplan. Some effects of anisotropy on spiral spin-configuration with application to rare earth metals. *Phys. Rev.*, 329, 1961.

[75] R. J. Elliot. Theory of magnetism in the rare earth metals. In G. T. Rado and H. Suhl, editors, *Magnetism*, volume II A, chapter 7. Academic Press, NY, 1965.

[76] J. A. Blanco, D. Gignoux, and D. Schmitt. Crystal field and magnetic properties of the tetragonal $TbNi_2Si_2$ compound. *Z. Phys. B*, 89, 1992.

[77] P. C. Canfield, S. L. Bud'ko, B. K. Cho, A. Lacerda, D. Farrell, E. Johnston-Halperin, V. A. Kalatsky, and V. L. Pokrovsky. Angular dependence of metamagnetism transitions in $HoNi_2B_2C$. *Phys. Rev. B*, 55, 1997.

[78] C. Sutter, G. Grübel, C. Vettier, F. de Bergevin, A. Staunault, D. Gibbs, and C. Giles. Helicity of magnetic domains in holmium studied with circularly polarized x-rays. *Phys. Rev. B*, 55, 1997.

[79] K. Tomala, J. P. Sanchez, P. Vulliet, P. C. Canfield, Z. Drzazga, and A. Winiarska. Squared-spin-modulated versus spiral-like magnetic structures in $GdNi_2B_2C$: A ^{155}Gd Mössbauer-effect investigation. *Phys. Rev. B*, 58, 1998.

[80] T. Nagamiya. Helical spin ordering-1 theory of helical spin configuration. In F. Seitz, D. Turnbull, and H. Ehrenreich, editors, *Solid State Physics*, volume 20. Academic Press, New York, 1967.

[81] R. E. Watson and A. J. Freeman. Exchange coupling and conduction-electron polarization in metals. *Phys. Rev.*, 152, 1966.

[82] R. E. Watson and A. J. Freeman. Exchange coupling and conduction-electron polarization in metals. II. *Phys. Rev.*, 178, 1969.

[83] W. E. Evenson and S. H. Liu. Theory of magnetic ordering in the heavy rare earths. *Phys. Rev.*, 178, 1969.

[84] B. N. Harmon and A. J. Freeman. Augmented-plane-wave calculation of indirect-exchange matrix elements for gadolinium. *Phys. Rev. B*, 10, 1974.

[85] B. N. Harmon. *Conduction electron polarization, spin densities and neutron magnetic form factor of gadolinium.* Ph.D. thesis, Northwestern University, 1973.

[86] L. M. Roth, H. J. Zeiger, and T. A. Kaplan. Generalization of the Ruderman-Kittel-Kasuya-Yosida interaction for nonspherical Fermi surface. *Phys. Rev.*, 149, 1966.

[87] W. M. Lomer. Electronic structure of chromium group metals. *Proc. Phys. Soc.*, 80, 1962.

[88] O. K. Andersen, O. Jepsen, and D. Glötzel. Canonical description of the band structures of metals. In F. Bassani, F. Fumi, and M. P. Tosi, editors, *Highlights of condensed-matter theory*, pages 59–176. Italian Physical Society, 1985.

[89] J. Rath and A. J. Freeman. Generalized magnetic susceptibility in metals: Application of the analytic tetrahedron linear energy method to Sc. *Phys. Rev. B*, 11, 1975.

[90] S. H. Liu. Exchange interaction between conduction electrons and magnetic shell electrons in rare earth metals. *Phys. Rev.*, 121, 1961.

[91] S. Legvold, B. J. Baudry, J. E. Ostenson, and B. N. Harmon. Superconducting magnetic pair breaking in dhcp La-Eu and La-Gd. *Solid State Comm.*, 21, 1976.

[92] D. P. Brammeier and D. Lynch. Unpublished. Private communication.

[93] C. G. Windsor. Interband contributions to the generalized spin susceptibility of chromium. *J. Phys. F: Metal Phys.*, 2, 1972.

[94] W. E. Evenson and S. H. Liu. Generalized susceptibilities and magnetic ordering of heavy rare earths. *Phys. Rev. Lett.*, 21, 1968.

[95] J. C. Duthie and Pettifor. Correlation between d-band occupancy and crystal structure in the rare earths. *Phys. Rev. Lett.*, 38, 1977.

[96] R. P. Gupta and S. K. Sinha. Exchange enhanced generalized susceptibility function for paramagnetic chromium including band structure effects. *J. Appl. Phys.*, 41, 1970.

[97] R. P. Gupta and S. K. Sinha. Wave-number-dependent susceptibility function for paramagnetic chromium. *Phys. Rev. B*, 3, 1971.

[98] K. Grobsky and B. N. Harmon. Spin-wave temperature dependence of Gadolinium. *J. Appl. Phys.*, 49, 1978.

[99] H. J Hesse, R. Lübbers, M. Winzenick, H. W. Neuling, and G. Wortmann. Pressure and temperature dependence of the Eu valence in $EuNi_2Ge_2$ and related sustems studied by Mössbauer effect, X-ray absoption and X-ray diffraction. *J. Alloys and Compounds*, 246, 1997.

[100] K. D. Myers, S. L. Bud'ko, I. R. Fisher, Z. Islam, H. Kleinke, P. C. Canfield, and A. H. Lacerda. Systematic study of anisotropic transport and magnetic properties of RAgSb$_2$ (R=Y,La-Nd,Sm,Gd-Tm). *Submitted to J. Magn. Magn. Mater.*, 1999.

[101] E. Stryjewski and N. Giordano. Metamagnetism. *Adv. Phys.*, 26, 1977.

[102] A. Garnier, D. Gignoux, D. Schmitt, and T. Shigeoka. Evidence of mixed magnetic phases in $TbRu_2Ge_2$. *Phys. Rev. B*, 57, 1998.

[103] A. Garnier, D. Gignoux, D. Schmitt, and T. Shigeoka. Mixed magnetic phases in tetragonal $TbRu_2Ge_2$. *J. Phys.: Condens. Matter*, 10, 1998.

[104] T. Shigeoka, A. Garnier, D. Gignoux, D. Schmitt, F.-Y. Zhang, and P. Burlet. Magnetic phase diagram and field-induced magnetic structure in $TbNi_2Si_2$. *J. Phys. Soc. Jap.*, 63, 1994.

[105] T. Tsuneto and T. Murao. Spin ordering in a system with large anisotropy energy in a magnetic field. *Physica*, 51, 1971.

[106] G. F. Koster, J. O. Dimmock, R. G. Wheeler, and H. Statz. *Properties of the thirty-two point groups*. M.I.T. Press, 1963.

[107] Mrachkov and E. Leyarovsky. Crystalline electric field effects in the magnetic properties of hexagonal praseodymium compounds. *Physica B*, 150, 1988.

ACKNOWLEDGMENTS

A mere word of gratitude to my major advisor, Alan I. Goldman, is bound to be inadequate in acknowledging his myriad of contributions in the completion of this dissertation as well as to my development as an experimental physicist. It is impossible for me to imagine that I could have accomplished this work without his endless patience, thoughtful guidance, incessant intellectual input, and more importantly, his kind and relentless support during the difficult times.

I have been fortunate, intellectually and personally, to have Paul C. Canfield as my co-major advisor. His unending enthusiasm and spontaneous excitement during discussions of physics, scientific insights, *meticulous* editing, congruent encouragements, and epicurean attitude toward gastronomy, both guided my research and made the last few years of experience memorable.

A special word of appreciation is due to Bruce N. Harmon who has shown enormous patience in answering even the silliest questions of an experimentalist uninitiated in theory and helped me learn how to "surf" on Fermi surface. My work with him has been one of the most fruitful collaborations of my research experience.

The experiments, which constitute the core of this work, were carried out at various research facilities, namely, National Synchrotron Light Source (NSLS, X22C) and High-Flux Beam Reactor (HFBR) in Brookhaven National Laboratory (BNL), Cornell High Energy Synchrotron Source (CHESS, C1), Institute Laue-Langevin (D15) and Atomic Energy Canada Ltd. (AECL) reactor (C5) at the Chalk River Laboratory. I spent a lot of exciting moments at these places during my experiments. I want to thank John

P. Hill and Doon Gibbs of the Physics Department at BNL for their collaboration and intellectual contribution to this work. Thanks are also due to Ken Finkelstein (CHESS), T. Vogt and A. Zheludev (BNL), P. Burlet (CEA, Grenoble, France), and W. J. L. Buyers (AECL) for their collaboration. I thankfully acknowledge Panagiotis Dervenagas for arranging more than two weeks of beam-time at ILL in short notice and becoming actively involved in the experiment.

I recall having many stimulating conversations on physics, and the rest, with my past lab-mate Carsten Detlefs during our trips to national laboratories and want to thank him for taking the time to discuss and answer many questions that I had. I appreciate having many interesting conversations about life, fish, war, science, computers, and etc. with Sergey Bud'ko, Ian R. Fisher, and my lab-mates, past and present, Tianqu Gu, Brandon Gordon, Changyong Song, and Lars Lottermoser. I want to thank Tim Wiener and Ken Myers for growing some of the samples studied in this work. I would also like to thank V. Antropov for his help with the electronic band calculations and patience in answering my questions.

I have benefited in various ways from other colleagues and research scientists in Ames Laboratory, Physics and Astronomy department and from other research laboratories through exchange of ideas. I appreciate having such opportunities.

Also, I am thankful to the Downare family for their hospitality and kindness, in a number of occasions, and their continued comraderie.

I am grateful to my parents for their kind support and encouragement. I thank them so much for sending me to Bemidji, Minnesota, for an undergraduate education.

Finally, my deepest appreciation goes to my spouse, Akiko Kasai, for her continued support for my work, regardless of all the turmoil she has been through, and my frequent absence from home. Our trip together to the Rockies, or Badlands, or elsewhere, was always delightful and a welcome get-away from my hectic research life. And, I want to thank her for her performance on the piano, which is the source of so much joy and

strength that I cannot do without.

This work was performed at Ames Laboratory under Contract No. W-7405-Eng-82 with the United States Department of Energy (USDOE). This work was supported by the Director of Energy Research, Office of Basic Sciences. The United States government has assigned the DOE Report number IS-T1870 to this thesis. The work at BNL was carried out under Contract No. DEAC0298CH10886, Division of Materials Science, USDOE. The work at CHESS was funded by the National Science Foundations.